

**NASA  
Technical  
Paper  
1959**

February 1982

# Dynamics of Aircraft Antiskid Braking Systems

John A. Tanner,  
Sandy M. Stubbs,  
Robert C. Dreher,  
and Eunice G. Smith

LOAN COPY RETURN TO  
AFWL TECHNICAL LIBRARY  
KIRTLAND AFB, N. M.

NASA  
TP  
1959  
c.1



**NASA**

**NASA  
Technical  
Paper  
1959**

1982

TECH LIBRARY KAFB, NM



0134992

# Dynamics of Aircraft Antiskid Braking Systems

John A. Tanner,  
Sandy M. Stubbs,  
Robert C. Dreher,  
and Eunice G. Smith  
*Langley Research Center  
Hampton, Virginia*

**NASA**

National Aeronautics  
and Space Administration

Scientific and Technical  
Information Branch



## CONTENTS

SUMMARY .....	1
INTRODUCTION .....	1
SYMBOLS .....	2
ANTISKID BRAKING TESTS .....	4
Brakes .....	4
Tires .....	4
Skid-Control Systems .....	4
Facility .....	5
Instrumentation .....	5
Test Procedure .....	6
Data Reduction .....	6
TIRE STATIC AND FREE-VIBRATION TESTS .....	7
Facility .....	7
Instrumentation .....	8
Test Procedure .....	8
Data Reduction .....	8
WHEEL, BRAKE, AND TIRE POLAR MOMENTS OF INERTIA .....	9
Facility .....	9
Test Procedure and Instrumentation .....	10
Data Reduction .....	10
COMPUTER SIMULATION STUDIES OF BRAKE PRESSURE-TORQUE RESPONSE .....	10
Experimental Data Input .....	10
Current Computer Models .....	11
Undamped nonlinear spring .....	11
Linear spring with viscous damping .....	11
Variable Nonlinear Spring With Hysteresis Memory Function .....	12
Error Term .....	13
RESULTS AND DISCUSSION .....	13
Dynamics of Antiskid Control Valve .....	14
Static and dynamic response characteristics .....	14
Computer modeling considerations .....	14
Tire Dynamics During Braking and Cornering .....	15
Braking and cornering friction coefficients .....	15
Tire spring, damping, and inertia characteristics .....	15
Computer modeling considerations .....	16
Dynamic Characteristics of the Brake .....	16
Brake pressure-volume characteristics .....	16
Dynamic pressure-torque response .....	16
Computer modeling considerations .....	17
CONCLUDING REMARKS .....	19
REFERENCES .....	21

TABLES ..... 23

FIGURES ..... 28

APPENDIX A - PRESSURE, TORQUE, AND FRICTION FIGURES ..... 50

APPENDIX B - COMPUTER CODES ..... 88

    Experimental Data Input ..... 88

    Undamped Nonlinear Spring ..... 89

    Linear Spring With Viscous Damping ..... 90

    Variable Nonlinear Spring With Hysteresis Memory Function ..... 91

## SUMMARY

An experimental investigation was conducted at the Langley Aircraft Landing Loads and Traction Facility to study the dynamic response characteristics of three, representative, aircraft antiskid braking systems and their components. A computer study was performed to assess the accuracy of three, brake pressure-torque mathematical models. The investigation utilized one wheel, brake, and tire assembly from the main gear of a McDonnell Douglas DC-9 series 10 airplane.

The experimental investigation indicates that the performance characteristics of aircraft antiskid braking systems are strongly influenced by: the spring, damping, and friction characteristics of the tire; the dynamic response of the antiskid control valve; and the pressure-torque response of the brake. The computer study employed an average-torque error criterion to assess the accuracy of three mathematical models in duplicating the pressure-torque response of the brake on the DC-9 series 10 airplane. The three models were characterized as an undamped nonlinear spring, a linear spring with viscous damping, and a variable nonlinear spring with hysteresis memory function. The results of the computer study indicate that the variable nonlinear spring with hysteresis memory function models the pressure-torque response more accurately than the other two models.

## INTRODUCTION

Advances in avionics are making it possible to conduct airplane takeoff and landing operations under increasingly severe weather conditions. Such operations place stringent design requirements on the airplane braking and steering systems. Consequently, designers of modern antiskid braking systems are relying more heavily on the computer to aid in the design and testing of these systems (refs. 1 to 3). A practical computer simulation of any antiskid system must take into account several dynamic characteristics which may affect system performance. The dynamics of the antiskid control valve, the spring and damping properties of the tire during braking and steering maneuvers, and the brake pressure-torque characteristics are typical dynamic responses that must be represented, either by the inclusion of the appropriate hydraulic or electrical hardware in analog simulations or by accurate mathematical modeling in digital simulations, if the computer is to give realistic results (refs. 1, 2, and 4).

The mathematical modeling of dynamic response characteristics associated with aircraft antiskid braking systems is a formidable task, and there is a lack of definitive data available to assess the accuracy of the modeling techniques currently employed in computer simulations. Thus, a need exists to obtain data on the response characteristics of antiskid braking systems under realistic operating conditions and to establish the accuracy of computer modeling techniques so that present analytical methods of designing and testing antiskid braking systems can be improved.

For several years, the National Aeronautics and Space Administration (NASA), with support from the Federal Aviation Administration (FAA), has been engaged in a research program to study the behavior of airplane antiskid braking systems under the controlled conditions afforded by the Langley Aircraft Landing Loads and Traction Facility. The investigations used wheels, brakes, tires, and hydraulic components

from a McDonnell Douglas DC-9 series 10 airplane (refs. 5 to 7). Additional static and free-vibration tests have been conducted on a DC-9 aircraft tire to establish spring, damping, and polar moment of inertia characteristics. The experimental program described in references 5 to 7 provided a unique opportunity to study dynamic response characteristics associated with antiskid braking systems. The studies also generated detailed input data required to conduct a computer study to assess the accuracy of several brake pressure-torque mathematical models.

The purpose of this paper is to present the dynamic characteristics of representative airplane antiskid braking systems under controlled test conditions and the results of a computer study to determine the accuracy of several brake pressure-torque models. A film supplement is available which gives a graphic representation of the observed antiskid braking and cornering behavior. A request form and a description of the film are included in the back of this report.

McDonnell Douglas Corporation, Eastern Airlines, Messier-Hispano-Bugatti, and the Hydro-Aire Division of the Crane Company provided antiskid-system hardware for this investigation and the FAA furnished the wheels, brakes, and tires.

Identification of commercial products in this report is used to adequately describe the model. The identification of these commercial products does not constitute official endorsement, expressed or implied, of such products or manufacturers by the National Aeronautics and Space Administration.

#### SYMBOLS

Values are given in both SI and U.S. Customary Units. The measurements and calculations were made in U.S. Customary Units. Factors relating the two systems are given in reference 8.

$c_t$	time constant
$F$	force
$F_{max}$	maximum force applied in static loading tests
$F_0$	force at zero deflection
$J$	polar moment of inertia
$J_t$	tire polar moment of inertia
$J_{tare}$	polar moment of inertia of mounting disks and attachments
$K$	spring stiffness
$l$	cable length
$m$	mass
$m_p$	platen mass
$m_t$	effective tire mass

$N$             oscillation count  
 $P$             brake pressure  
 $P_0, P_1, P_2$         brake pressure offsets  
 $R$             radius to support cables for torsional pendulum  
 $r_t$           tire radius  
 $r_w$           wheel radius  
 $T$             brake torque  
 $t$             time  
 $t_0$           time of initial brake application  
 $t_1, t_2$         time limits of integration  
 $V$             ground speed  
 $v$             wheel angular velocity  
 $v_0$           synchronous wheel velocity  
 $W$             weight  
 $x_1, x_N$         amplitudes of oscillation  
 $Y, Z$         variable coefficients  
 $\alpha_t$         tire angular acceleration  
 $\alpha_w$         wheel angular acceleration  
 $\gamma$         structural damping factor  
 $\mu$           friction coefficient  
 $\rho$           viscous damping factor  
 $\tau$           period of oscillation  
 $\omega_n$         natural frequency

**Subscripts:**

act          actual  
c            cornering  
d            drag  
err         error

lb        lower bound  
mod      model  
st        static  
ub        upper bound

A bar over a symbol denotes an average value.

## ANTISKID BRAKING TESTS

### Brakes

The brakes used in the antiskid braking tests were designed for use on the McDonnell Douglas DC-9 series 10 airplane. A photograph of one of the assembled brakes is shown in figure 1. The major components of the brake consist of the housing, torque tube, back plate, pressure plate, 5 rotating disks, 4 stationary disks, and 14 pistons. The brake lining is a conventional sintered-steel design. The brake housing contains two separate hydraulic systems, and each system services 7 of the 14 pistons. During the course of this investigation, only one of the hydraulic systems was used, which is typical of airline operations of this brake. Tests were conducted with brake supply pressure set at 21 MPa (3000 psi), the maximum working pressure for the brake, and at 14 MPa (2000 psi).

### Tires

The tires used in this investigation were 40 × 14 type VII, bias-ply aircraft tires of 22-ply rating with a rated maximum speed of 200 knots (1 knot = 0.5144 m/s). The tires were stock retreads with a six-groove pattern, and the study included both new and worn tread configurations. A photograph of two tires having new and worn treads is presented in figure 2. The tire with the new tread is shown inflated and the tire with the worn tread is shown uninflated. The new tread had a groove depth of 0.71 cm (0.28 in.) and was considered new until the groove depth decreased to 0.36 cm (0.14 in.). A commercially available tire-grinding machine was employed to remove the tread rubber uniformly from the retreaded tire until a groove depth of 0.05 cm (0.02 in.) remained. This simulated worn tire was probably in a worse tread-wear condition (95 to 100 percent of tread removed) than is normally experienced in airplane operations. Throughout the antiskid braking tests the tire inflation pressure was maintained at the normal airline operational pressure of 965 kPa (140 psi). The inflation pressures for the static and free-vibration tests ranged from 965 kPa (140 psi) to 1172 kPa (170 psi).

### Skid-Control Systems

Three, different skid-control systems were used in this investigation, referred to herein as systems A, B, and C. System A was a velocity-rate-controlled, pressure-bias-modulated skid-control system. System B was a slip-ratio-controlled skid-control system which, on the airplane, relied upon a ground-speed reference from an unbraked nose wheel. System C was a slip-velocity-controlled, pressure-bias-

modulated skid-control system. Systems A and C rely upon the braked wheel for acceleration and/or reference ground-speed information. More detailed descriptions of these systems can be found in references 5 (system A), 6 (system B), and 7 (system C). Each of the systems was configured to simulate a braking system that had electronic and hydraulic components, including correct line lengths and sizes, for a single main wheel of a McDonnell Douglas DC-9 series 10 airplane. Figure 3 is a photograph of the major hydraulic components of system C installed on the test carriage.

A pressure relief valve was installed in the return line to maintain a back pressure of 448 kPa (65 psi) in the brake lines. This back pressure was maintained for systems A and C, but the back pressure for system B is questionable because of faulty seals in the relief valve. The inactive brake hydraulic system was at essentially atmospheric pressure. These back-pressure conditions differ from normal airline operational conditions which call for a back pressure of 345 kPa (50 psi) to be maintained in both brake hydraulic systems.

### Facility

The antiskid braking tests (refs. 5 to 7) were performed on a test carriage at the Langley Landing Loads Track described in reference 9. Figure 4 is a photograph of the carriage with the test wheel assembly installed. Figure 5 is a close-up view of the wheel and tire and shows details of the instrumented dynamometer which was used instead of a landing-gear strut to support the wheel and brake assembly because it provided an accurate measurement of the ground forces.

Approximately 244 m (800 ft) of the 366 m (1200 ft) of flat concrete test runway available were used to provide braking and cornering data on a dry surface, on an artificially damped surface, and on an artificially flooded surface. The 61 m (200 ft) of runway preceding the test section was used for the initial wheel spin-up and brake actuation, and the 61 m (200 ft) of runway beyond the test section was retained for brake release. To obtain a damp condition, the test surface was lightly wetted with no standing water. For the flooded runway condition, the test section was surrounded by a flexible dam and flooded to a depth of approximately 1.0 cm (0.4 in.). The runway was level and had no crown for drainage purposes; therefore, the entire runway had a uniform surface wetness condition, and antiskid cycling occurred for the entire 244 m (800 ft). The concrete surface in the test area had a light broom finish in a transverse direction, and the surface texture was somewhat smoother than that for most operational concrete runways. The average texture depth of the runway was 159  $\mu\text{m}$  (0.00628 in.), which is slightly less than that of a typical operational runway. (See ref. 10, for example.) During the course of testing on the dry surface, rubber was deposited on the runway, particularly with a yawed tire, and it was necessary to clean the surface periodically.

### Instrumentation

During the antiskid braking tests, the tire friction forces were measured by means of the instrumented dynamometer shown in figure 5 and illustrated schematically in figure 6. Strain gages were mounted on the five dynamometer support beams: two of the beams were used for measuring vertical forces, two were used for measuring drag forces parallel to the wheel plane, and a single beam was used for measuring side force perpendicular to the wheel plane. The accelerometers on the test-wheel

axle provided information for inertia corrections to the force data. The axle was supported at each end by spherical bearings which allow the axle to rotate without inducing bending moments in the five dynamometer support beams. The axle was also connected to the dynamometer through a combination of four torque links. (See insert in fig. 6.) These torque links are loaded in tension under the influence of brake torque and are subjected to a small bending moment due to the combined effects of the vertical and drag forces. The torque links were instrumented to measure the strains induced by the brake torque and to be insensitive to the bending moments induced by the vertical and drag forces. Hence the brake-torque and drag-force measurements are uncoupled. A transducer installed in the hydraulic line near the brake was used to measure the brake pressure. A steel-reinforced, cogged, rubber timing belt was driven by the test wheel to turn an auxiliary axle which drove an assortment of pulse (ac) alternators and dc generators that were used to obtain a measure of the test-wheel angular velocity. Signals from the appropriate alternators supplied wheel-speed and/or angular-acceleration information to antiskid systems A and C. Signals from the appropriate dc generator supplied wheel-speed information to antiskid system B. The skid signals produced by the various antiskid systems were recorded for an examination of their characteristics. A lightweight trailing wheel was mounted on the side of the test carriage as shown in figure 7, and the output from a dc generator mounted on its axle supplied information on the carriage speed. For the tests involving antiskid system B, this carriage speed information was also routed to the antiskid control box to provide the reference ground speed in lieu of a nose wheel. All data outputs were fed into appropriate signal conditioning equipment and then into two frequency-modulated tape recorders. A time code was fed into the two recorders simultaneously to provide synchronization of the two sets of data.

#### Test Procedure

The technique for the antiskid braking tests consisted of setting the dynamometer and tire assembly to the preselected yaw angle (if cornering were desired), propelling the test carriage to the proper speed, applying a preselected vertical load on the tire, and monitoring the outputs from the onboard instrumentation. The brake was actuated by a pneumatic piston at the pilot metering valve (see fig. 3), which gave full pedal deflection or maximum braking, and the various antiskid systems modulated the braking effort. The brake was remotely actuated, applied for the full distance, and remotely released just prior to carriage arrestment. The nominal carriage speeds ranged from 40 to 100 knots, as measured approximately midway along the runway. After initial acceleration, the carriage coasted through the test section and there was a small speed decay due to air drag, friction, and the antiskid braking of the test tire itself. The vertical loading was varied from approximately 54.7 kN (12 300 lbf) to 114.3 kN (25 700 lbf), which represented nominal operational loads for a single wheel of the DC-9 series 10 airplane. Tests were run at tire yaw angles of 0° and 6°. Antiskid system A was tested at a nominal brake-system pressure of 14 MPa (2000 psi) and antiskid systems B and C were tested at a nominal brake system pressure of 21 MPa (3000 psi).

#### Data Reduction

All data acquired during the antiskid braking tests were filtered to 1000 Hz and recorded on magnetic tape. Except for the alternator signals, these data were again filtered to 60 Hz, digitized at 250 samples per second, and stored on tape. From these digitized data, direct measurements were obtained of the carriage speed, the

braked-wheel angular velocity, the skid signals generated by the various antiskid systems, the brake pressure and torque, the total drag force, the side force, the total tire vertical force, and the accelerations at the wheel axle. The instantaneous force data were corrected for acceleration effects and were combined vectorally to compute the instantaneous drag-force friction coefficient parallel to the direction of motion and the cornering-force friction coefficient perpendicular to the direction of motion. The wheel angular velocity  $v$  was combined with carriage synchronous velocity  $v_0$  to compute the instantaneous, wheel slip ratio according to the following expression:

$$\text{Slip ratio} = 1 - \frac{v}{v_0} \quad (1)$$

The data for the various antiskid control systems were then used to obtain plots of the pressure-skid signal response, the brake pressure-torque response, the drag-force friction coefficient  $\mu_d$  against wheel slip ratio, and the cornering-force friction coefficient  $\mu_c$  against wheel slip ratio. These plots are presented in appendix A.

## TIRE STATIC AND FREE-VIBRATION TESTS

### Facility

Tire static and free-vibration tests were performed to establish the spring and damping characteristics of the DC-9 airplane tire to model accurately the effects of tire friction, spring, damping, and inertia characteristics. The static and free-vibration tests were conducted on the tire vibration stand described in reference 11. Figure 8 is a photograph of the stand set up for a lateral free-vibration test. The main structure of the stand is configured as two, three-bay portal frames joined overhead by four beams and along the floor by a thick plate. The wheel rim is supported on one side by a tapered, welded box structure and on the other side by a vertical beam. The wheel rim supports are suspended from the upper part of the structure and secure the wheel to prevent tire rotation.

The special feature of the tire vibration stand is the support of the test platen by four wire-rope cables. Each cable is suspended from a force-measuring load cell connected to a hydraulic cylinder, as shown in figure 8. The cable free-swing length is approximately 1.83 m (6 ft). Tire vertical loading is accomplished by energizing the hydraulic cylinders to lift the platen vertically against the tire; individual cylinder control is available to equalize the cable tension or level the platen.

Three different platens were used in this investigation. The mass of these platens was 102.1 kg (225 lbm), 173.3 kg (382 lbm), and 536 kg (1182 lbm) including cables and attachments. The upper surface of each platen was painted in the center with a grit-filled enamel to minimize tire slippage.

Another hydraulic cylinder was used to displace the platen during the static tests. During the dynamic tests, a mechanical ratcheting device and a quick-release mechanism were employed to provide the initial displacement and release for the free-vibration tests. These loading mechanisms could be oriented to perform either lateral or fore-and-aft tire tests.

## Instrumentation

During tests on the tire vibration stand, the tire vertical load was measured by means of the four load cells which monitored the cable tensions. For the static loading tests, a fifth load cell monitored the applied lateral or fore-and-aft loading and a linear potentiometer was used to measure the platen displacements. The outputs from these two instruments were fed into an x-y recorder to generate load-deflection hysteresis loops. For the free-vibration tests, a servo-type accelerometer was employed to measure platen acceleration. The output from the accelerometer was fed into appropriate signal conditioning equipment and then into a frequency-modulated tape recorder. A time code was also fed into the recorder to provide a millisecond time reference.

## Test Procedure

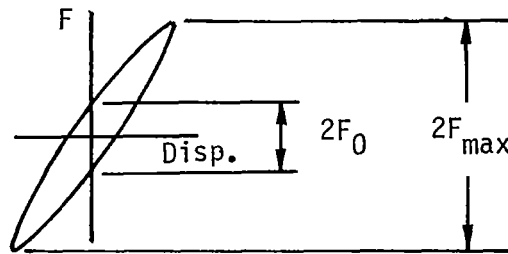
For tests on the tire vibration stand, the unloaded tire was inflated to a pre-selected pressure ranging from 965 kPa (140 psi) to 1172 kPa (170 psi). The platen was then centered beneath the tire and uniformly raised against the tire periphery. Individual hydraulic cylinder adjustments were made to equalize the cable loading and level the platen. The vertical loads ranged from approximately 58 kN (13 000 lbf) to 120 kN (27 000 lbf). The static tests were performed by slowly forcing the platen through its neutral position, a distance of approximately 0.64 cm (0.25 in.), either laterally or fore-and-aft through two complete cycles and recording the resulting load-deflection hysteresis loop on an x-y plotter. The free-vibration tests were performed by displacing the platen approximately 0.64 cm (0.25 in.), releasing it, and recording the resulting, damped, free-vibration acceleration time histories.

## Data Reduction

A typical load-deflection hysteresis loop from one of the static loading tests is presented in figure 9 to illustrate the technique used to establish the envelope of the spring stiffness of the tire. For each hysteresis loop, two spring-stiffness values are measured. One stiffness value (slope of line A-A in fig. 9) is the minimum slope of the static loading portion of the hysteresis loop, and the other value (slope of line B-B in fig. 9) is the maximum slope. The maximum slope is associated with initial load relaxation following attainment of the peak static load. The two, statically determined stiffness values define the envelope which should include all the possible spring-stiffness values obtained under dynamic loading conditions (refs. 12 and 13). The energy dissipation of the tire is manifested in these tests by the hysteresis characteristics of the load-deflection curve. To account for this energy dissipation mechanism in the tire, structural damping is assumed in this investigation (ref. 14). The structural-damping factor  $\gamma$  can be determined from the static load-deflection hysteresis loops exemplified by figure 9 according to the following equation:

$$\gamma = \frac{F_0}{F_{\max}} \quad (2)$$

where  $F_0$  and  $F_{max}$  are graphically depicted in the following sketch:



For the free-vibration tests, the average period of oscillation  $\tau$  is measured and the spring stiffness  $K$  is determined from the following equation:

$$K = m \left( \frac{2\pi}{\tau} \right)^2 \quad (3)$$

The mass of the vibrating system is assumed to be the sum of the platen mass  $m_p$  and the effective tire mass  $m_t$ :

$$m = m_p + m_t \quad (4)$$

Values of  $m_t$  were found from a coefficient obtained from a linear regression analysis of the following equation (ref. 11):

$$m_p = K \left( \frac{m}{K} \right) - m_t \quad (5)$$

The tire spring-stiffness values from both the static and free-vibration tests were corrected for cable interaction effects using the techniques outlined in reference 11.

The corresponding structural damping factors for the free-vibration tests were computed over several representative cycles using the equation

$$\gamma = \frac{1}{\pi N} \ln \left( \frac{x_1}{x_N} \right) \quad (6)$$

where  $N$  is the oscillation count and  $x_1$  and  $x_N$  are amplitudes of vibration. The structural damping factor is related to the viscous damping factor according to the expression  $\rho = \gamma/2$ .

#### WHEEL, BRAKE, AND TIRE POLAR MOMENTS OF INERTIA

##### Facility

A three-wire torsional pendulum was used to measure the polar moments of inertia of the tire, wheel, and rotating brake parts. Figure 10 is a photograph of the test tire mounted on the pendulum. The unloaded length of each cable is 4.86 m (15.94 ft) and the cable connections to the mounting disk are equally spaced around the disk at

a radius of 22.86 cm (9 in.). A fourth cable passing through a hole in the center of the mounting disk is used as a reference to insure a pure angular displacement of the system without translation.

### Test Procedure and Instrumentation

The procedure for the torsional pendulum tests involved centering and mounting the wheel, brake, or tire test article to the mounting disk, displacing the pendulum approximately 10°, releasing it, and measuring the period of oscillation. To minimize timing errors, the time required for 10 pendulum oscillations was measured and the average period of oscillation was computed. A manually triggered electronic stopwatch was used to measure the period of oscillation.

### Data Reduction

The mass moment of inertia  $J$  about the center of gravity of the various test articles was determined from the torsional pendulum tests using the following equation:

$$J = \frac{\tau^2 WR^2}{4\pi^2 l} - J_{tare} \quad (7)$$

where  $\tau$  is the period of oscillation,  $W$  is the weight of the test specimen,  $R$  is the radius to the support cables of the torsional pendulum,  $l$  is the cable length, and  $J_{tare}$  is the polar moment of inertia of the mounting disks and attachments.

### COMPUTER SIMULATION STUDIES OF BRAKE PRESSURE-TORQUE RESPONSE

The computer simulation utilized a typical brake-pressure time history from one of the antiskid braking tests to study the responses of the various pressure-torque models and compared the torque outputs from the models with the actual torque response of the brake. The following sections describe the experimental data input, the computer models of the brake pressure-torque response, and the error function used to assess the accuracy of the pressure-torque models. The computer codes for the brake pressure-torque models used in this investigation are presented in appendix B.

### Experimental Data Input

Time histories of brake pressure and torque from typical antiskid braking tests were digitized at 25 samples per second and used to generate data tables for the computer simulation tests. The computer program uses linear interpolation to approximate intermediate values and provides for extrapolation of data which falls outside of the table range, but the starting and stopping points of the simulation runs were set within the program to eliminate the need for extrapolation. The brake pressure data were used as input for the brake pressure-torque models, and the brake torque data were needed to define the torque error function for each model.

## Current Computer Models

Undamped nonlinear spring.- The computer model of the brake pressure-torque response, which is used in a Langley aircraft ground handling simulator project (ref. 15), can be characterized as an undamped nonlinear spring. In reference 15, the torque is assumed to be the product of a ground-speed function and a pressure function according to the following equation:

$$T = f(V) g(P) \quad (8)$$

for the ground speed  $V$  expressed in m/s,

$$\begin{aligned} f(V) = & 0.9944013639 - 9.832431338 \times 10^{-4}(V) \\ & -1.180138027 \times 10^{-6}(V)^2 + 8.560911033 \times 10^{-9}(V)^3 \\ & -9.407435981 \times 10^{-12}(V)^4 \end{aligned} \quad (9a)$$

where  $V < 61$  m/s (200 ft/s). For ground speed expressed in ft/s,

$$\begin{aligned} f(V) = & 0.9944013639 - 0.00322586335(V) \\ & -0.000012702928(V)^2 + 3.0232572 \times 10^{-7}(V)^3 \\ & -1.08996216 \times 10^{-9}(V)^4 \end{aligned} \quad (9b)$$

where  $V < 61$  m/s (200 ft/s) or

$$f(V) = 0.52 \quad (9c)$$

where  $V > 61$  m/s (200 ft/s). The pressure function is

$$\begin{aligned} g(P) = & -1540.608088 + 0.110788323(P) \\ & -2.427221348 \times 10^{-7}(P)^2 + 2.558172351 \times 10^{-13}(P)^3 \end{aligned} \quad (10a)$$

where  $P > 0.68$  MPa (100 psi) for pressure expressed in MPa, or

$$\begin{aligned} g(P) = & -1540.608088 + 16.0684884(P) \\ & -0.00510589018(P)^2 + 7.805 \times 10^{-7}(P)^3 \end{aligned} \quad (10b)$$

where  $p > 0.68$  MPa (100 psi) for pressure expressed in psi, or

$$g(P) = 0 \quad (10c)$$

where  $P < 0.68$  MPa (100 psi).

The coefficients of equations (9) and (10) represent least-squares curve fits to the brake-characteristic curves presented in figure C-5 of reference 15. For any given speed, equations (9) and (10) produce a single-valued, nonlinear, brake pressure-torque response with no hysteresis.

Linear spring with viscous damping.- The computer model of brake pressure-torque response described in reference 1 can be characterized as a linear spring with vis-

cous damping. In this model, a static torque gain  $T_{st}$  is defined by the following system of equations:

$$T_{st} = 0.64(P - P_0)^{0.7} \quad \text{in SI Units} \quad (11a)$$

$$T_{st} = 73.0(P - P_0)^{0.7} \quad \text{in U.S. Customary Units} \quad (P > P_0) \quad (11b)$$

$$T_{st} = 0 \quad (P < P_0) \quad (11c)$$

The static torque gain is then input to a linear spring-damper system. The dynamic torque output from the spring-damper system is modified by an exponential time function to approximate the initial brake-actuation lag. This torque lag is defined by the following equation:

$$\text{Torque lag} = 1.0 - e^{-(t-t_0)/c_t} \quad (12)$$

where  $c_t = 0.3$  sec. The output of this model is a multivalued, nonlinear pressure-torque response.

#### Variable Nonlinear Spring With Hysteresis Memory Function

A third brake pressure-torque model was developed in this investigation to simulate as closely as possible the observed pressure-torque response of the DC-9 brake. This model can be characterized as a variable nonlinear spring with hysteresis memory function and defines an envelope which encloses the possible brake pressure-torque responses. The lower brake-torque boundary is associated with increasing pressure and is defined by the following system of equations:

$$T_{lb} = 3.06(P - P_1)^{0.65} \quad \text{in SI Units} \quad (13a)$$

$$T_{lb} = 89(P - P_1)^{0.65} \quad \text{in U.S. Customary Units} \quad (P > P_1) \quad (13b)$$

$$T_{lb} = 0 \quad (P < P_1) \quad (13c)$$

The upper brake-torque boundary is associated with decreasing pressure and is defined by the following system of equations:

$$T_{ub} = Y(P - P_2)^{0.47} \quad \text{in SI Units} \quad (14a)$$

$$T_{ub} = Z(P - P_2)^{0.47} \quad \text{in U.S. Customary Units} \quad (P > P_2) \quad (14b)$$

$$T_{ub} = 0 \quad (P < P_2) \quad (14c)$$

and

$$T_{ub} = 20.61 \text{ kJ } (15 \text{ 200 ft-lbf}) \quad (14d)$$

as an upper limit.

The coefficients  $Y$  and  $Z$  are variable and range from 1.46 to 5.62 and 104 to 400, respectively, depending upon the maximum pressure reached during the preceding pressure cycle.

The brake-pressure input is numerically differentiated and a flag is set when the pressure derivative is greater than 0.34 MPa/s (50 psi/s) and the model operates on the lower boundary. The flag is cleared when the pressure derivative is less than -3.45 MPa/s (-500 psi/s) and the model operates on the upper boundary.

Brake-actuation lag is approximated by an exponential time function and operates on increasing-pressure cycles only. For this application, the time constant  $c_t$  is 0.075 sec in equation (12). A second exponential time function allows a maximum torque growth of 18 percent during the braking effort and is defined as

$$\text{Torque growth} = 1.18 - 0.18e^{-(t-t_0)/c_t} \quad (15)$$

where  $c_t = 3.0$  sec. When the brake pressure falls below  $P_1$ , the two time functions are reinitialized. The maximum torque developed while pressure is increasing is stored and serves as a temporary upper limit on torque during pressure release, and, conversely, the minimum torque reached during brake release is stored and used as a temporary lower limit on torque during the next brake application cycle. This constitutes the hysteresis memory function.

#### Error Term

To assess the accuracy of the computer models, the torque output from each model is compared with the actual torque response of the brake for the same pressure input. This comparison leads to an average-torque error term defined by the following equation:

$$\bar{T}_{\text{err}} = \frac{1}{t_2 - t_1} \int_{t_1}^{t_2} (|T_{\text{act}} - T_{\text{mod}}|) dt \quad (16)$$

where  $t_1$  and  $t_2$  enclose the time interval over which  $\bar{T}_{\text{err}}$  is measured. The average torque error is computed for each model by numerical integration techniques. The value of  $\bar{T}_{\text{err}}$  is a direct indication of the ability of a computer model to duplicate the actual brake response and is equal to zero when the brake pressure-torque response is modeled exactly.

#### RESULTS AND DISCUSSION

The overall response of an antiskid braking system is influenced by individual response characteristics of three major components - the antiskid control valve, the tire, and the brake. Subsequent sections describe antiskid-control-valve dynamics, tire dynamics during braking and cornering, and dynamic characteristics of the brake. Data describing the response of these components for the three antiskid braking systems of this study are presented in figures A1 to A37 of appendix A. These figures present the variations of brake pressure with skid signal and the variations of brake torque with brake pressure for the antiskid braking systems under a variety of test conditions. The figures also present braking-force friction coefficients plotted as a function of wheel slip ratio and, for the tests run at a yaw angle of 6°, cornering-force friction coefficient plotted as a function of wheel slip ratio.

Tables I and II are summaries of test conditions and results of fore-and-aft and lateral free-vibration tests used to determine spring, damping, and effective-mass

characteristics of the tire. Table III is a summary of test conditions and results of static tests used to measure tire spring and damping characteristics, and table IV is a summary of torsional pendulum tests used to determine polar moments of inertia of the wheel, tires, and brake rotors used in this investigation.

#### Dynamics of Antiskid Control Valve

Static and dynamic response characteristics.- The dynamic response characteristics of an aircraft antiskid-braking-system control valve can be illustrated by plotting brake pressure as a function of the skid signal. Typical examples of the dynamic response of the three antiskid valves used in this investigation are presented in figure 11. Dashed lines representing the so-called static response characteristics of the control valves are superimposed over the dynamic responses in figure 11. When the braking effort is initiated for antiskid system A (fig. 11(a)), the skid signal is at its minimum value of approximately 5 mA, hydraulic fluid flows through the normally open antiskid control valve to the brake, and the brake pressure rapidly increases to the pilot-commanded pressure of approximately 14 MPa (2000 psi). At the onset of wheel skidding (a in fig. 11(a)), the antiskid system reacts quickly to increase the skid signal and hence, calls for a large reduction in the brake pressure (b in fig. 11(a)). This response causes a large hysteresis loop to be developed in the skid signal-pressure plot that is centered about the static valve characteristic, thereby suggesting that the hydraulic response of the antiskid control valve lags the electronic response of the valve. When the antiskid system senses recovery from the skid, the skid signal is reduced to permit reapplication of the brake pressure and the sequence is repeated several times during the remainder of the run. These hysteresis loops are built up in a clockwise sense during antiskid cycling, and similar hysteresis loops were observed in the valve responses of all three antiskid systems in this investigation, as illustrated by figures 11(b) and 11(c). The extent, shape, and position of the hysteresis loops exhibited in the valve dynamic responses are influenced by such factors as frequency of antiskid cycling, pressure-bias-modulation characteristics of the antiskid systems, static valve response characteristics, and the response characteristics of the brake hydraulic system. For example, rapid variations in the brake pressure cause the dynamic response of the antiskid valves to differ significantly from the static response denoted by the dashed lines in figure 11. This is particularly true for antiskid system B (fig. 11(b)) which does not employ pressure-bias modulation. Pressure-bias modulation retards the pressure reapplication following recovery from wheel skidding, which allows the dynamic response of the control valve to follow closely the static response during brake pressure recovery. However, pressure-bias modulation usually results in less than optimum braking performance, because brake pressure is slow to return to the levels required to develop peak, braking-friction-coefficient values.

Computer modeling considerations.- Any computer simulation of an antiskid braking system must accurately model the dynamic valve-response characteristics (fig. 11). It is possible to represent the hydraulic characteristics of aircraft antiskid braking systems mathematically through a system of lumped-mass, nonlinear-spring, and dashpot representations, but this approach requires considerable experimentation and verification of the model parameters by comparisons with actual system dynamic data. The approach currently favored by most antiskid and airframe manufacturers is to employ actual hydraulic hardware in a "breadboard" layout (see fig. 3), duplicating as nearly as possible the actual aircraft configuration. The breadboard hardware includes the brake, a pilot metering valve, a hydraulic fuse, rigid and flexible hydraulic lines, and the antiskid control valve, thereby insuring that the

hydraulic response characteristics of the computer simulation are nearly identical to those of the airplane. (See refs. 1 and 15 for examples.)

### Tire Dynamics During Braking and Cornering

Braking and cornering friction coefficients.- Typical examples of the drag-force and cornering-force friction coefficients, obtained during antiskid braking at a 6° yaw angle on dry and damp runway surfaces, are plotted as a function of the wheel slip ratio in figure 12. The drag-force friction coefficient  $\mu_d$  increases with slip ratio, reaches a peak value at a slip ratio of approximately 0.15, denoted by the vertical dashed lines in figure 12, and decreases with further increases in slip ratio. The cornering-force friction coefficient  $\mu_c$  is at a maximum value when the wheel is unbraked (Wheel slip ratio = 0) and decreases with increasing braking effort. At a slip ratio of 0.15, the cornering-force friction coefficient has been reduced between 30 and 40 percent and, at a slip ratio greater than 0.4,  $\mu_c$  becomes negligible. These results clearly illustrate the trade-off between braking and cornering. The data in figure 12 indicate that the antiskid system is causing the tire to operate primarily on the front side (0 to 0.15 slip ratio) of the friction-slip curve which should minimize tread wear and cornering losses. However, the ability of the antiskid system to modulate the braking effort is complicated by the data bandwidth in the figure, and this bandwidth is much larger on the damp runway (fig. 12(b)) than on the dry runway (fig. 12(a)). These oscillations in the tire friction-coefficient/slip response are the result of variations in the available runway friction level and the dynamic response characteristics of the tire which acts as a spring coupling between the wheel and the tire/pavement interface. The variation in the available runway friction level is attributed to such factors as tire heating on the dry runway, changes in the runway texture depth, and the extent of water contamination on the damp runway.

Tire spring, damping, and inertia characteristics.- The spring and damping characteristics of the tire, which define its dynamic response, determined from free-vibration tests in the fore-and-aft and lateral directions are presented in tables I and II, respectively. The spring and damping characteristics obtained from static loading tests are presented in table III. The weights and polar moments of inertia of the tire, wheel, and rotating brake parts are presented in table IV. The data indicate that the tire spring stiffness in the fore-and-aft direction increases approximately 7 percent when the inflation pressure is increased from 965 kPa (140 psi) to 1172 kPa (170 psi). The stiffness increases approximately 6 percent when the vertical load is increased from 58 kN (13 000 lbf) to 120 kN (27 000 lbf). The lateral tire spring stiffness increases approximately 15 percent when the inflation pressure is increased from 965 kPa (140 psi) to 1172 kPa (170 psi) and decreases approximately 7 percent when the vertical load is increased from 58 kN (13 000 lbf) to 120 kN (27 000 lbf). The spring stiffness in the fore-and-aft direction is approximately 3.5 times higher than the spring stiffness in the lateral direction. The tire spring stiffness values obtained from the free-vibration tests are 20 to 30 percent higher than the spring stiffness values associated with the loading portion of the static hysteresis loops and about 7 percent lower than the spring stiffness values associated with initial load relaxation following attainment of the peak static load.

The tire structural damping factor in the fore-and-aft and lateral directions is approximately 0.132 and 0.088, respectively, as measured from free-vibration tests. Hence, damping in the fore-and-aft direction is about 1/3 higher than damping in the lateral direction. These damping values are 20 to 30 percent higher than the values

obtained from the static loading tests. The tire effective mass calculated from data gathered during the free-vibration tests has a mean value of roughly 8.16 kg (18 lbm), which is approximately 12 percent of the total tire mass of 65.43 kg (144.25 lbm). These data are in agreement with the data presented in reference 11. The polar moment of inertia of the wheel, brake, and tire assembly is dominated by the polar moment of inertia of the tire. The polar moment of inertia of the worn tire was approximately 12 percent lower than the polar moment of inertia for the new tire.

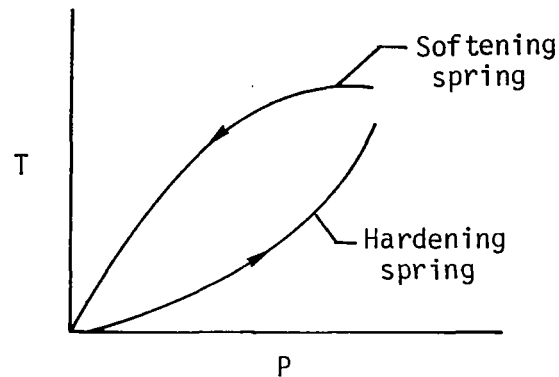
Computer modeling considerations.- Computer simulations of antiskid braking systems can be made more accurate by including the effects of tire friction, spring, damping, and inertia characteristics. Most computer simulations have the capability of modeling variations in braking and cornering friction coefficients with wheel slip ratio on dry and wet runway surfaces as a family of single-valued, nonlinear functions similar to those shown in figure 13. The computer simulations also include tire inertia characteristics, but many simulations do not model the rapidly changing runway friction levels which can exist on damp surfaces (fig. 12(b)) and even fewer computer simulations model the effects of the spring coupling between the wheel and the tire/pavement interface (compare fig. 12 with fig. 13, for example). Without these additional refinements, the tire dynamic characteristics are not adequately represented in the computer simulation, and the antiskid model could produce misleading results. Previous analog-computer model studies (ref. 4) of an antiskid braking system indicate that the spring and damping characteristics of the tire can be modeled fairly well by assuming that the wheel and tire are both rigid and connected by a linear spring and viscous damper. A schematic representation of the system of reference 4 is presented in figure 14.

#### Dynamic Characteristics of the Brake

Brake pressure-volume characteristics.- The hydraulic response of the brake is a function of its pressure-volume characteristic. In figure 15, the brake pressure is plotted as a function of the fluid displacement for the DC-9 brake used in this study. The data were obtained from the brake manufacturer. The resulting curve is nonlinear and indicates that about 14.91 cm<sup>3</sup> (0.91 in<sup>3</sup>) of hydraulic fluid is required to compress the brake stack of stators and rotors and an additional displacement of approximately 8.19 cm<sup>3</sup> (0.50 in<sup>3</sup>) is required to develop a pressure of 20 MPa (2900 psi). The slope of the curve in figure 15 is analogous to brake stiffness which is inversely proportional to the fluid flow required to modulate brake pressure. A good brake design maximizes stiffness. For this brake, maximum stiffness is observed for pressures above about 4.14 MPa (600 psi), and the antiskid system can modulate the brake pressure with a minimum fluid flow requirement. For pressures below 4.14 MPa (600 psi), the brake is operating on the "knee" of the pressure-volume response (see fig. 15) and the fluid flow requirement for brake pressure modulation is considerably larger. Pressure modulation below 4.14 MPa (600 psi) is typical of antiskid operation on slippery runway surfaces, and the larger fluid-flow requirements for this pressure range can lead to degradation in overall system performance.

Dynamic pressure-torque response.- Time histories of the pressure input to the brake during a typical antiskid braking test and the resulting torque output from the brake are presented in figure 16. The relationship between brake pressure and torque defines the brake behavior during antiskid operations and plays a critical role in

establishing the braking performance of antiskid braking systems. The torque in figure 16 is plotted as a function of pressure in figure 17 to illustrate this characteristic more graphically. The relationship depicted in the figure is characterized by a number of hysteresis loops, and these loops are developed in a counter-clockwise sense during the course of the test. Hence, the torque developed as a result of a given pressure input can vary over a large band and is dependent upon previous braking history. The primary influence of these hysteresis loops is to cause the torque gain to behave like a hardening spring during brake application (increasing pressure) and to behave like a softening spring during brake release (decreasing pressure) as depicted in the following sketch:



The hardening spring characteristic, which is especially pronounced during the initial brake application, delays development of torque levels sufficient to produce peak friction coefficient. The softening spring characteristic during brake release promotes deeper tire skidding during antiskid cycling which can, in turn, delay skid recovery. Therefore brake designs which minimize the size of these hysteresis loops will enhance the performance of the antiskid system.

The outer boundary of the hysteresis loops shown in figure 17 generally encompasses the measured pressure-torque responses presented in appendix A for all three antiskid systems. Instantaneous pressure-torque responses of the brake within this envelope are a function of the runway friction level and the response characteristics of each antiskid system. The extent of the hysteresis envelope is a function of brake temperature, fade, and stiffness characteristics; low-speed torque peaking; brake-lining friction characteristics; back pressure in the hydraulic lines; and, to a lesser extent, brake wear. When locked-wheel skids occur during antiskid cycling, the torque ceases to be a function of pressure, but is related, instead, to tire friction and inertia characteristics according to the expression

$$T = J_t \alpha_t - \mu_d W r_t \quad (17)$$

where  $J_t$  is the tire moment of inertia,  $\alpha_t$  is the tire angular acceleration,  $W$  is the tire load,  $\mu_d$  is the drag-force friction coefficient, and  $r_t$  is the tire radius.

Computer modeling considerations.- An accurate model of the brake dynamic behavior is necessary to enable computer simulations to tune existing antiskid systems to optimize their braking and cornering performance for specific aircraft

applications and to aid in the design of future systems. The pressure-volume response of the brake can be duplicated by including the brake hardware in a "breadboard" simulation, but the pressure-torque response of the brake must be modeled mathematically. Most of the current computer simulations model this response either as an undamped nonlinear spring (ref. 15) or as a linear spring with viscous damping coupled with a nonlinear static torque gain (ref. 1). During the course of this investigation, a third brake pressure-torque model was developed which can be characterized as a variable nonlinear spring with a hysteresis memory function. The mathematical expressions representing these three pressure-torque models are presented in equations (8) to (15), and the computer coding is presented in appendix B. Figure 18 presents the pressure-torque responses of these models to the measured antiskid-braking-pressure input shown in figure 16(a) and should be compared with the measured pressure-torque response of the brake for the same pressure input (fig. 17). The response of the undamped nonlinear spring is shown in figure 18(a) and can be characterized as a nonlinear, single-valued curve. This curve provides an accurate fairing of the actual torque response of the brake but does not exhibit the pronounced hysteresis loops observed in the measured response. The pressure-torque responses of both the linear spring with viscous damping (fig. 18(b)) and the variable nonlinear spring with hysteresis memory function (fig. 18(c)) exhibit hysteresis characteristics that are similar to the measured brake response. Antiskid computer simulations which fail to model accurately the hysteresis characteristics of the brake pressure-torque response generally underestimate (1) the severity of tire skidding which occurs during antiskid braking and (2) the time required for skid recovery. Such simulations produce unconservative estimates of antiskid braking performance. Thus, there is a need for brake manufacturers to generate the dynamic torque data required to define the brake pressure-torque hysteresis envelope during development or qualification tests to facilitate accurate computer modeling.

Results of a computer study to assess the accuracy of these pressure-torque models is summarized in table V. Two tests from each of the three antiskid braking systems employed in this investigation were selected for this computer study, and an average torque error criteria (eq. (16)) was used as a measure of the accuracy of each model. The undamped-nonlinear-spring model is expressed as the product of a speed function and a pressure function (eqs. (8) to (10)) and was unaltered during the course of the computer studies. The linear spring with viscous damping employed the nonlinear static torque gain (eqs. (11)) recommended in reference 1 throughout the computer study, but the recommended spring and damping characteristics of the second-order transfer system were not used. Instead a parametric study was conducted to establish the spring and damping characteristics that minimized the average torque error for each antiskid system application and these values are listed in table V along with a brake pressure offset value  $P_0$ . Similarly, a parametric study was used to establish the pressure offsets associated with the variable nonlinear spring with hysteresis memory function, equations (14) and (15), and the best-fit pressure values are also listed in table V. These variations in model parameters for the different antiskid systems are necessary to compensate for the differences in the pressure-torque response of the brake caused by variations in back pressure of the hydraulic lines.

The torque error with antiskid braking system B is generally higher than the torque error associated with the other antiskid braking systems. This difficulty is probably caused by the rapid pressure cycling characteristics of system B because of the lack of pressure-bias modulation. If the torque errors for each model are averaged over the six antiskid braking tests, a comparison among the three models indicates that the variable nonlinear spring with hysteresis memory function has torque errors which are more than 40 percent lower than the undamped nonlinear spring and

the linear spring with viscous damping. This result indicates that the variable nonlinear spring with hysteresis memory function has the potential to provide more accurate pressure-torque models in antiskid simulations; however, these data are for a single brake design and additional tests with different brake designs are needed to further corroborate these results.

#### CONCLUDING REMARKS

An experimental investigation was conducted at the Langley Aircraft Landing Loads and Traction Facility to study dynamic response characteristics of three representative aircraft antiskid braking systems and their components, and a computer study was performed to assess the accuracy of three, brake pressure-torque mathematical models. Tests included antiskid braking studies conducted on dry and wet runway surfaces, static- and free-vibration tests of the tires used, and torsional pendulum measurements of the tire, wheel, and brake polar moments of inertia. The investigation utilized one main-gear wheel, brake, and tire assembly of a McDonnell Douglas DC-9 series 10 airplane.

The experimental investigation indicates that the performance characteristics of aircraft antiskid braking systems are strongly influenced by the spring, damping, and friction characteristics of the tire; the dynamic response of the antiskid control valve; and the pressure-torque response of the brake. Variations in the drag-force and cornering-force friction coefficients with wheel slip ratio are influenced by the spring and damping characteristics of the tire and by the runway friction level. The dynamic-pressure/skid-signal response of the antiskid control valves used in this study indicate that brake pressure variations lag the electronic skid-signal commands during antiskid cycling. The extent of the pressure lag is a function of the frequency of antiskid cycling, the pressure-bias-modulation characteristics of the antiskid system, the static valve response characteristics, and the hydraulic response characteristics of the braking system. The dynamic pressure-torque response of the brake during antiskid cycling is characterized by a number of large hysteresis loops which cause the brake torque gain to behave like a hardening spring during brake application and to behave like a softening spring during brake release. Antiskid computer simulations which fail to model accurately the hysteresis characteristics of the brake pressure-torque response generally underestimate the severity of tire skidding which occurs during antiskid braking and the time required for skid recovery. Such simulations produce unconservative estimates of antiskid braking performance. Thus to facilitate accurate computer modeling, brake manufacturers should generate the dynamic torque data required to define the brake pressure-torque hysteresis envelope during development or qualification tests. Most computer simulations have the capability of modeling the variations in braking and cornering friction coefficients with wheel slip ratio on dry and wet runway surfaces as a family of single-valued, nonlinear functions. The computer simulations also include the tire inertia characteristics, but many do not simulate the rapidly changing runway friction levels which can exist on damp surfaces. Even fewer computer simulations model the effects of the spring coupling between the wheel and the tire/pavement interface. Without these additional refinements, the tire dynamic characteristics will not be adequately represented and the antiskid model could produce misleading results.

The computer study described in this paper employed an average-torque error criterion to assess the ability of three mathematical models to duplicate the pressure-torque response of the brake for a DC-9 series 10 airplane. The three models were characterized as an undamped nonlinear spring, a linear spring with viscous damping, and a variable nonlinear spring with hysteresis memory function.

The results of the computer study indicate that the variable nonlinear spring with hysteresis memory function is significantly more accurate than the other two models; however, additional studies employing different brake designs are needed to further corroborate these results.

Langley Research Center  
National Aeronautics and Space Administration  
Hampton, VA 23665  
December 8, 1981

## REFERENCES

1. Straub, H. H.; Yurczyk, R. F.; and Attri, N. S.: Development of a Pneumatic-Fluidic Antiskid System. AFFDL-TR-74-117, U.S. Air Force, Oct. 1974. (Available from DTIC as AD A009 170.)
2. Straub, H. H.; Attri, N. S.; and Yurczyk, R. F.: Test and Performance Criteria for Airplane Antiskid Systems. AFFDL-TR-74-118, U.S. Air Force, Oct. 1974. (Available from DTIC as AD A008 536.)
3. Hirzel, E. A.: Antiskid and Modern Aircraft. [Preprint] 720868, Soc. Automot. Eng., Oct. 1972.
4. Batterson, Sidney A.: A Study of the Dynamics of Airplane Braking Systems as Affected by Tire Elasticity and Brake Response. NASA TN D-3081, 1965.
5. Stubbs, Sandy M.; and Tanner, John A.: Behavior of Aircraft Antiskid Braking Systems on Dry and Wet Runway Surfaces - A Velocity-Rate-Controlled, Pressure-Bias-Modulated System. NASA TN D-8332, 1976.
6. Tanner, John A.; and Stubbs, Sandy M.: Behavior of Aircraft Antiskid Braking Systems on Dry and Wet Runway Surfaces - A Slip-Ratio-Controlled System With Ground Speed Reference From Unbraked Nose Wheel. NASA TN D-8455, 1977.
7. Stubbs, Sandy M.; Tanner, John A.; and Smith, Eunice G.: Behavior of Aircraft Antiskid Braking Systems on Dry and Wet Runway Surfaces - A Slip-Velocity-Controlled, Pressure-Bias-Modulated System. NASA TP-1051, 1979.
8. Standard for Metric Practice. E 380-79, American Soc. Testing & Mater., c.1980.
9. Tanner, John A.: Fore-and-Aft Elastic Response Characteristics of 34 x 9.9, Type VII, 14 Ply-Rating Aircraft Tires of Bias-Ply, Bias-Belted, and Radial-Belted Design. NASA TN D-7449, 1974.
10. Yager, Thomas J.; Phillips, W. Pelham; Horne, Walter B.; and Sparks, Howard C. (Appendix D by R. W. Sugg): A Comparison of Aircraft and Ground Vehicle Stopping Performance on Dry, Wet, Flooded, Slush-, Snow-, and Ice-Covered Runways. NASA TN D-6098, 1970.
11. Sleeper, Robert K.; and Dreher, Robert C.: Tire Stiffness and Damping Determined From Static and Free-Vibration Tests. NASA TP-1671, 1980.
12. Tanner, John A.; Stubbs, Sandy M.; and McCarty, John L.: Static and Yawed-Rolling Mechanical Properties of Two Type VII Aircraft Tires. NASA TP-1863, 1981.
13. Tanner, John A.; McCarty, John L.; and Clark, S. K.: Current Research in Aircraft Tire Design and Performance. 1980 Aircraft Safety and Operating Problems, Joseph W. Stickle, compiler, NASA CP-2170, Part 2, 1981, pp. 543-553.
14. Scanlan, Robert H.; and Rosenbaum, Robert: Introduction to the Study of Aircraft Vibration and Flutter. Macmillan Co., c.1951.

15. McGowan, J. A.: Expansion of Flight Simulator Capability for Study and Solution of Aircraft Directional Control Problems on Runways - Appendixes. NASA CR-145281, 1978.
16. Advanced Continuous Simulation Language (ACSL) - User Guide/Reference Manual. Mitchell and Gauthier Assoc., Inc., c.1975.

TABLE I.- SUMMARY OF FORE-AND-AFT TIRE SPRING AND DAMPING CHARACTERISTICS  
 DETERMINED FROM FREE-VIBRATION TESTS

Test	Platen mass, $m_p$		Tire pressure		Vertical load		Spring stiffness, K		Damping factor, $\gamma$	Effective tire mass, $m_t$			
	kg	lbm	kPa	psi	kN	lbf	kN/m	lbf/in		kg	lbm		
1	102	225	965	140	58.5	13 160	2880	16 444	0.126	12.3	27.1		
2					79.9	17 960	2956	16 880	.130	7.3	16.0		
3					89.0	20 000	3032	17 315	.132	.9	2.0		
4					119.7	26 920	3049	17 409	.138	11.2	24.8		
5					1069	155	57.8	13 000	2952	16 859	.122	7.6	16.7
6			79.9	17 960			2956	16 880	.130	15.0	33.0		
7			88.9	19 980			3065	17 505	.126	8.4	18.6		
8			120.3	27 040			3105	17 731	.140	13.5	29.7		
9					1172	170	58.4	13 140	2992	17 099	.124	9.8	21.6
10			80.7	18 140			3115	17 789	.136	6.8	14.9		
11			89.1	20 040			3186	18 196	.128	2.7	5.9		
12			121.7	27 360			3303	18 862	.134	1.7	3.8		
13	173	382	965	140	57.6	12 960	3015	17 215	0.138	12.3	27.1		
14					80.1	18 000	3040	17 360	.138	7.3	16.0		
15					89.1	20 040	3044	17 380	.138	.9	2.0		
16					119.7	26 920	3181	18 167	.136	11.2	24.8		
17					1069	155	57.6	12 960	3040	17 358	.136	7.6	16.7
18			80.4	18 080			3122	17 828	.138	15.0	33.0		
19			89.7	20 160			3166	18 079	.136	8.4	18.6		
20			119.7	26 920			3265	18 646	.134	13.5	29.7		
21					1172	170	58.5	13 160	3108	17 746	.130	9.8	21.6
22			80.6	18 120			3198	18 263	.132	6.8	14.9		
23			90.6	20 380			3220	18 389	.134	2.7	5.9		
24			120.1	27 000			3328	19 003	.134	1.7	3.8		
25	536	1182	965	140	58.2	13 080	2668	15 233	0.130	12.3	27.1		
26					80.6	18 120	2614	14 929	.136	7.3	16.0		
27					90.6	20 360	2760	15 759	.136	.9	2.0		
28					120.5	27 080	2759	15 755	.148	11.2	24.8		
29					1069	155	58.2	13 080	2722	15 542	.132	7.6	16.7
30			80.4	18 080			2768	15 808	.132	15.0	33.0		
31			90.2	20 280			2843	16 236	.132	8.4	18.6		
32			121.0	27 200			2870	16 387	.136	29.7	29.7		
33					1172	170	58.0	13 040	2849	16 268	.112	9.8	21.6
34			79.5	17 880			3037	17 643	.112	6.8	14.9		
35			89.3	20 080			2897	16 543	.138	2.7	5.9		
36			120.1	27 000			2991	17 081	.142	1.7	3.8		

TABLE II.- SUMMARY OF LATERAL TIRE SPRING AND DAMPING CHARACTERISTICS

DETERMINED FROM FREE-VIBRATION TESTS

Test	Platen mass, $m_p$		Tire pressure		Vertical load		Spring stiffness, $K$		Damping factor, $\gamma$	Effective tire mass, $m_t$	
	kg	lbm	kPa	psi	kN	lbf	kN/m	lbf/in		kg	lbm
1	102	225	965	140	57.8	13 000	887	5065	0.114	7.6	16.8
2					80.7	18 140	866	4947	.114	9.4	20.7
3					89.0	20 000	828	4730	.116	7.5	16.6
4					120.3	27 040	833	4756	.116	11.3	25.0
5			1069	155	57.5	12 920	906	5175	.114	4.1	9.1
6					80.8	18 160	881	5032	.118	7.4	16.4
7					88.9	19 980	867	4952	.114	.7	1.6
8					119.6	26 880	819	4675	.138	20.4	45.1
9			1172	170	59.6	13 400	1043	5957	.130	8.6	19.1
10					80.5	18 100	1031	5885	.130	11.4	25.1
11					88.5	19 900	1016	5802	.136	8.6	18.9
12					118.9	26 720	935	5341	.118	1.5	3.4
13	173	382	965	140	58.9	13 240	928	5301	0.086	7.6	16.8
14					79.8	17 940	894	5107	.074	9.4	20.7
15					90.0	20 240	899	5133	.074	7.5	16.6
16					120.2	27 020	881	5030	.078	11.3	25.0
17			1069	155	57.4	12 900	1020	5823	.070	4.1	9.1
18					79.4	17 840	971	5543	.072	7.4	16.4
19					90.2	20 280	969	5532	.072	.7	1.6
20					120.0	27 000	952	5434	.074	20.4	45.1
21			1172	170	60.2	13 540	1070	6111	.084	8.6	19.1
22					80.8	18 160	1019	5820	.078	11.4	25.1
23					89.9	20 200	1021	5829	.074	8.6	18.9
24					120.7	27 140	993	5673	.074	1.5	3.4
25	536	1182	965	140	57.3	12 880	951	5428	0.070	7.6	16.8
26					80.1	18 000	930	5313	.074	9.4	20.7
27					90.0	20 240	905	5170	.076	7.5	16.6
28					118.9	26 720	918	5243	.078	11.3	25.0
29			1069	155	57.8	13 000	991	5659	.070	4.1	9.1
30					80.1	18 020	971	5543	.072	7.4	16.4
31					88.2	19 840	928	5298	.072	.7	1.6
32					119.9	26 960	996	5688	.068	20.4	45.1
33			1172	170	58.2	13 080	1112	6348	.064	8.6	19.1
34					80.5	18 100	1092	6237	.066	11.4	25.1
35					89.0	20 000	1070	6110	.074	8.6	18.9
36					119.7	26 900	977	5578	.066	1.5	3.4

TABLE III.- SUMMARY OF STATIC TIRE SPRING AND DAMPING CHARACTERISTICS

Test	Tire pressure		Vertical load		Spring stiffness, K				Damping factor, $\gamma$
	kpa	psi	kN	lbf	High		Low		
					kN/m	lbf/in	kN/m	lbf/in	
Fore and Aft									
1	965	140	58.3	13 100	3015	17 218	1945	11 105	0.104
2			80.4	18 080	3049	17 410	1941	11 082	.106
3			89.1	20 040	3060	17 475	2032	11 605	.098
4			119.7	26 920	3254	18 581	2038	11 640	.106
5	1069	155	58.2	13 080	3162	18 058	1982	11 318	.098
6			79.9	17 960	3338	19 063	2014	11 503	.102
7			89.1	20 040	3484	19 894	2150	12 280	.104
8			119.6	26 880	3232	18 455	2117	12 091	.100
9	1172	170	57.8	13 000	3191	18 223	1991	11 367	.104
10			80.6	18 120	3335	19 043	2153	12 295	.110
11			89.5	20 120	3321	18 963	2077	11 863	.110
12			119.0	26 760	3242	18 516	2204	12 589	.104
Lateral									
13	965	140	57.8	13 000	1029	5 877	787	4 492	0.062
14			80.2	18 040	973	5 558	769	4 391	.066
15			89.7	20 160	1013	5 783	792	4 522	.066
16			119.2	26 800	987	5 637	743	4 243	.074
17	1069	155	58.5	13 160	1020	5 822	851	4 859	.070
18			80.5	18 100	982	5 609	761	4 346	.072
19			89.1	20 040	1032	5 895	776	4 434	.078
20			118.9	26 720	1015	5 799	774	4 421	.082
21	1172	170	58.0	13 040	1080	6 169	834	4 761	.074
22			80.1	18 000	1058	6 043	856	4 890	.072
23			89.0	20 000	1129	6 450	823	4 699	.072
24			118.1	26 560	1036	5 917	803	4 587	.080

TABLE IV.- SUMMARY OF WEIGHTS AND POLAR MOMENTS OF INERTIA

Item	Weight		Polar moment of inertia	
	N	lbf	N-m-s <sup>2</sup>	lbf-in-s <sup>2</sup>
New tire <sup>a</sup>	641.66	144.25	10.04	88.89
Worn tire <sup>a,b</sup>	590.50	132.75	8.81	78.01
Wheel	227.97	51.25	.15	1.35
Brake rotors(5)	190.16	42.75	.41	3.62

<sup>a</sup>Inflated to 965 kPa (140 psi).

<sup>b</sup>95 to 100 percent of tread removed.

TABLE V.- SUMMARY OF RESULTS FROM BRAKE PRESSURE-TORQUE COMPUTER

MODEL ACCURACY STUDIES

$$\left[ \text{Equation (16): } \bar{T}_{\text{err}} = \frac{1}{t_2 - t_1} \int_{t_1}^{t_2} (|T_{\text{act}} - T_{\text{mod}}|) dt \right]$$

Run	Antiskid system	Speed, knots	Average torque error, $\bar{T}_{\text{err}}$					
			Undamped nonlinear spring		Linear spring with viscous damping <sup>a</sup>		Variable nonlinear spring with hysteresis memory function <sup>b</sup>	
			kN-m	ft-lbf	kN-m	ft-lbf	kN-m	ft-lbf
B2	A	73	1.56	1151	1.34	987	0.77	571
B7	A	76	1.47	1083	1.89	1397	.58	426
B13	B	97	1.38	1016	1.47	1084	1.48	1092
B18	B	71	3.01	2225	1.99	1473	.84	619
B26	C	54	1.14	844	.92	681	.70	519
B31	C	77	.71	524	.57	424	.46	338

<sup>a</sup>For antiskid system A:  $\omega_n = 23 \text{ Hz}$ ,  $\rho = 4$   
 For antiskid system B:  $\omega_n = 24 \text{ Hz}$ ,  $\rho = 1$   
 For antiskid system C:  $\omega_n = 24 \text{ Hz}$ ,  $\rho = 2$  }  $P_0 = 800 \text{ kPa (116 psi)}$

<sup>b</sup>For antiskid system A:  $P_1 = 1379 \text{ kPa (200 psi)}$ ,  $P_2 = 689 \text{ kPa (100 psi)}$   
 For antiskid system B:  $P_1 = 3999 \text{ kPa (580 psi)}$ ,  $P_2 = 689 \text{ kPa (100 psi)}$   
 For antiskid system C:  $P_1 = 2068 \text{ kPa (300 psi)}$ ,  $P_2 = 689 \text{ kPa (100 psi)}$

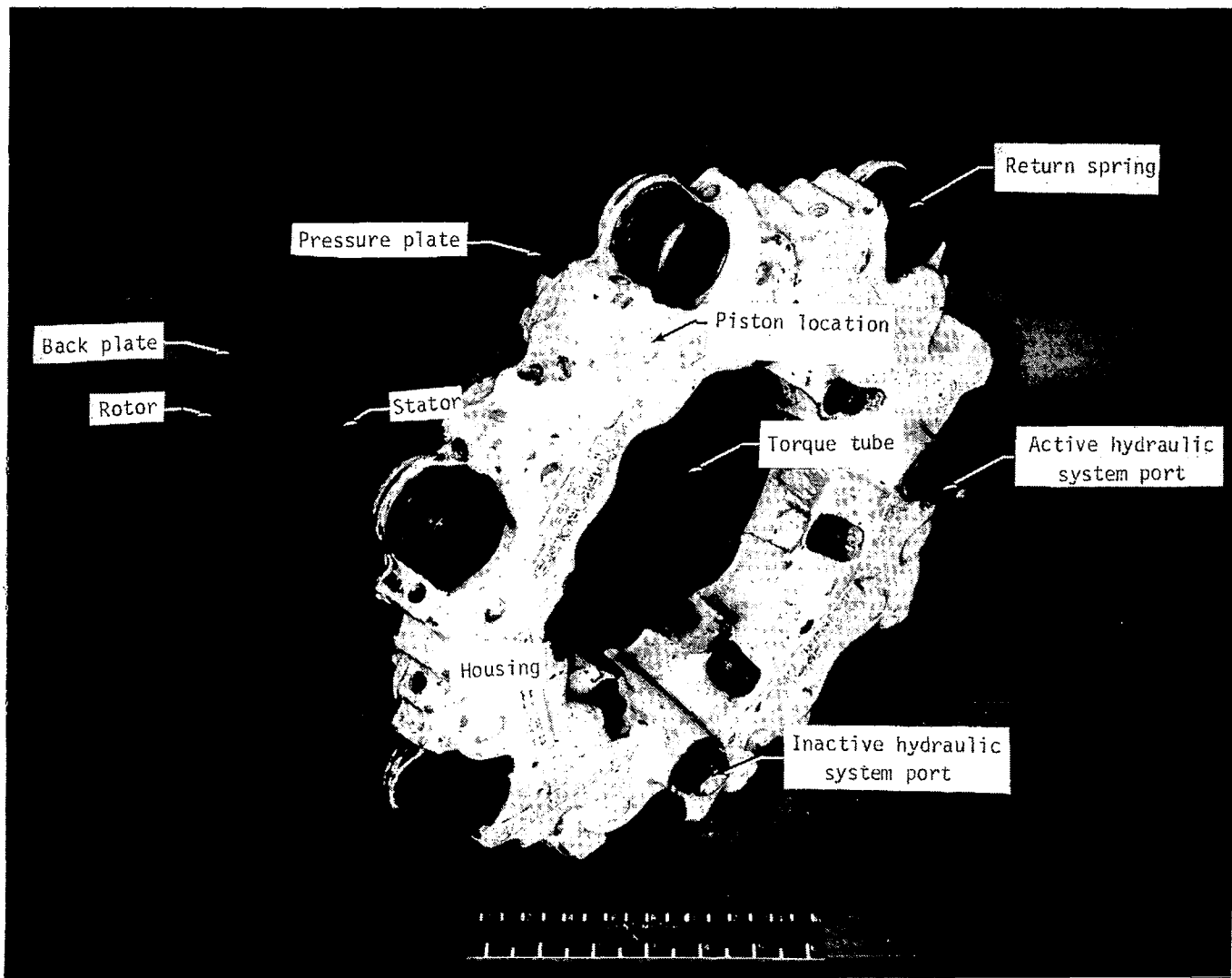


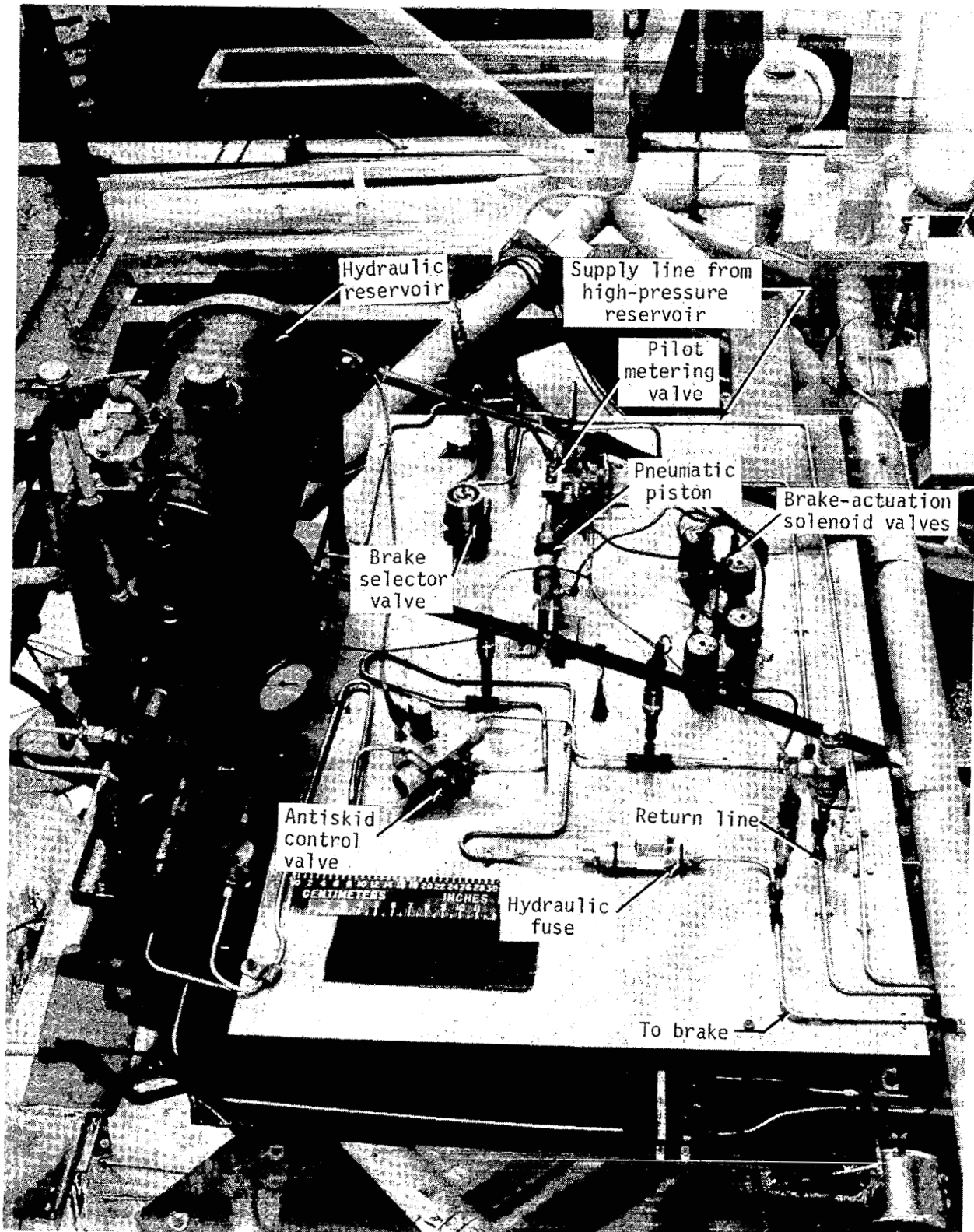
Figure 1.- Brake assembly.

L-81-9293.1



L-79-1976.2

Figure 2.- New and worn tread condition of six-groove, 40 x 14, type VII aircraft test tires.



L-76-5905.1

Figure 3.- Layout of braking system C on test carriage.

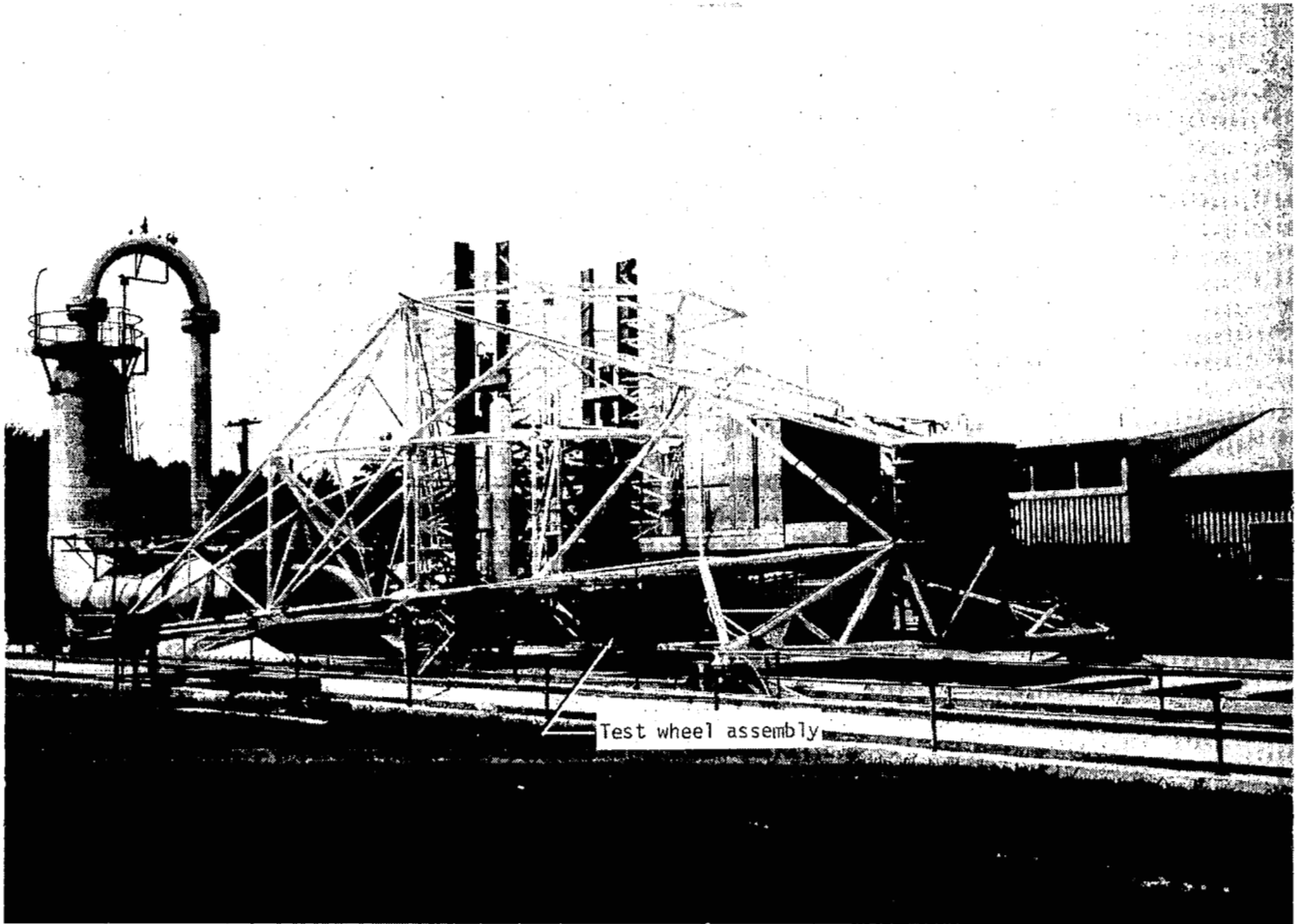
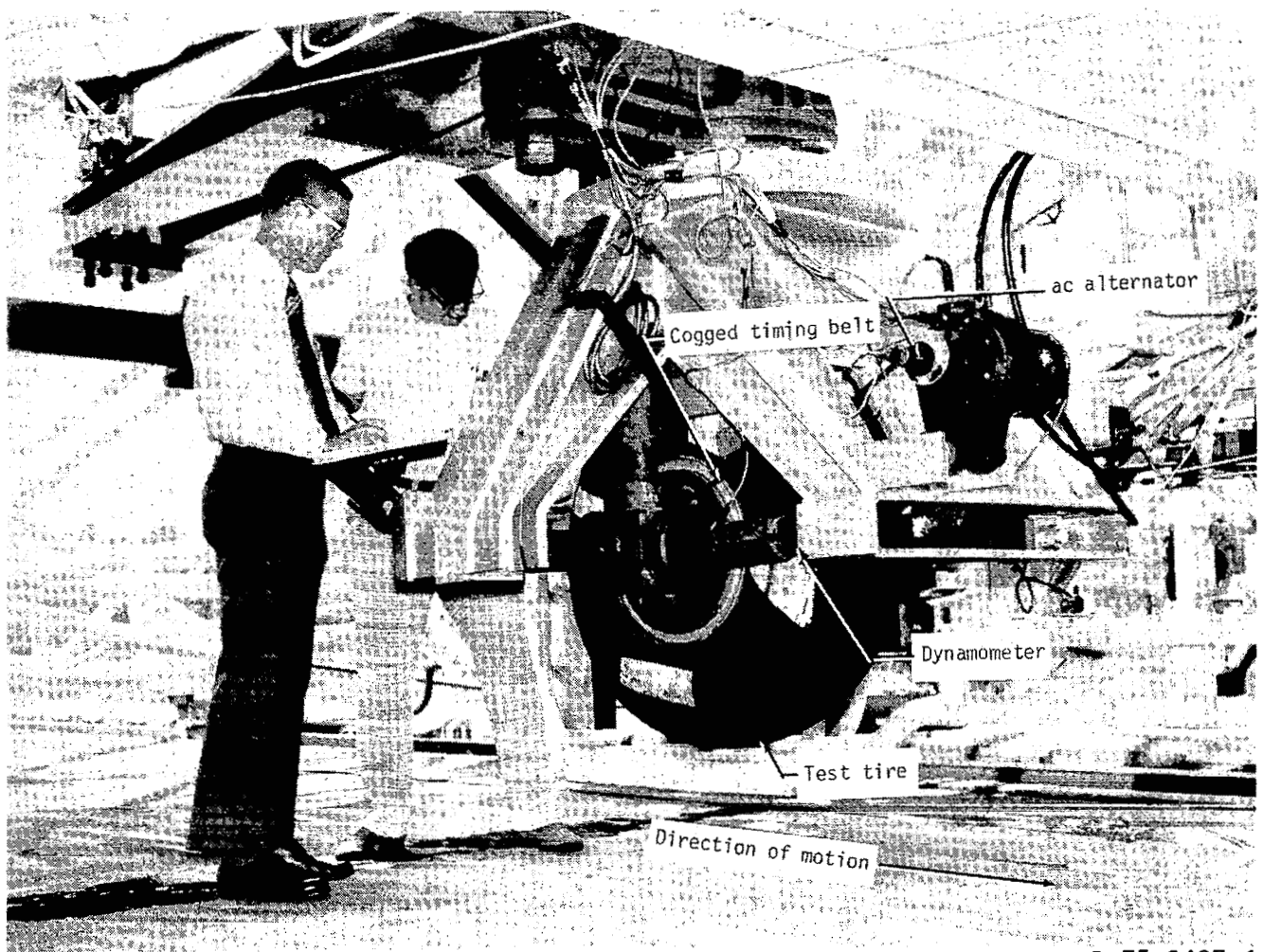


Figure 4.- Test carriage.

L-69-5860.1



L-75-3427.1

Figure 5.- Test tire and instrumented dynamometer.

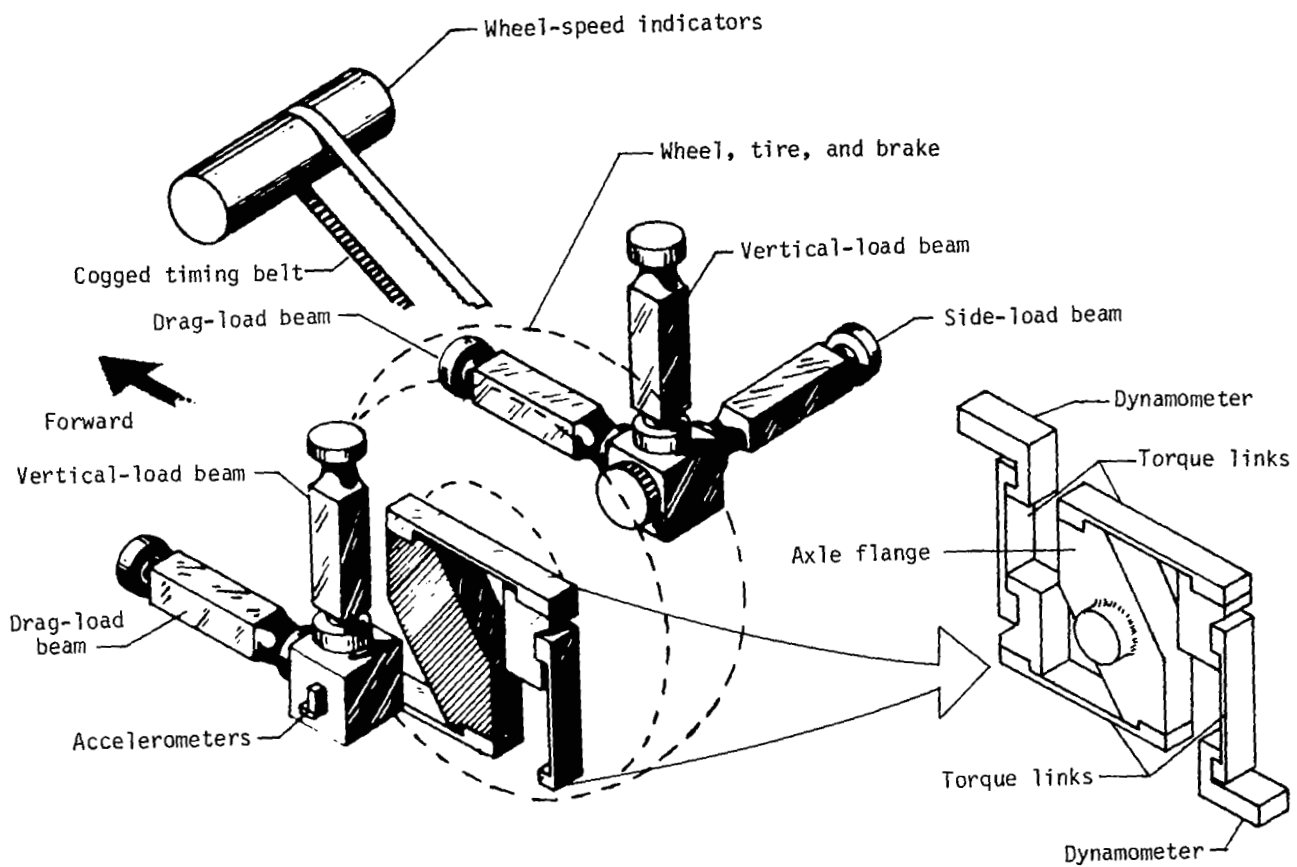
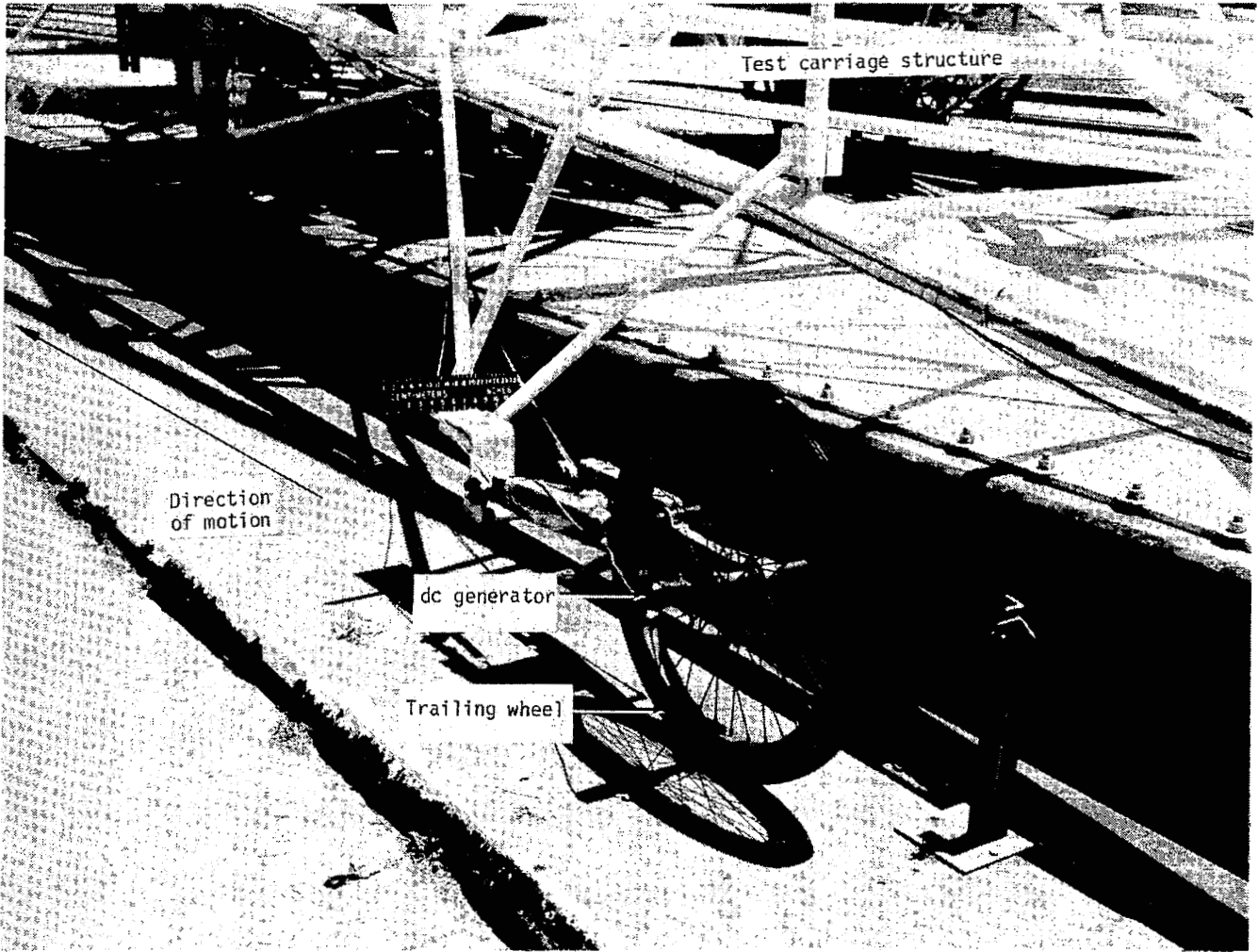


Figure 6.- Dynamometer details.



L-76-3786.1

Figure 7.- Lightweight trailing wheel used to measure carriage speed.

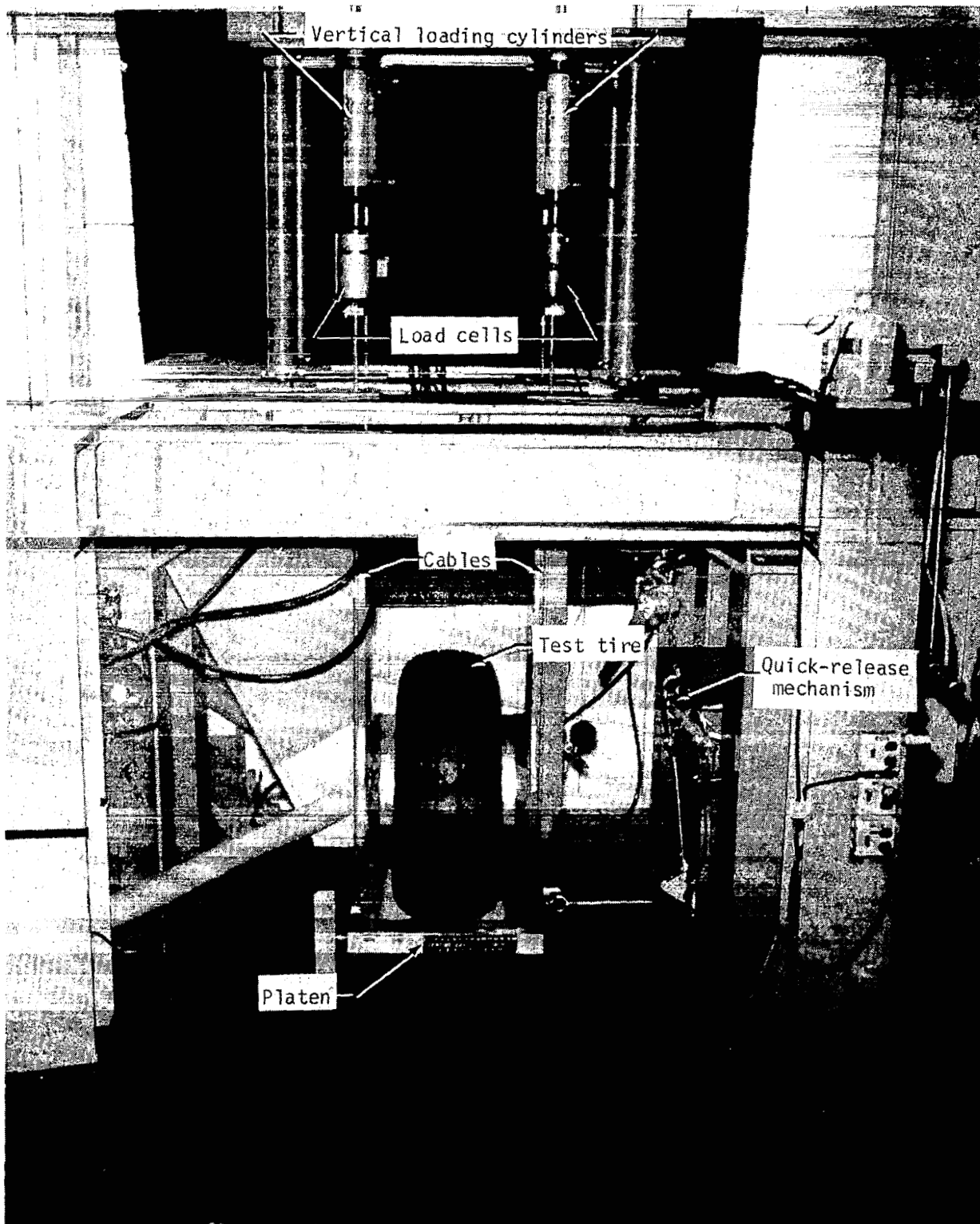


Figure 8.- Test tire mounted in tire vibration stand. L-81-569.1

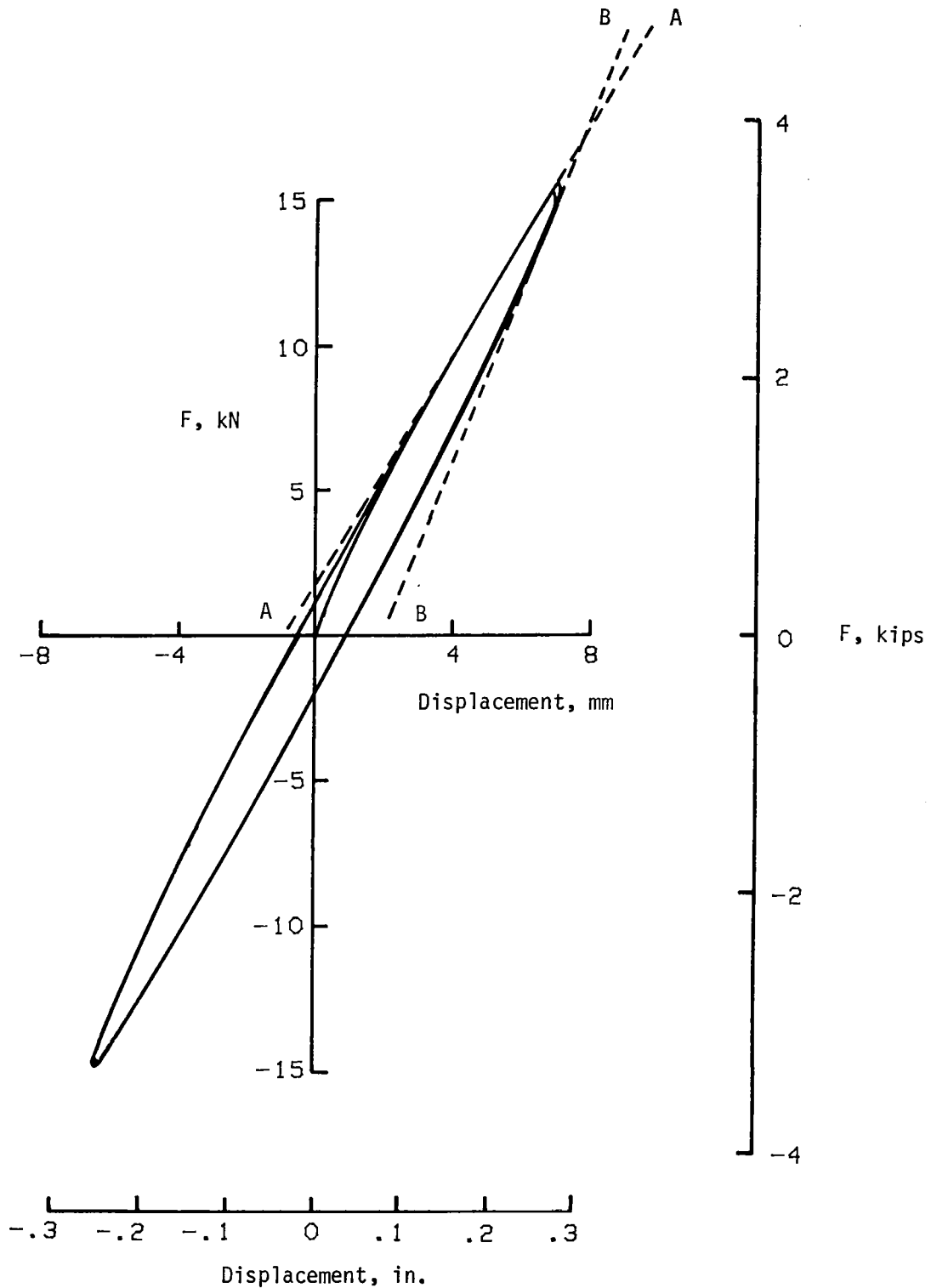
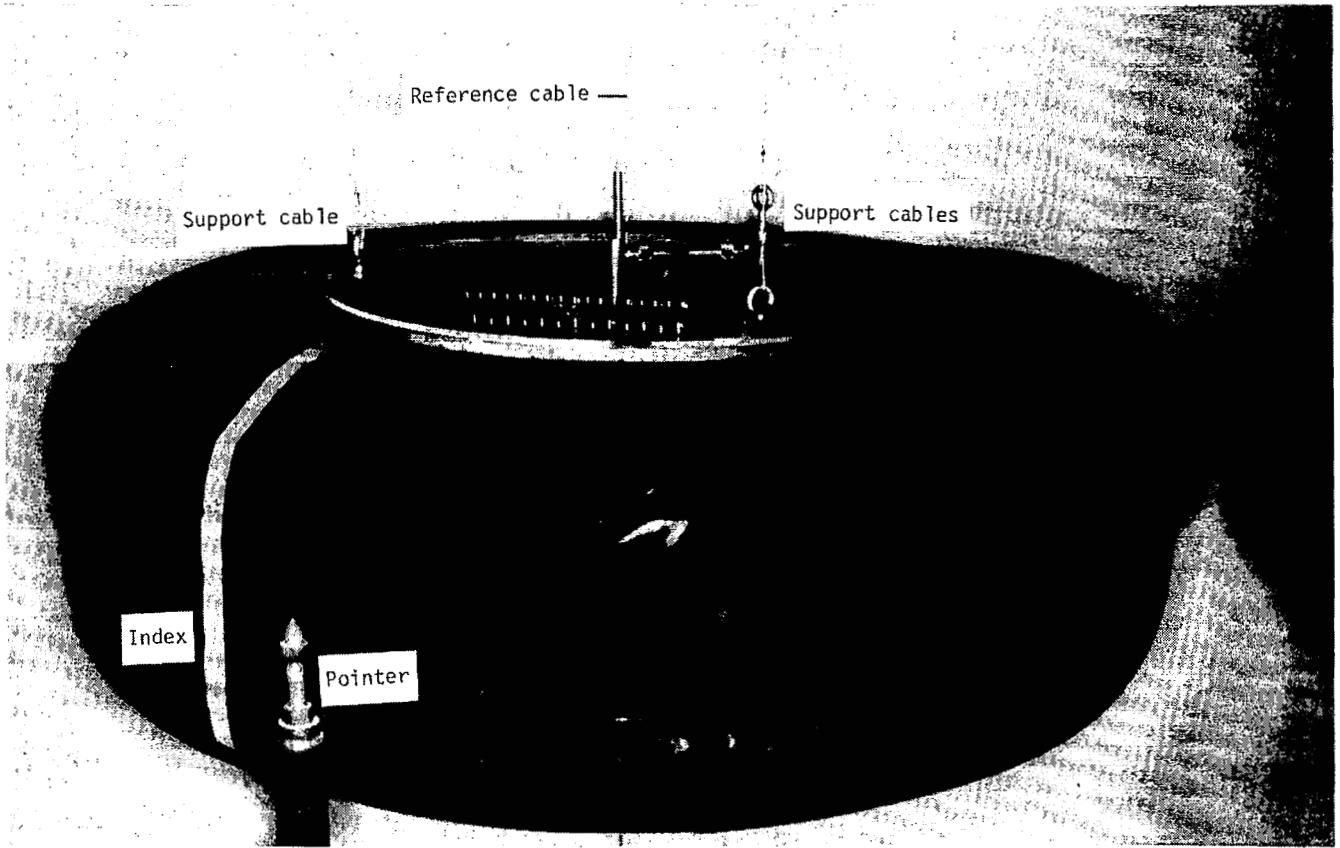
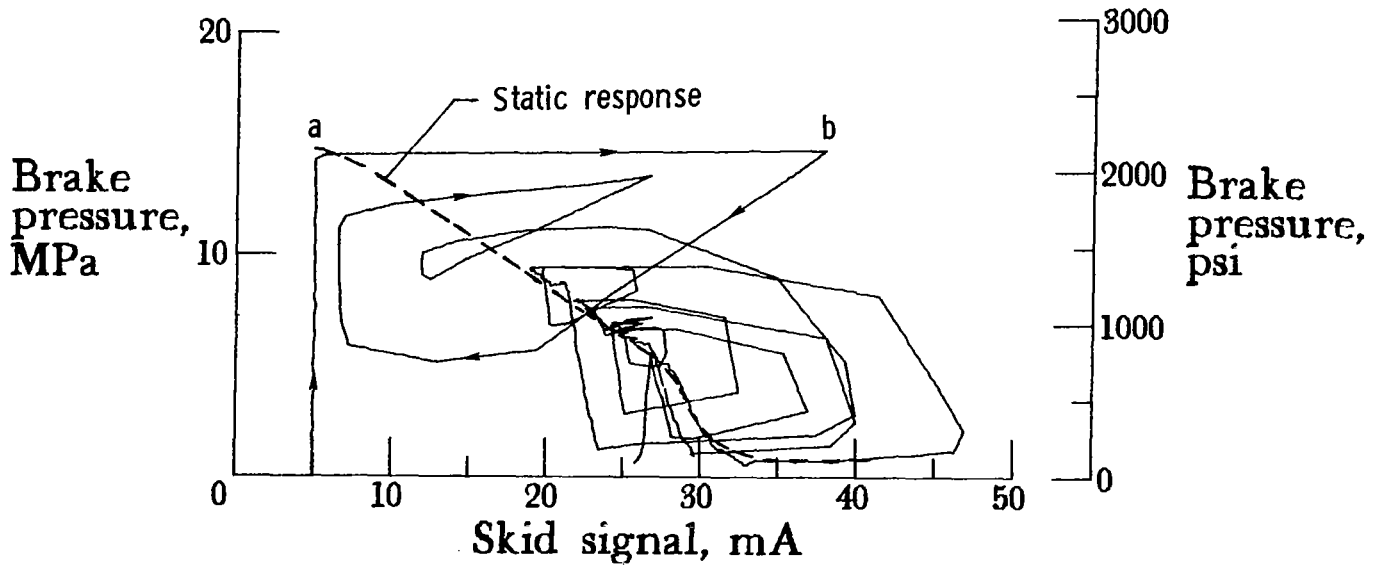


Figure 9.- Typical, static, fore-and-aft load-deflection curve showing how fore-and-aft spring rates are acquired: tire pressure, 965 kPa (140 psi); vertical load, 80.4 kN (18 080 lbf).

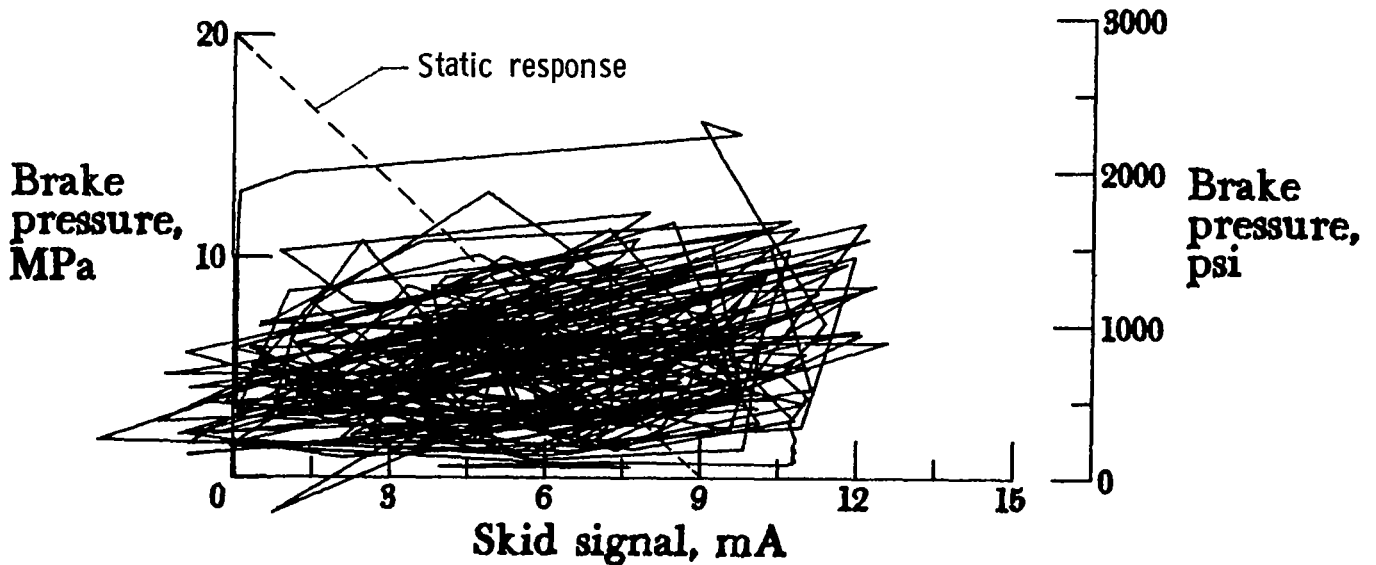


L-79-1537.1

Figure 10.- Test tire mounted on torsional pendulum.

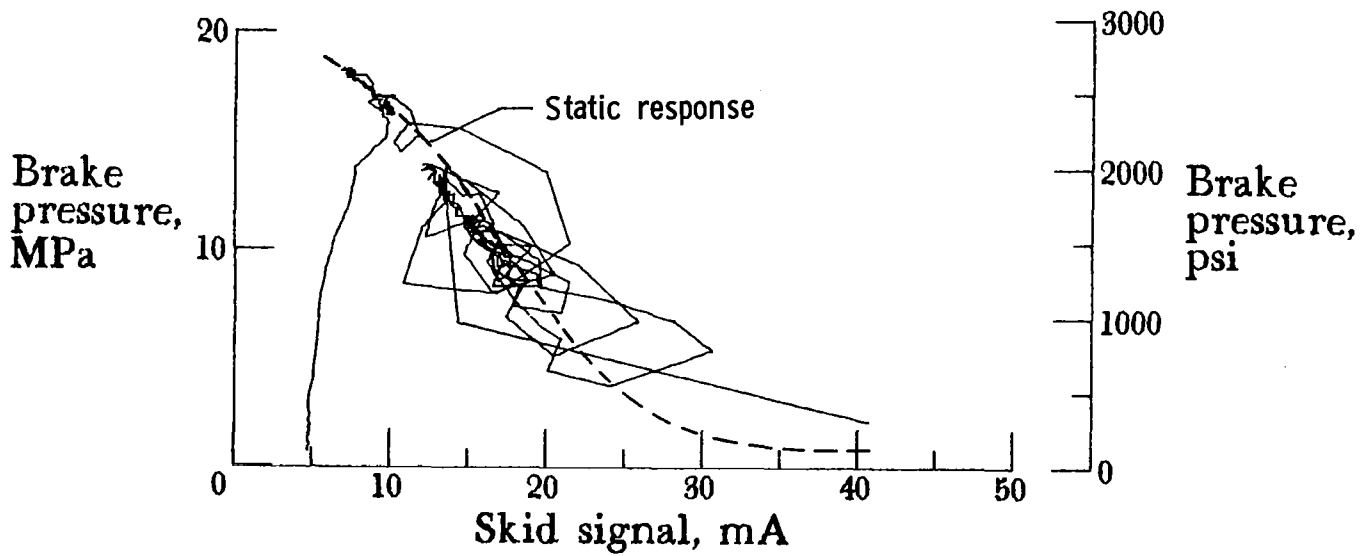


(a) System A: nominal carriage speed, 74 knots; vertical load, 75.6 kN (17 000 lbf); yaw angle, 0°; surface condition, damp; tire condition, new; brake pressure, 14 MPa (2000 psi); run A4.



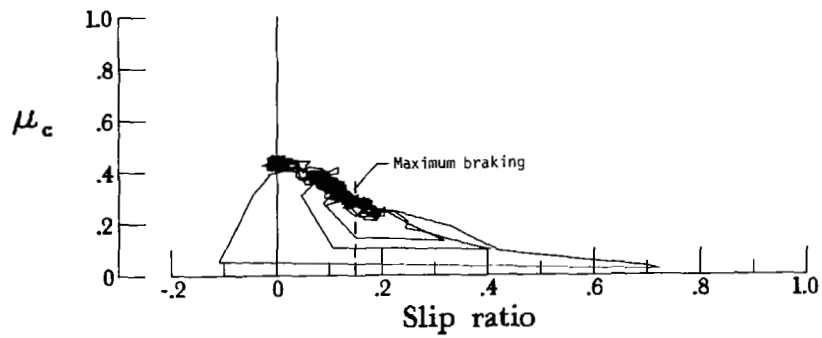
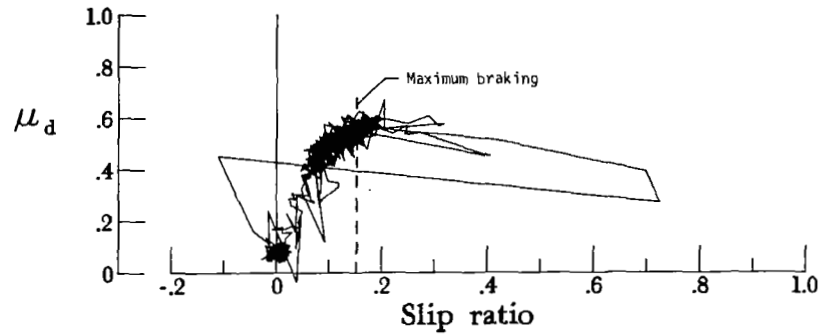
(b) System B: nominal carriage speed, 71 knots; vertical load, 63.2 kN (14 200 lbf); yaw angle, 0°; surface condition, damp; tire condition, new; brake pressure, 21 MPa (3000 psi); run A18.

Figure 11.- Typical dynamic response of antiskid control valves.



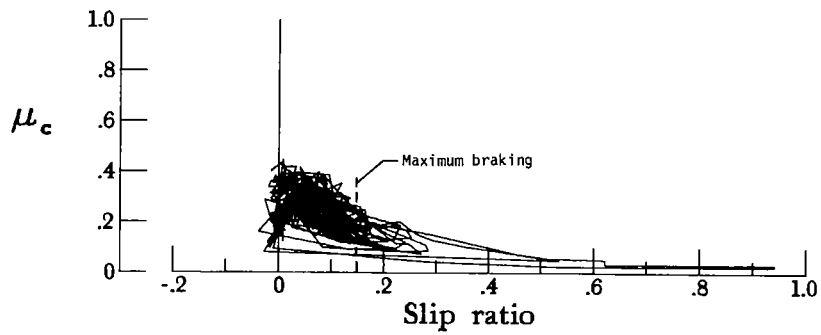
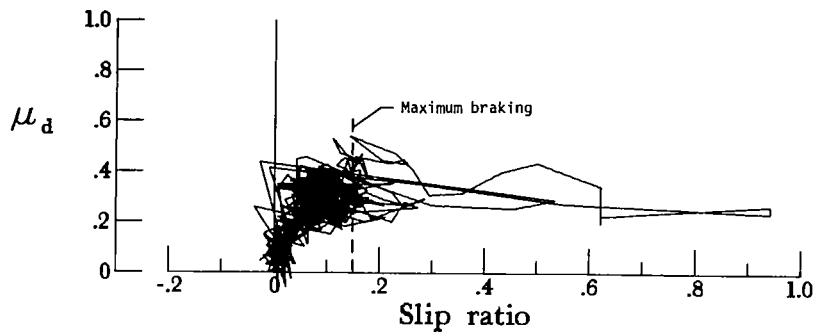
(c) System C: nominal carriage speed, 75 knots; vertical load, 85.0 kN (19 100 lbf); yaw angle, 0°; surface condition, dry; tire condition, new; brake pressure, 20 MPa (2900 psi); run A33.

Figure 11.- Concluded.



(a) System A: nominal carriage speed, 46 knots; vertical load, 83.6 kN (18 800 lbf); yaw angle, 6°; surface condition, dry; tire condition, new; brake pressure, 14 MPa (2000 psi); run A8.

Figure 12.- Typical examples of drag-force and cornering-force friction coefficients plotted against wheel slip ratio on dry and damp runway.



(b) System A: nominal carriage speed, 50 knots; vertical load, 82.3 kN (18 500 lbf); yaw angle, 6°; surface condition, damp; tire condition, new; brake pressure, 14 MPa (2000 psi); run A10.

Figure 12.- Concluded.

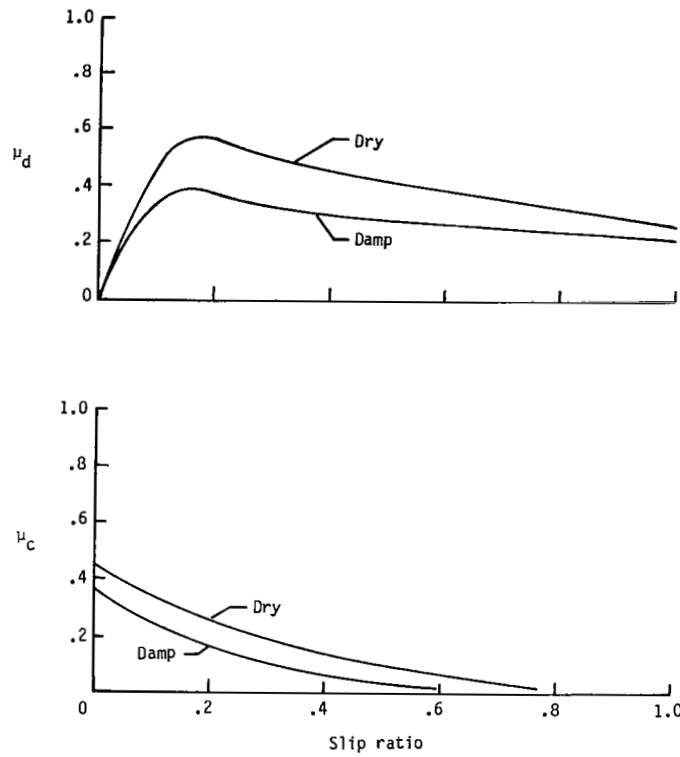


Figure 13.- Typical computer models of friction coefficient variations with wheel slip ratio.

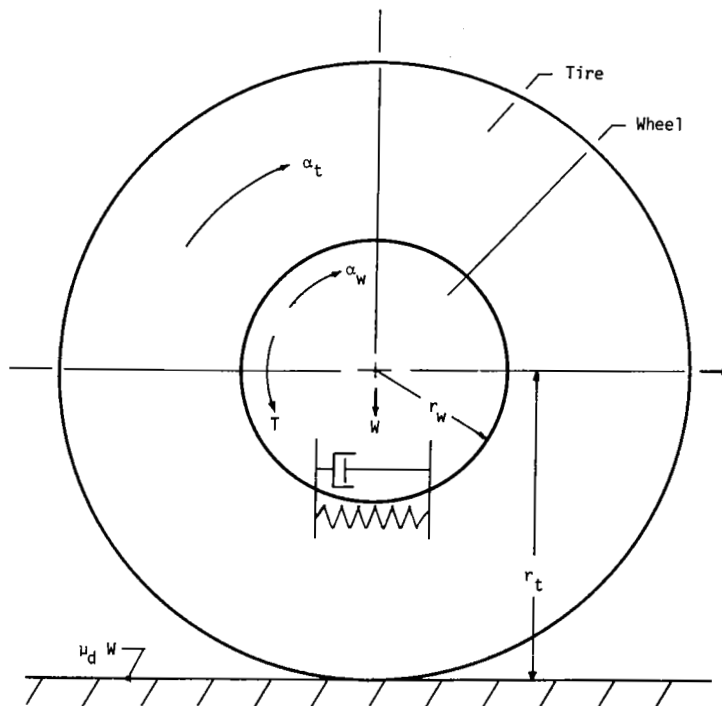


Figure 14.- Spring-damper system for modeling tire dynamics (ref. 4).

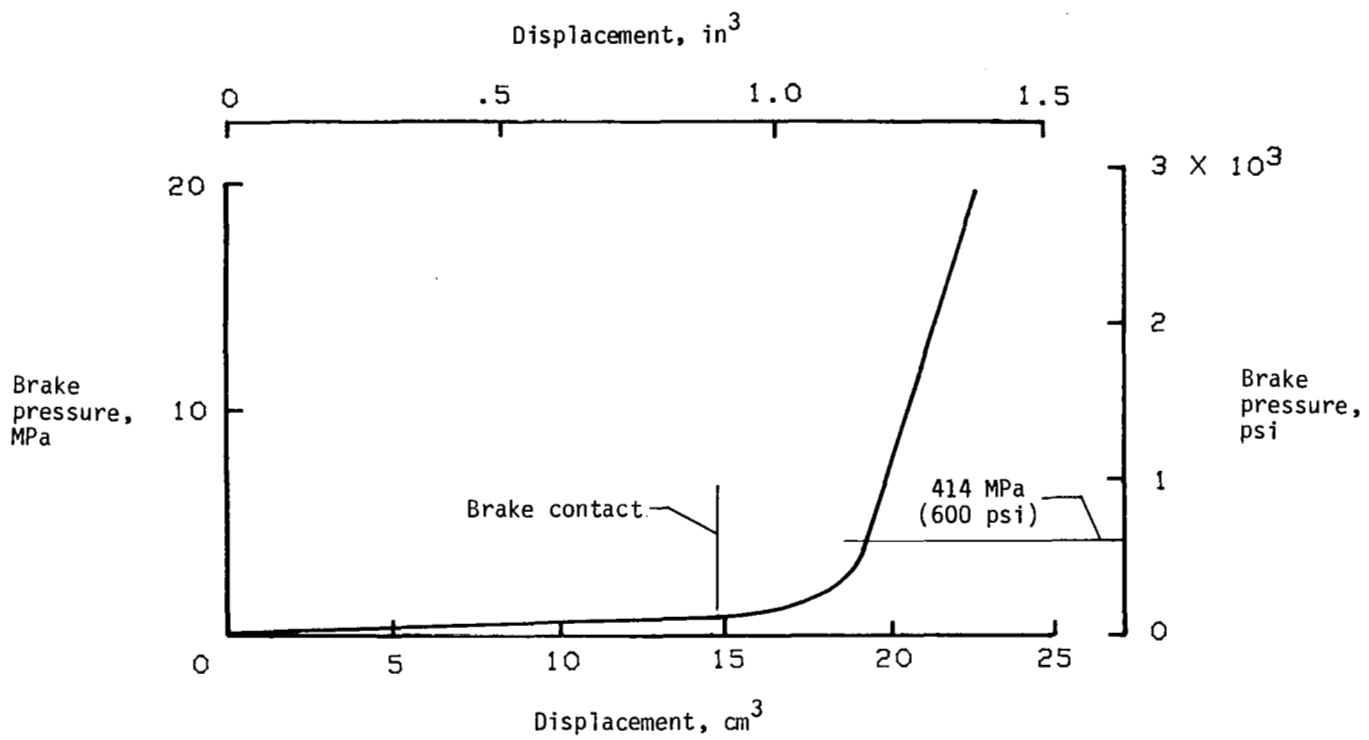
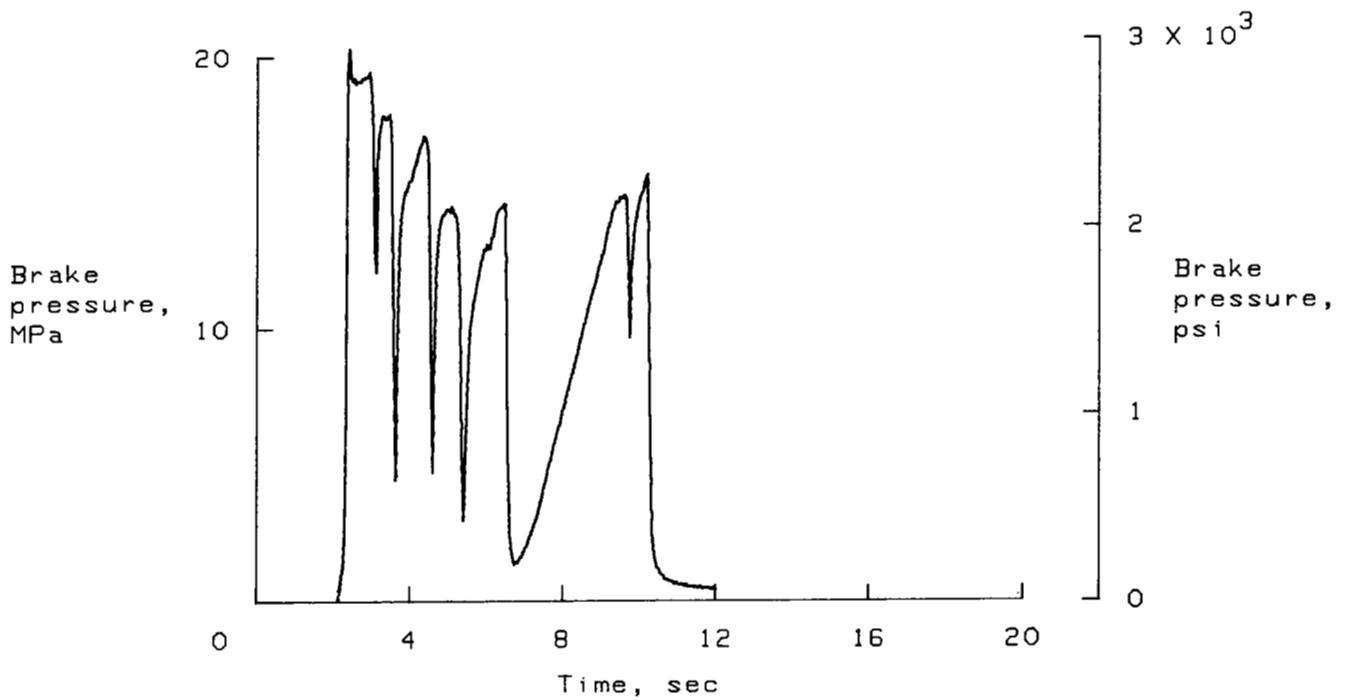
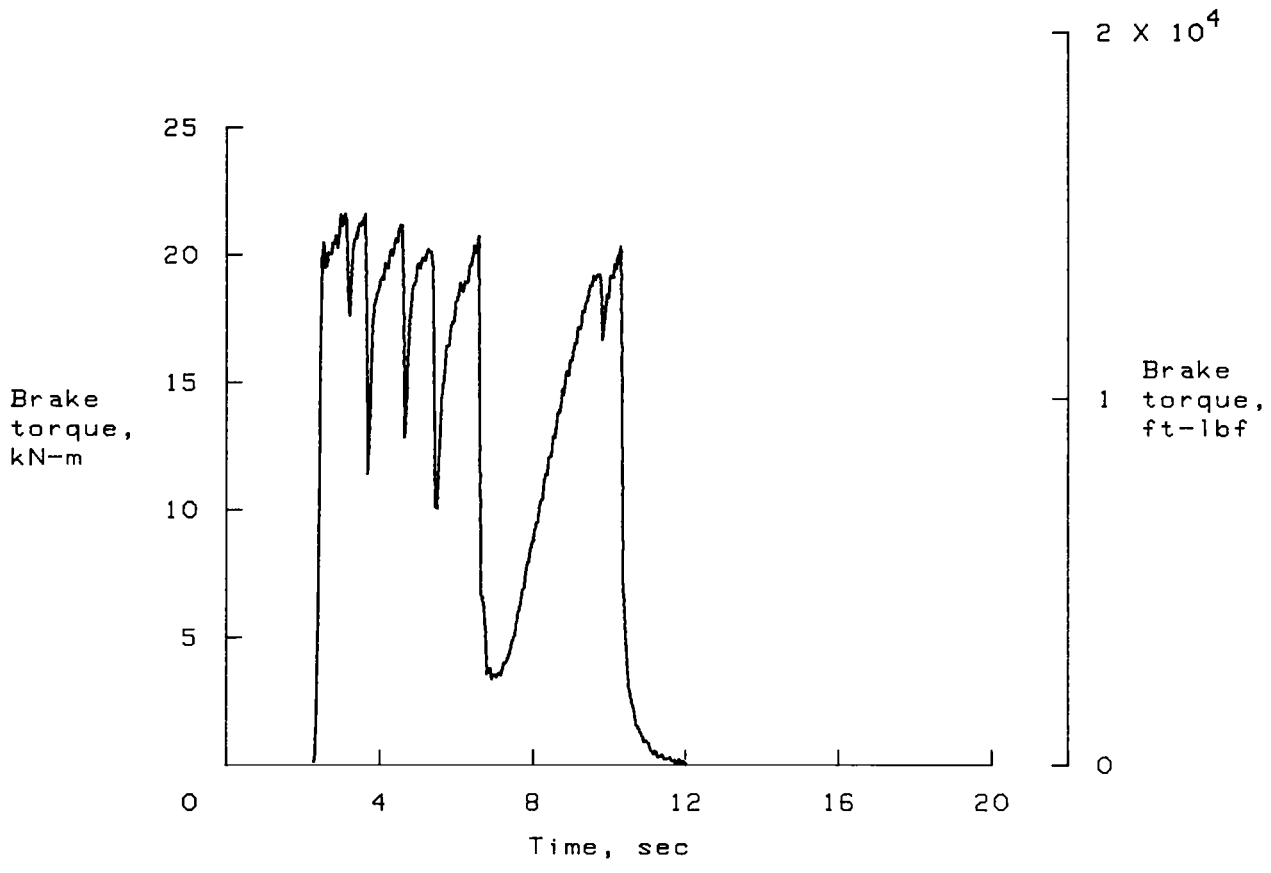


Figure 15.- Pressure-volume characteristics of DC-9 series 10 brake.



(a) Pressure input.

Figure 16.- Typical pressure and torque time histories: system C; nominal carriage speed, 54 knots; vertical load, 59.6 kN (13 400 lbf); yaw angle, 0°; surface condition, one damp spot on otherwise dry runway; tire condition, new; brake pressure, 21 MPa (3000 psi); run A26.



(b) Torque output.

Figure 16.- Concluded.

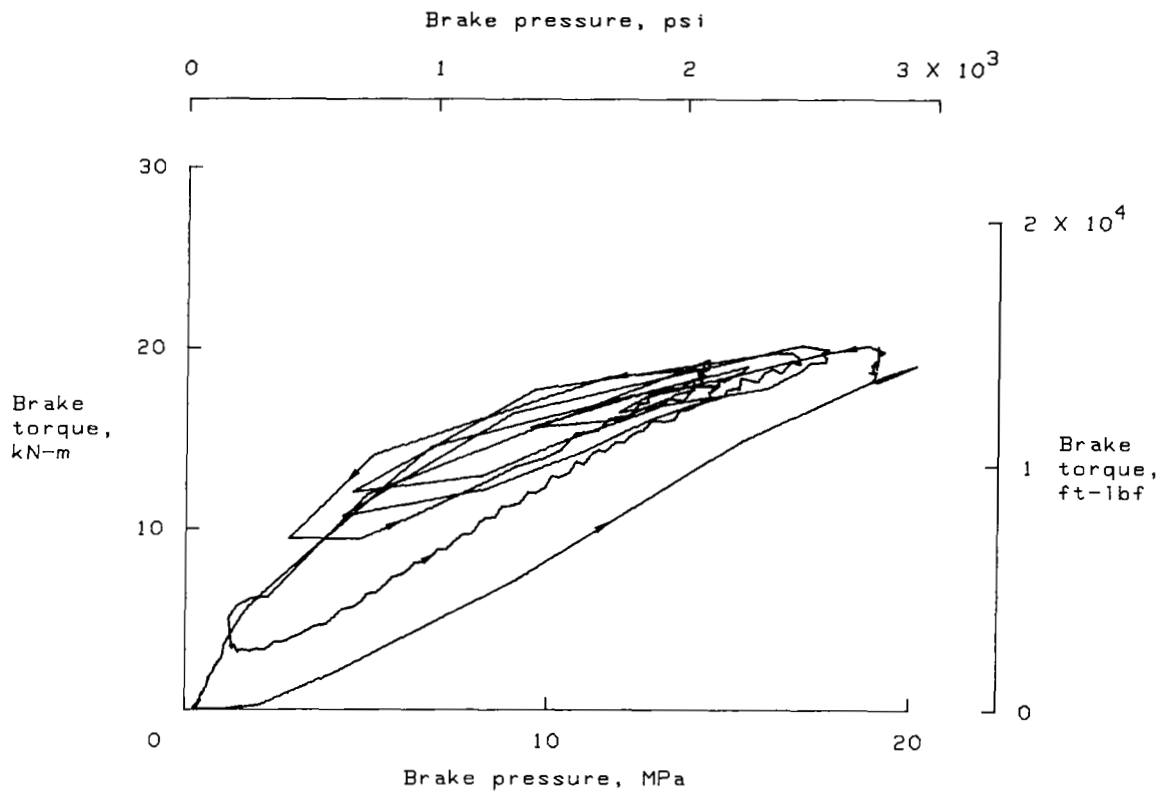
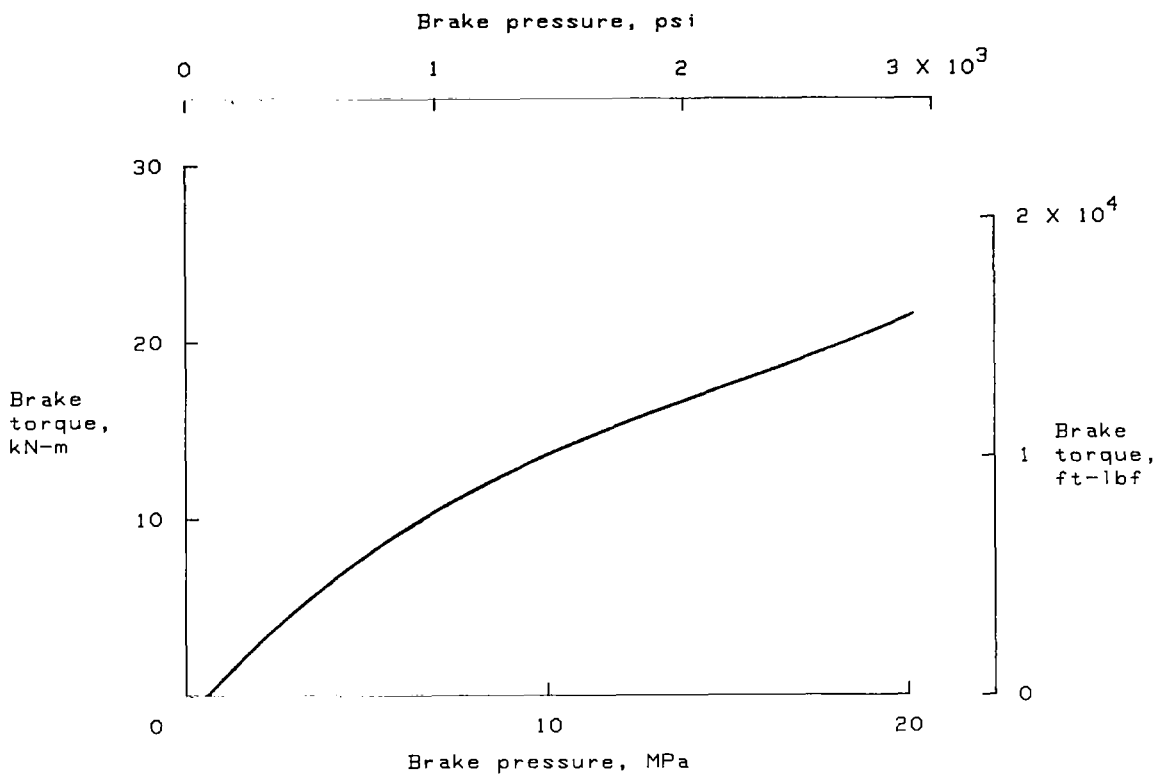
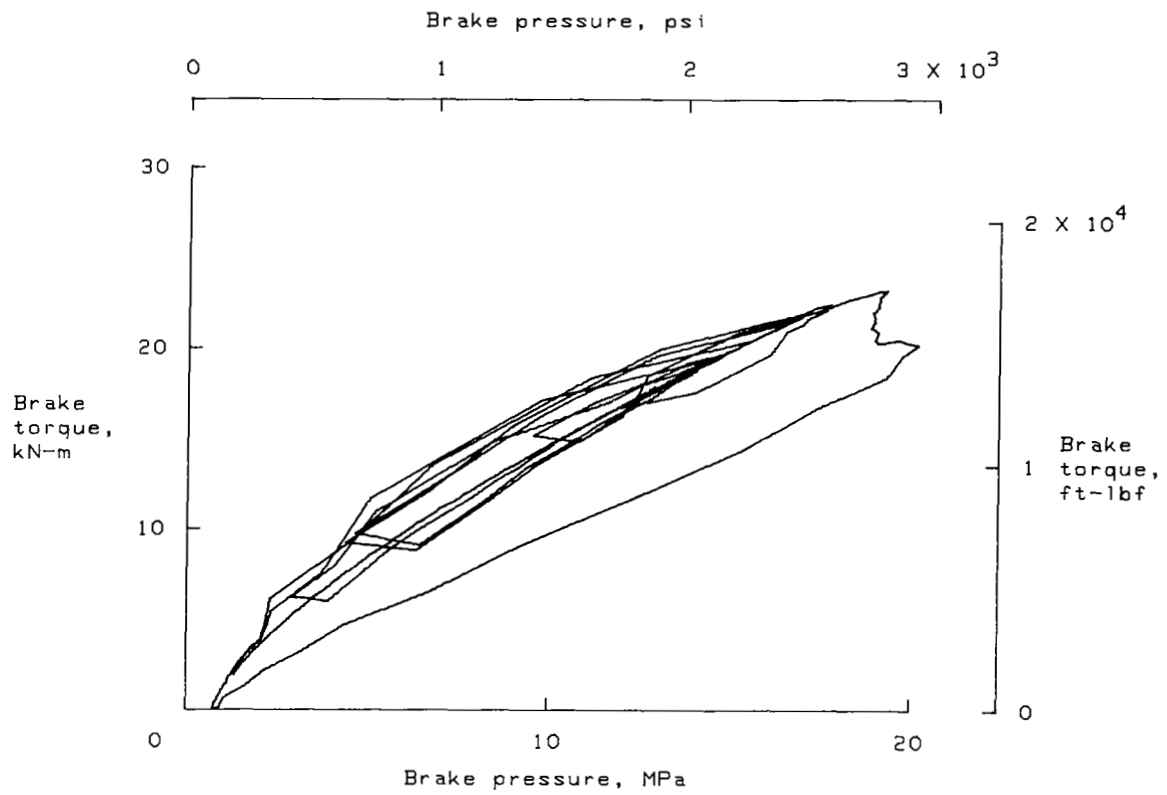


Figure 17.- Pressure-torque relationship: system C; nominal carriage speed, 54 knots; vertical load, 59.6 kN (13 400 lbf); yaw angle, 0°; surface condition, one damp spot on otherwise dry runway; tire condition, new; brake pressure, 21 MPa (3000 psi); run A26.



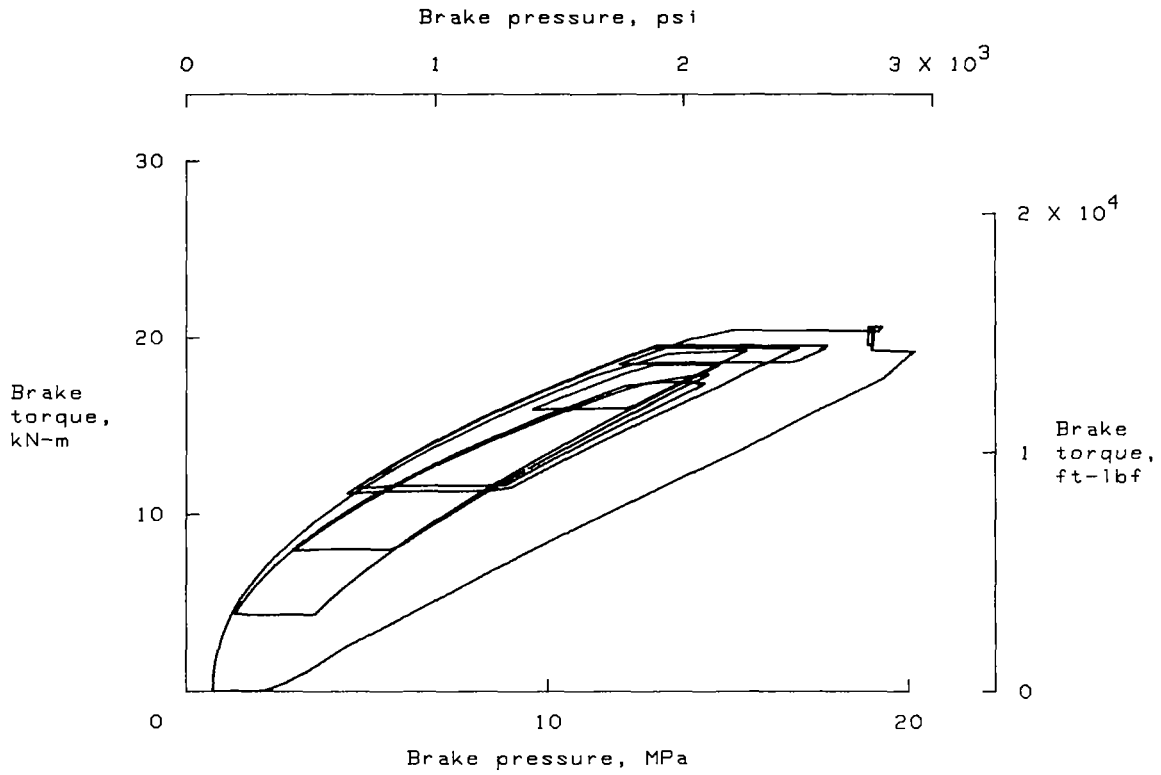
(a) Undamped, nonlinear spring.

Figure 18.- Computer model pressure-torque responses, with pressure input from figure 16(a).



(b) Linear spring with viscous damping.

Figure 18.- Continued.



(c) Variable nonlinear spring with hysteresis memory functions.

Figure 18.- Concluded.

## APPENDIX A

### PRESSURE, TORQUE, AND FRICTION FIGURES

Pressure, torque, and friction data are presented in figures A1 to A37 which describe the dynamic response characteristics of the antiskid braking systems included in this study. The figures include plots of the brake pressure as a function of skid signal, brake torque as a function of brake pressure, drag-force friction coefficient as a function of wheel slip ratio, and cornering-force friction coefficient as a function of wheel slip ratio. These data are provided for the convenience of the reader in studying the dynamic response characteristic of antiskid braking systems in detail.

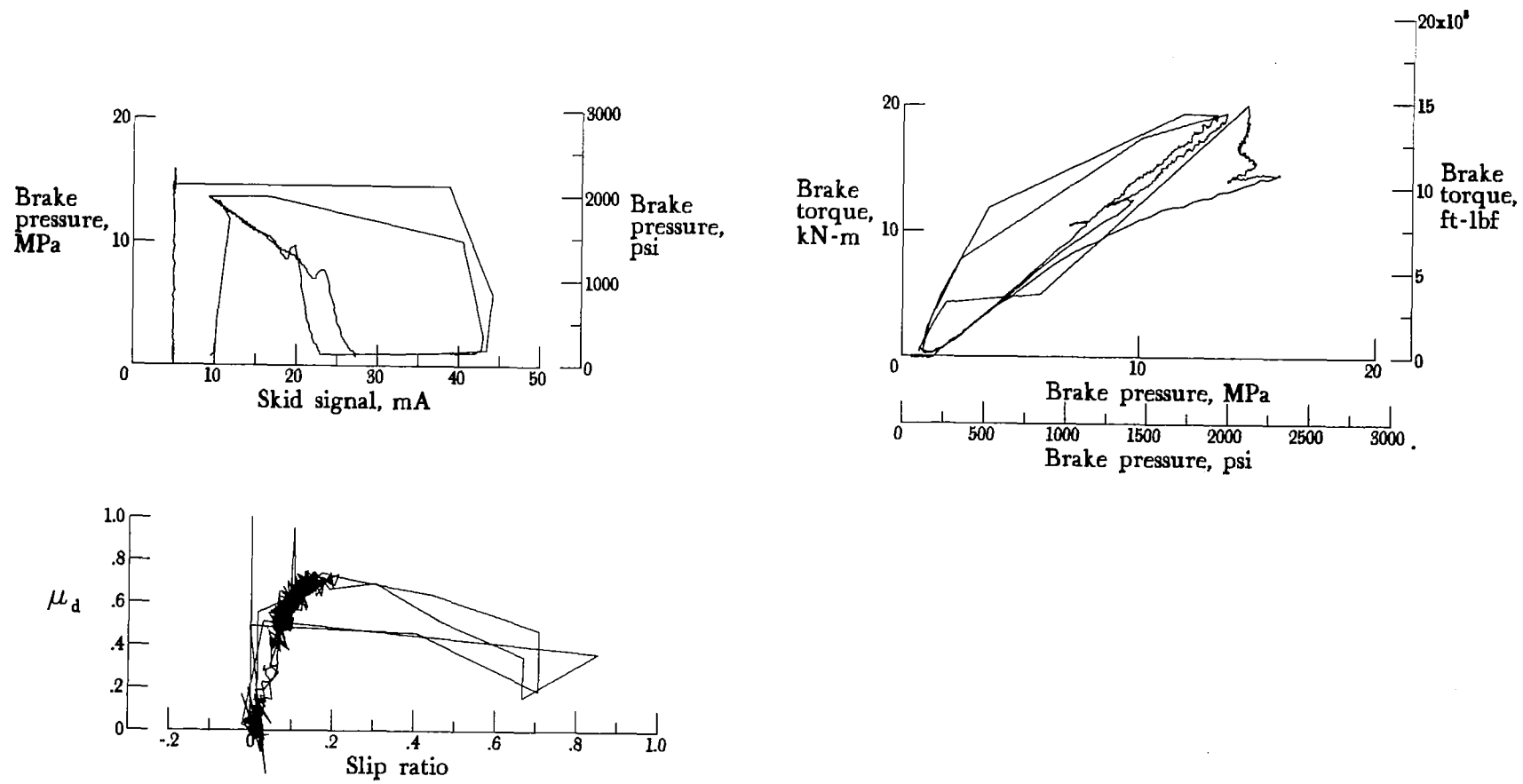


Figure A1.- Antiskid system dynamic response: system A; nominal carriage speed, 46 knots; vertical load, 54.7 kN (12 300 lbf); yaw angle, 0°; surface condition, dry; tire condition, new; brake pressure, 14 MPa (2000 psi).

Data not available

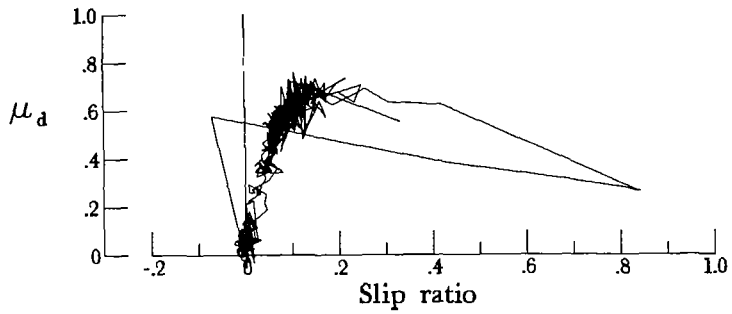
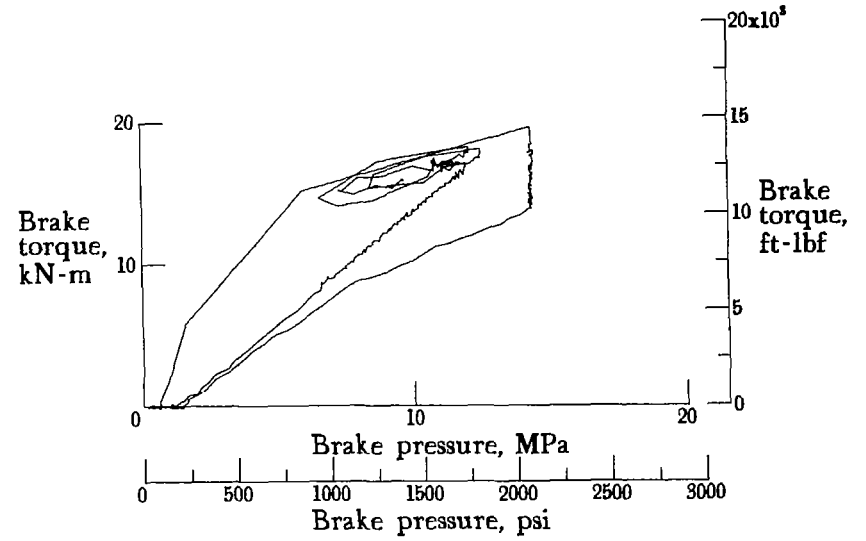


Figure A2.- Antiskid system dynamic response: system A; nominal carriage speed, 73 knots; vertical load, 60.5 kN (13 600 lbf); yaw angle, 0°; surface condition, dry; tire condition, new; brake pressure, 14 MPa (2000 psi).

Data not available

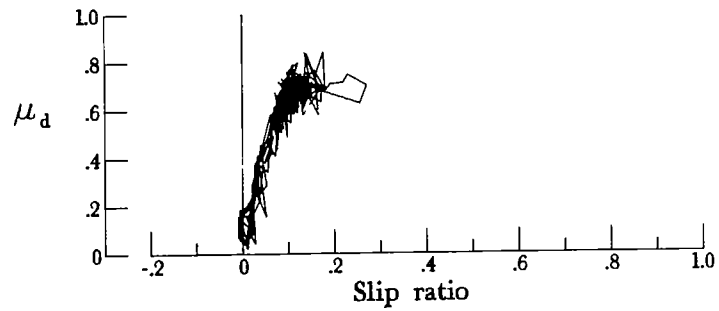
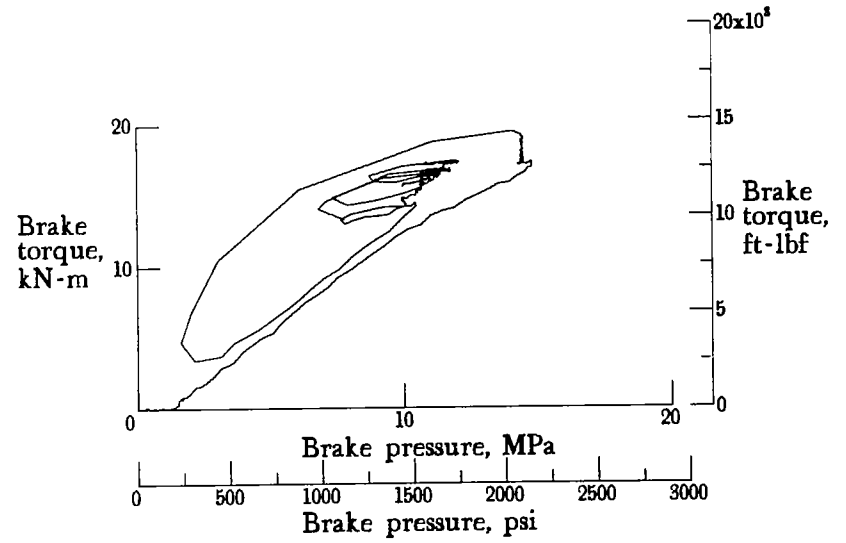


Figure A3.- Antiskid system dynamic response: system A; nominal carriage speed, 98 knots; vertical load, 60.9 kN (13 700 lbf); yaw angle, 0°; surface condition, dry; tire condition, new; brake pressure, 14 MPa (2000 psi).

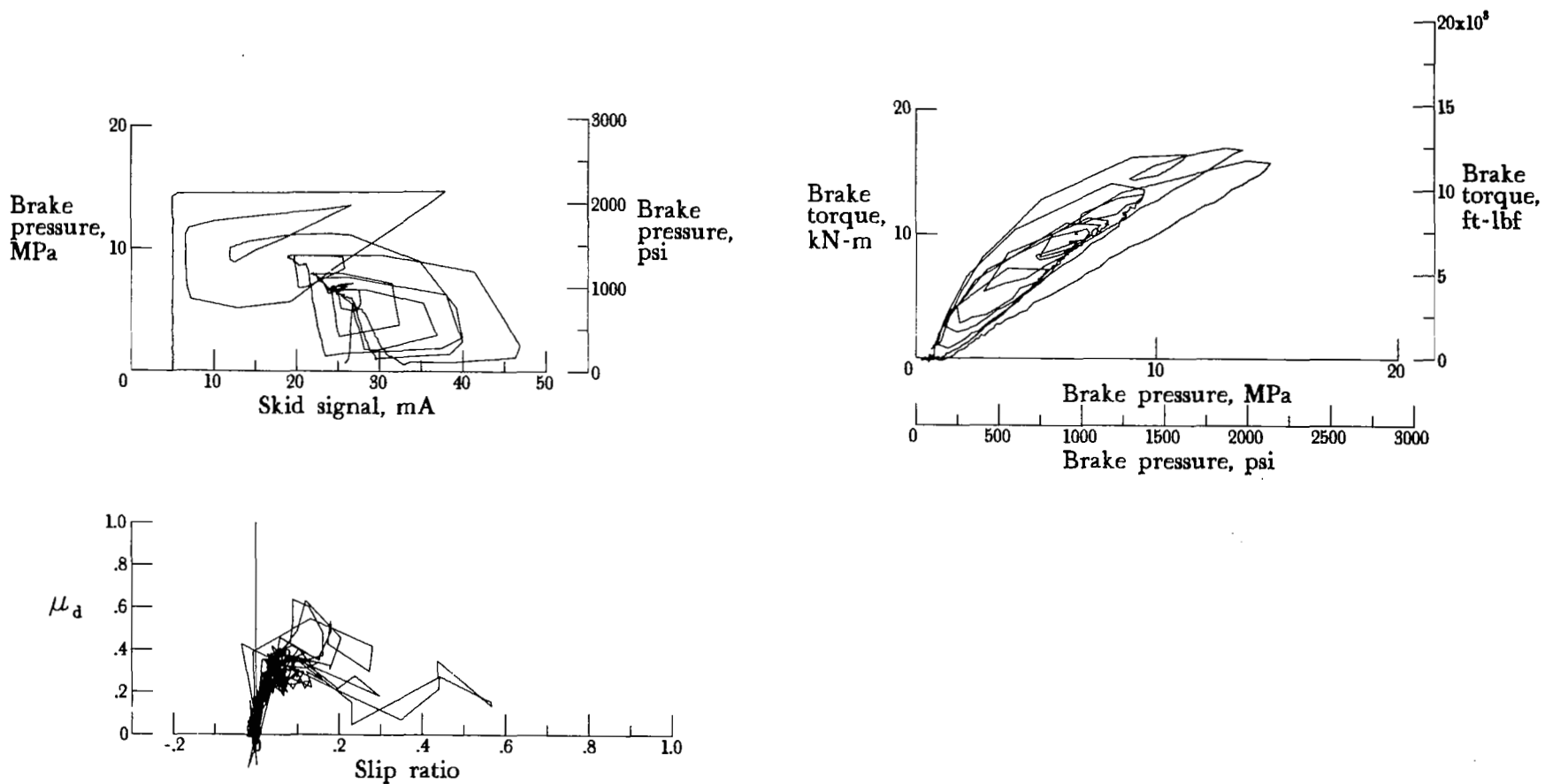


Figure A4.- Antiskid system dynamic response: system A; nominal carriage speed, 74 knots; vertical load, 75.6 kN (17 000 lbf); yaw angle, 0°; surface condition, damp; tire condition, new; brake pressure, 14 MPa (2000 psi).

Data not available

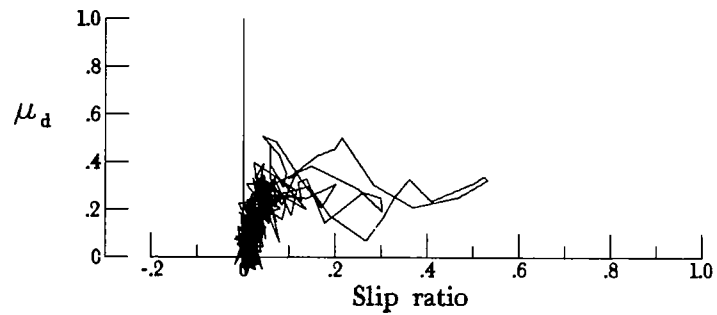
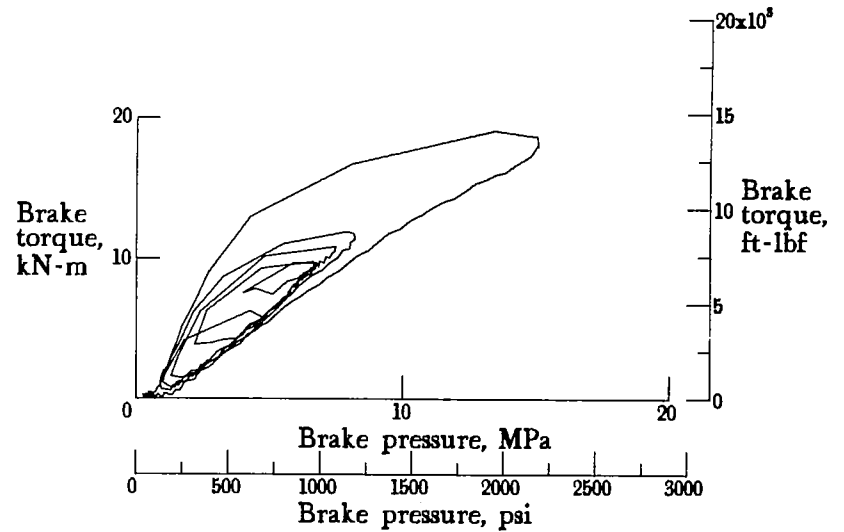


Figure A5.- Antiskid system dynamic response: system A; nominal carriage speed, 98 knots; vertical load, 79.6 kN (17 900 lbf); yaw angle, 0°; surface condition, damp; tire condition, new; brake pressure, 14 MPa (2000 psi).

Data not available

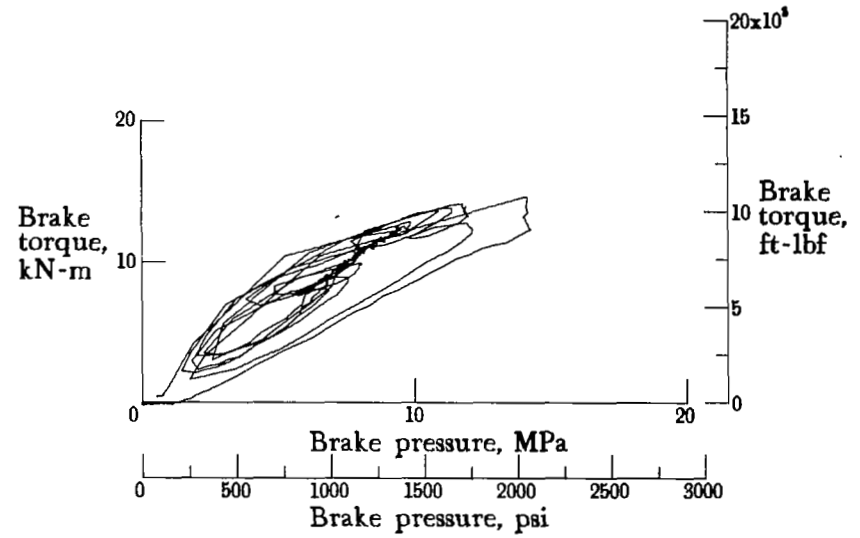
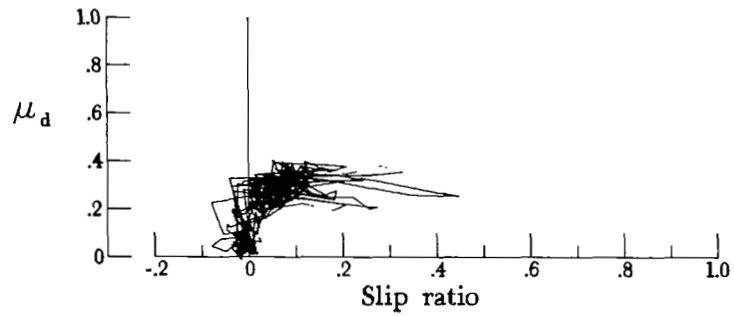


Figure A6.- Antiskid system dynamic response: system A; nominal carriage speed, 47 knots; vertical load, 92.1 kN (20 700 lbf); yaw angle, 0°; surface condition, flooded; tire condition, new; brake pressure, 14 MPa (2000 psi).

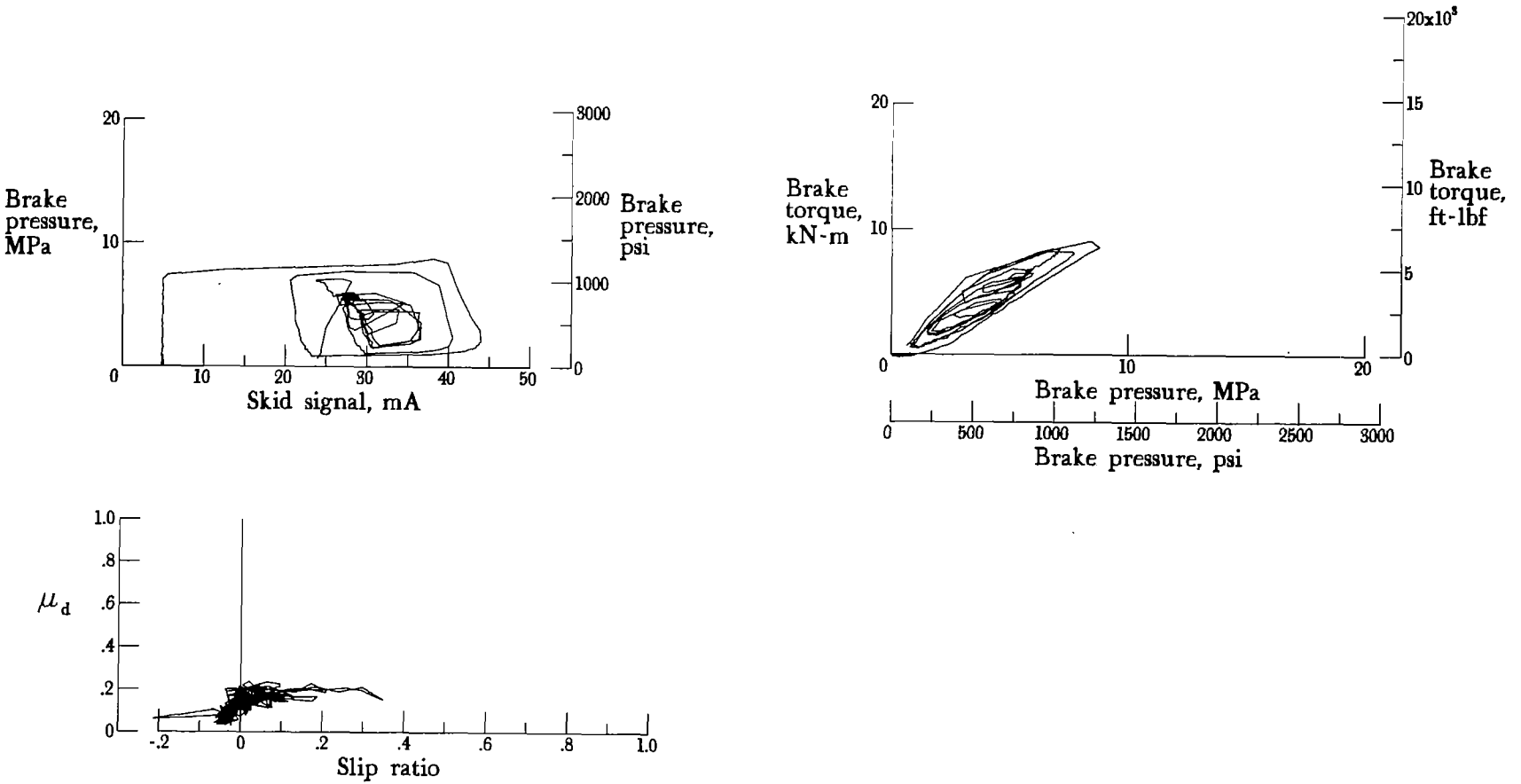


Figure A7.- Antiskid system dynamic response: system A; nominal carriage speed, 76 knots; vertical load, 114.3 kN (25 700 lbf); yaw angle, 0°; surface condition, flooded; tire condition, new; brake pressure, 14 MPa (2000 psi).

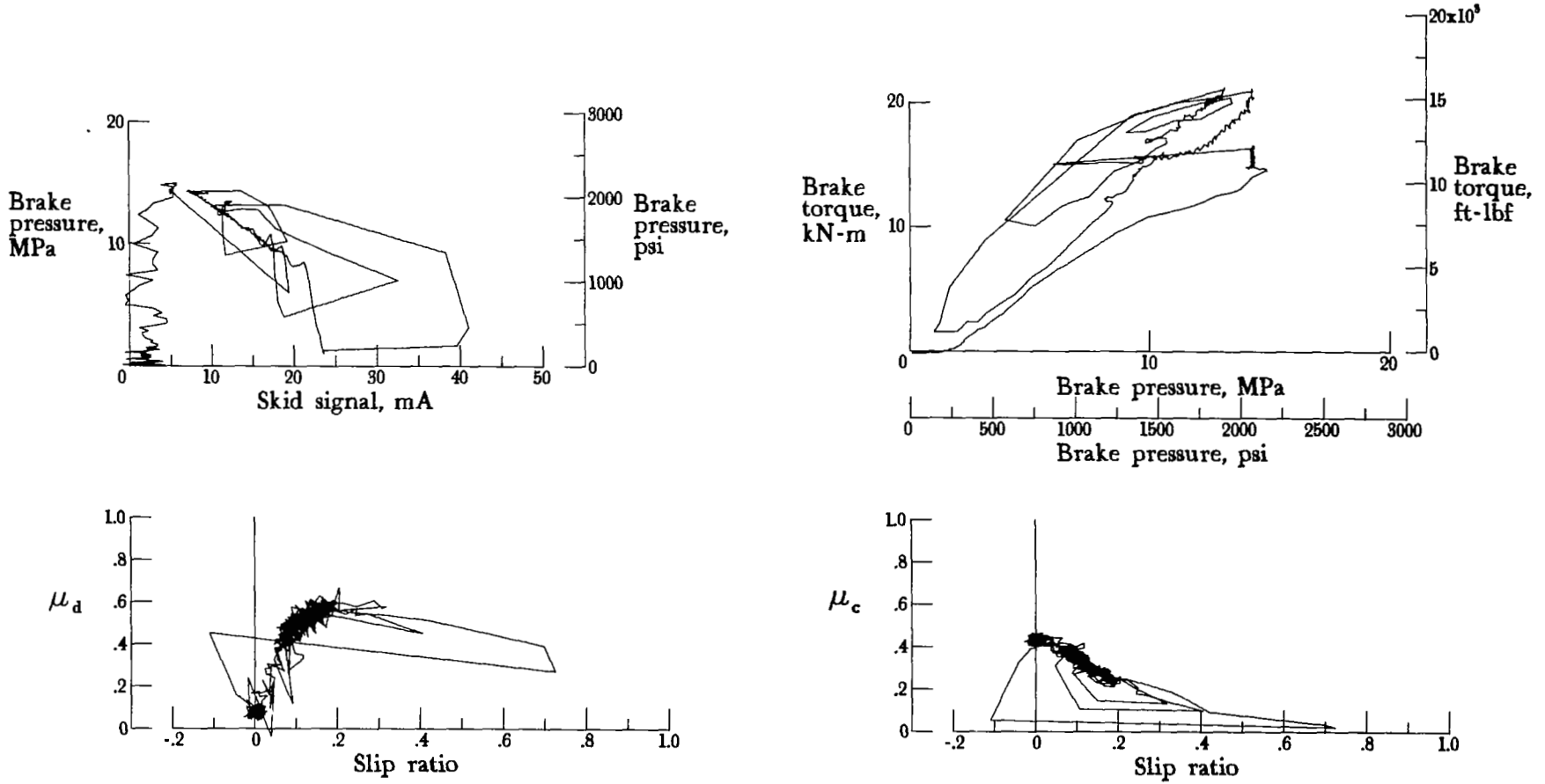


Figure A8.- Antiskid system dynamic response: system A; nominal carriage speed, 46 knots; vertical load, 83.6 kN (18 800 lbf); yaw angle, 6°; surface condition, dry; tire condition, new; brake pressure, 14 MPa (2000 psi).

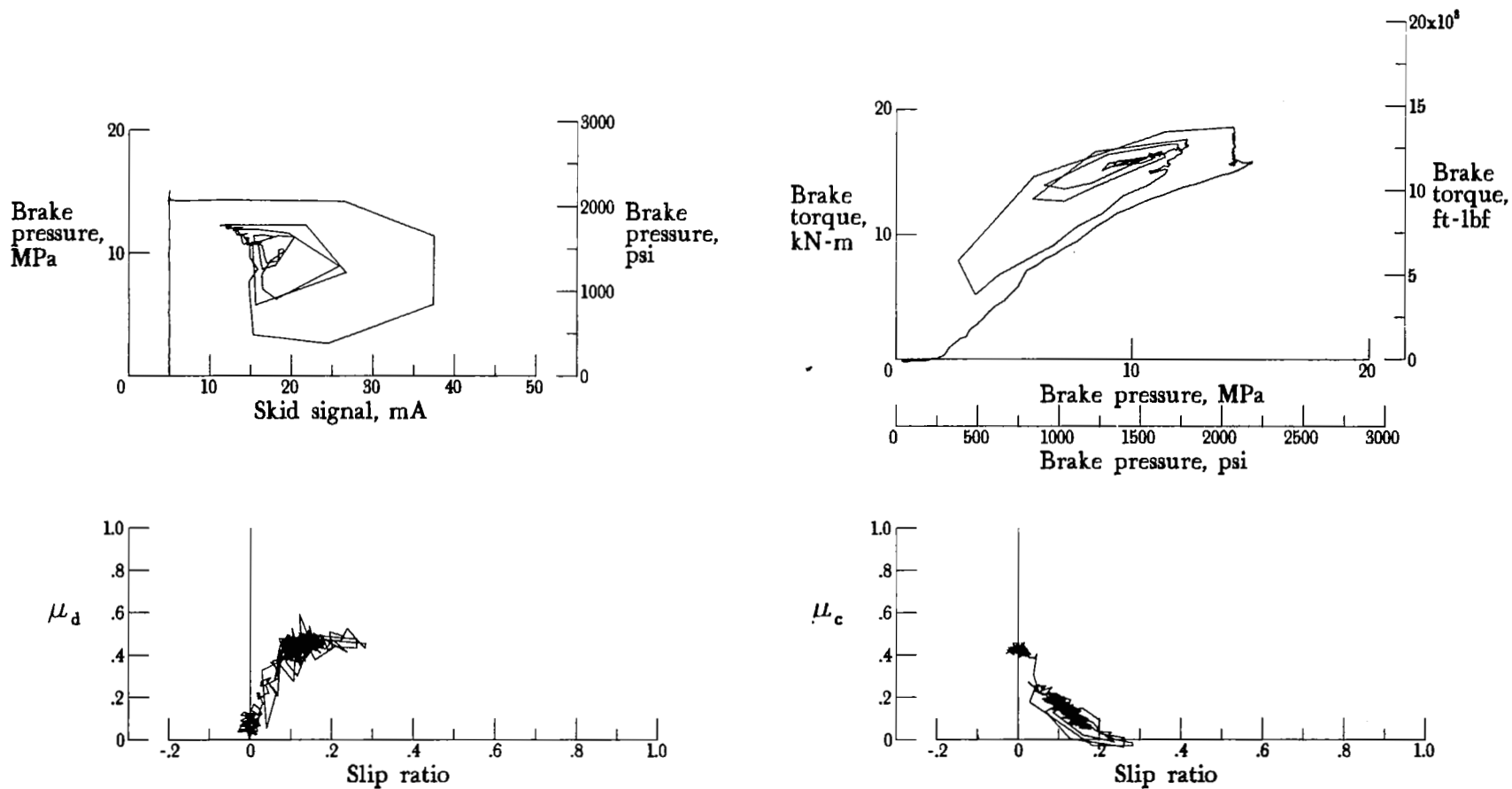


Figure A9.- Antiskid system dynamic response: system A; nominal carriage speed, 74 knots; vertical load, 81.4 kN (19 300 lbf); yaw angle, 6°; surface condition, dry; tire condition, new; brake pressure, 14 MPa (2000 psi).

Data not available

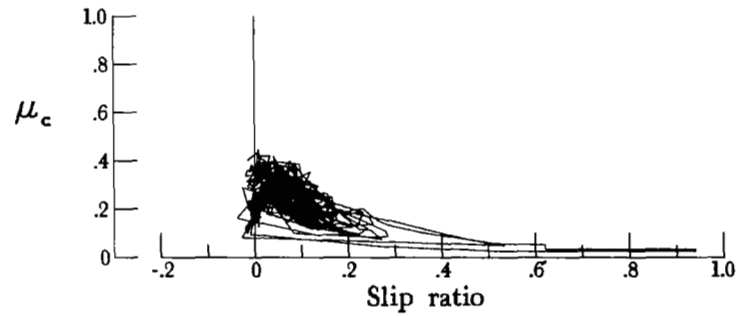
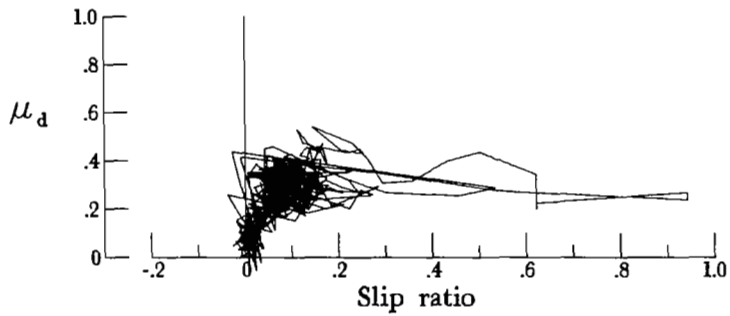
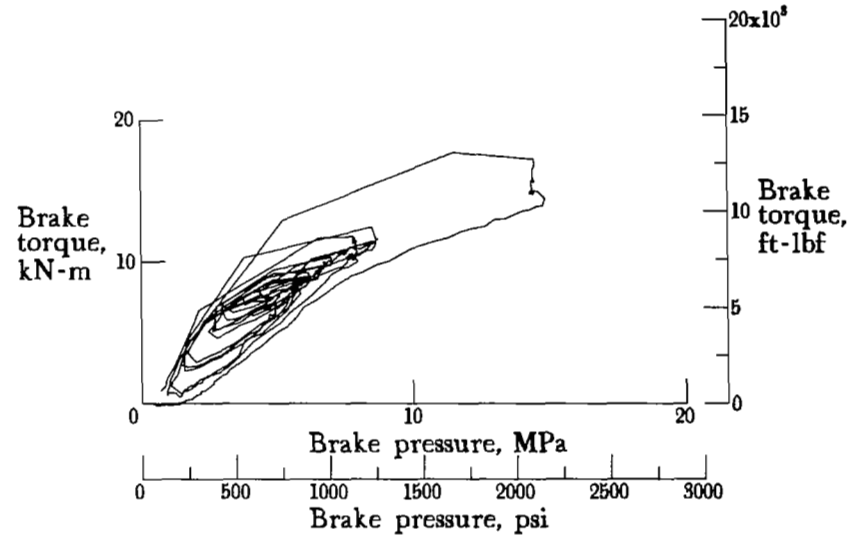


Figure A10.- Antiskid system dynamic response: system A; nominal carriage speed, 50 knots; vertical load, 82.3 kN (18 500 lbf); yaw angle, 6°; surface condition, damp; tire condition, new; brake pressure, 14 MPa (2000 psi).

Data not available

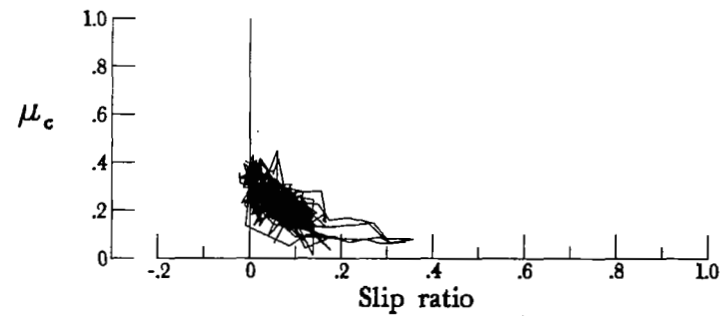
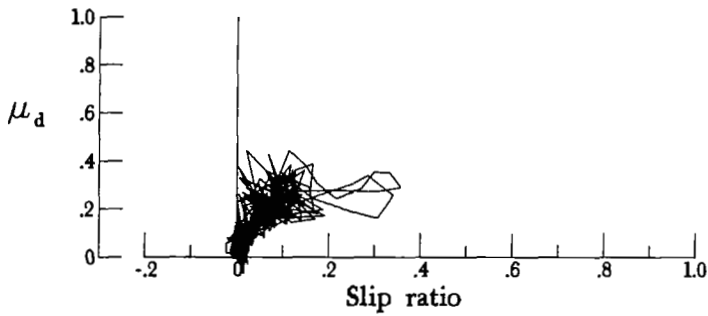
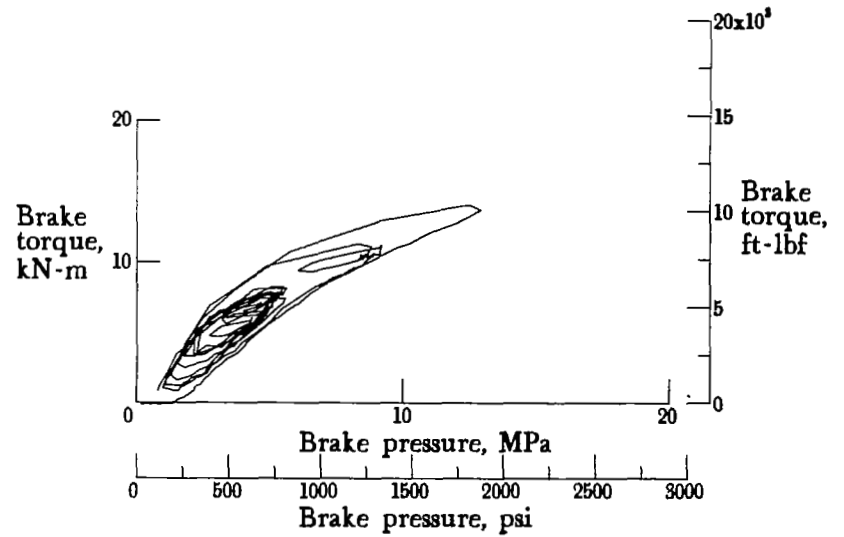


Figure A11.- Antiskid system dynamic response: system A; nominal carriage speed, 75 knots; vertical load, 81.8 kN (18 400 lbf); yaw angle, 6°; surface condition, damp; tire condition, new; brake pressure, 14 MPa (2000 psi).

Data not available

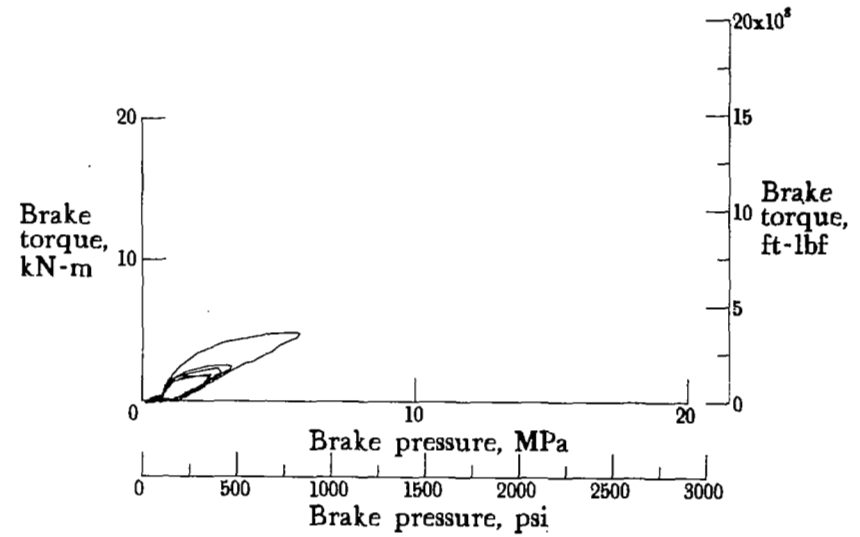
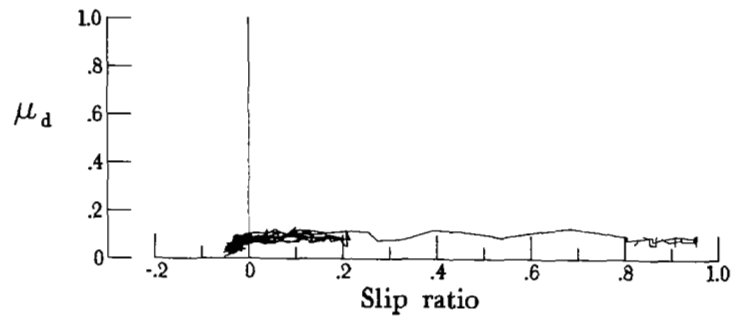


Figure A12.- Antiskid system dynamic response: system A; nominal carriage speed, 75 knots; vertical load, 78.1 kN (17 700 lbf); yaw angle, 0°; surface condition, flooded; tire condition, worn; brake pressure, 14 MPa (2000 psi).

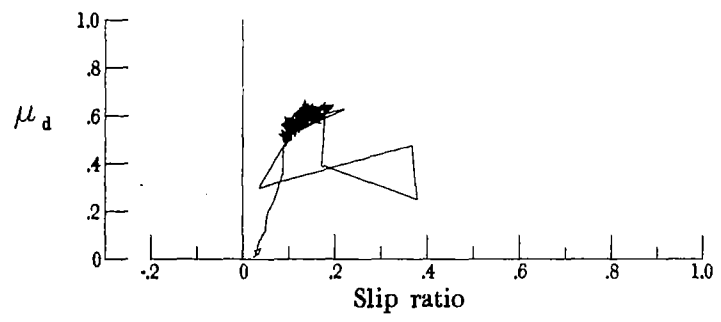
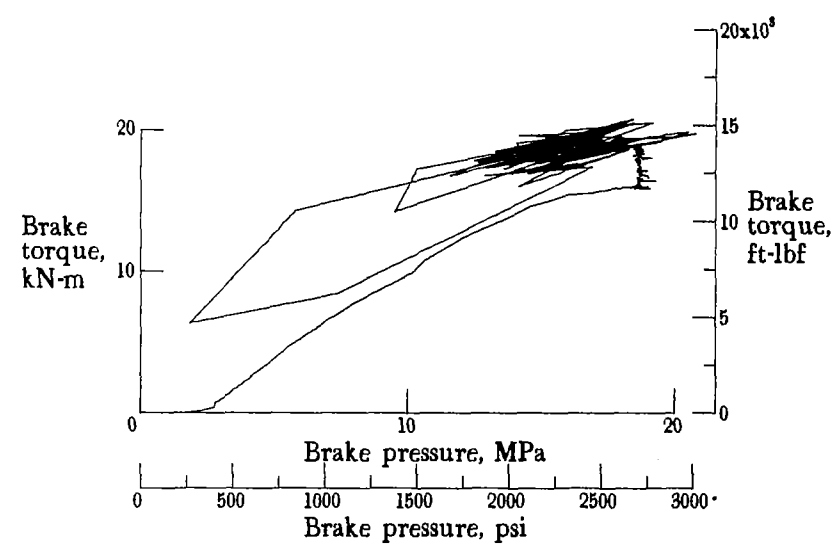
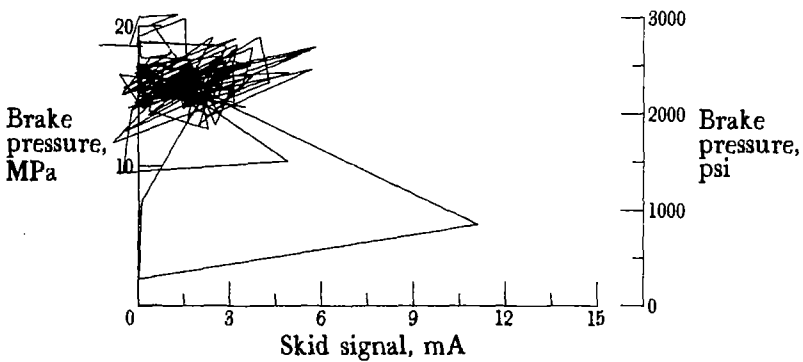


Figure A13.- Antiskid system dynamic response: system B; nominal carriage speed, 97 knots; vertical load, 63.6 kN (14 300 lbf); yaw angle, 0°; surface condition, one damp spot on an otherwise dry runway; tire condition, new; brake pressure, 19 MPa (2700 psi).

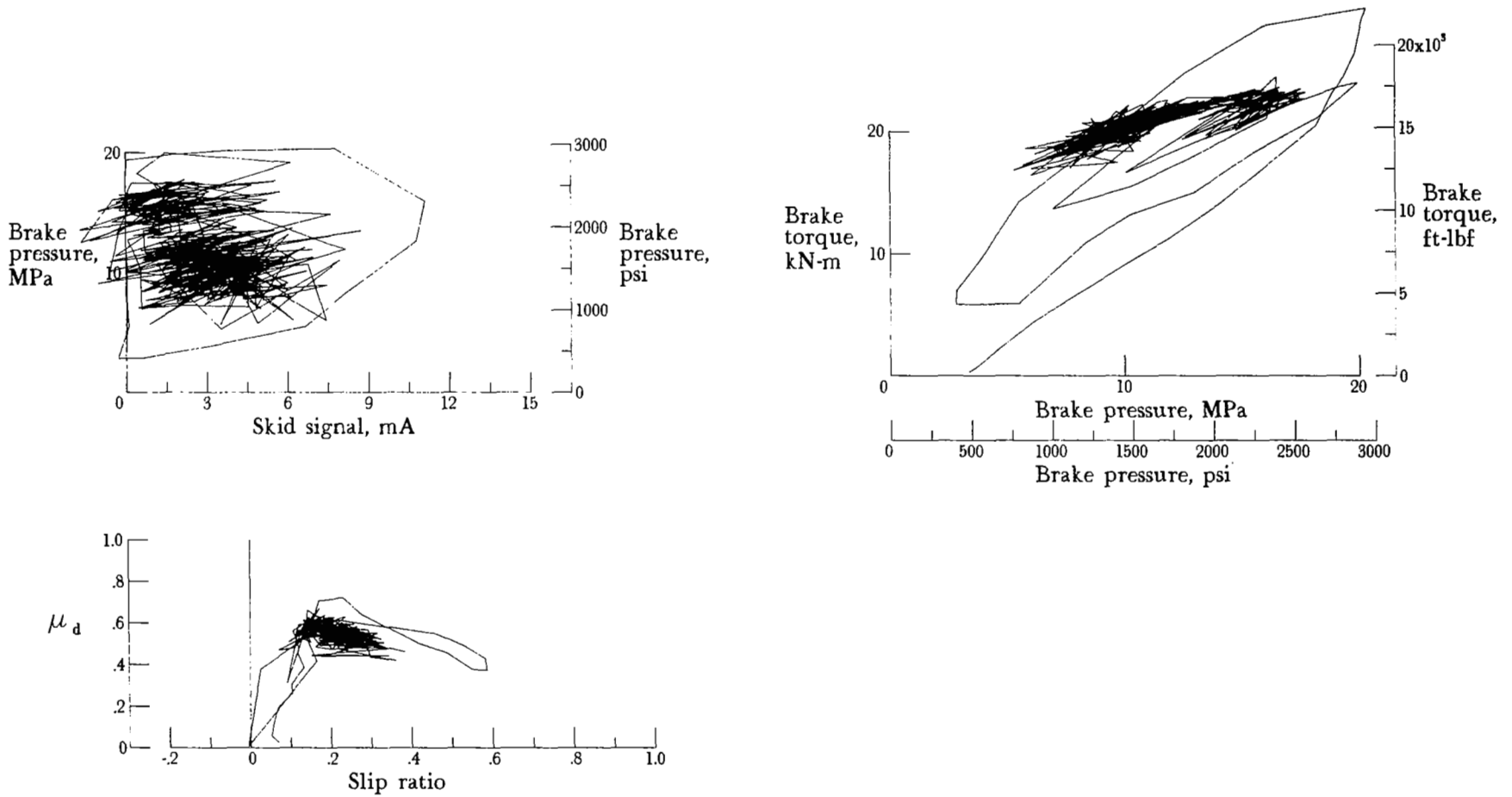


Figure A14.- Antiskid system dynamic response: system B; nominal carriage speed, 44 knots; vertical load, 81.8 kN (18 400 lbf); yaw angle, 0°; surface condition, dry; tire condition, new; brake pressure, 21 MPa (3000 psi).

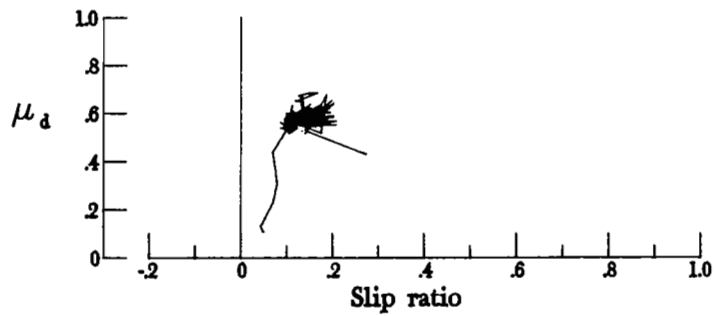
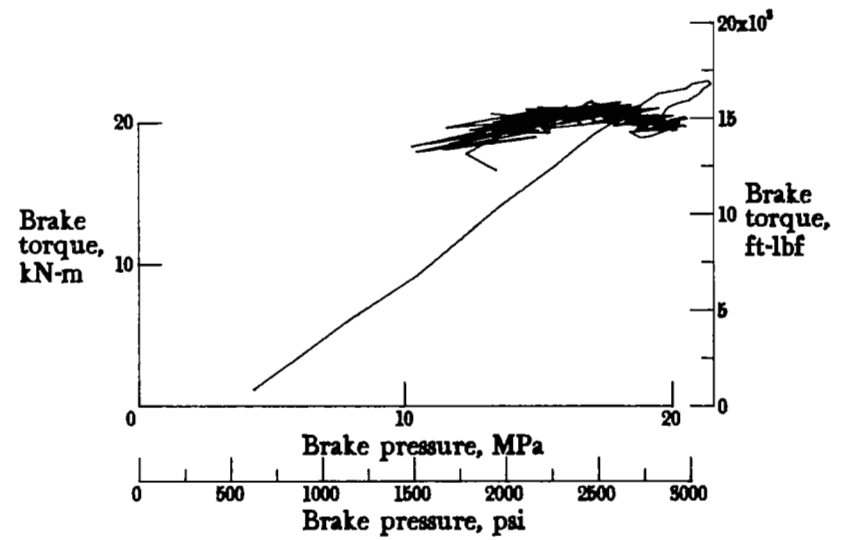
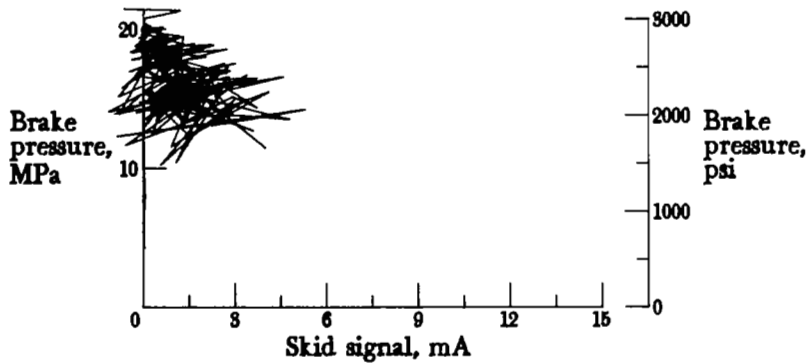


Figure A15.- Antiskid system dynamic response: system B; nominal carriage speed 68 knots; vertical load, 80.1 kN (18 000 lbf); yaw angle, 0°; surface condition, dry; tire condition, new; brake pressure, 21 MPa (3000 psi).

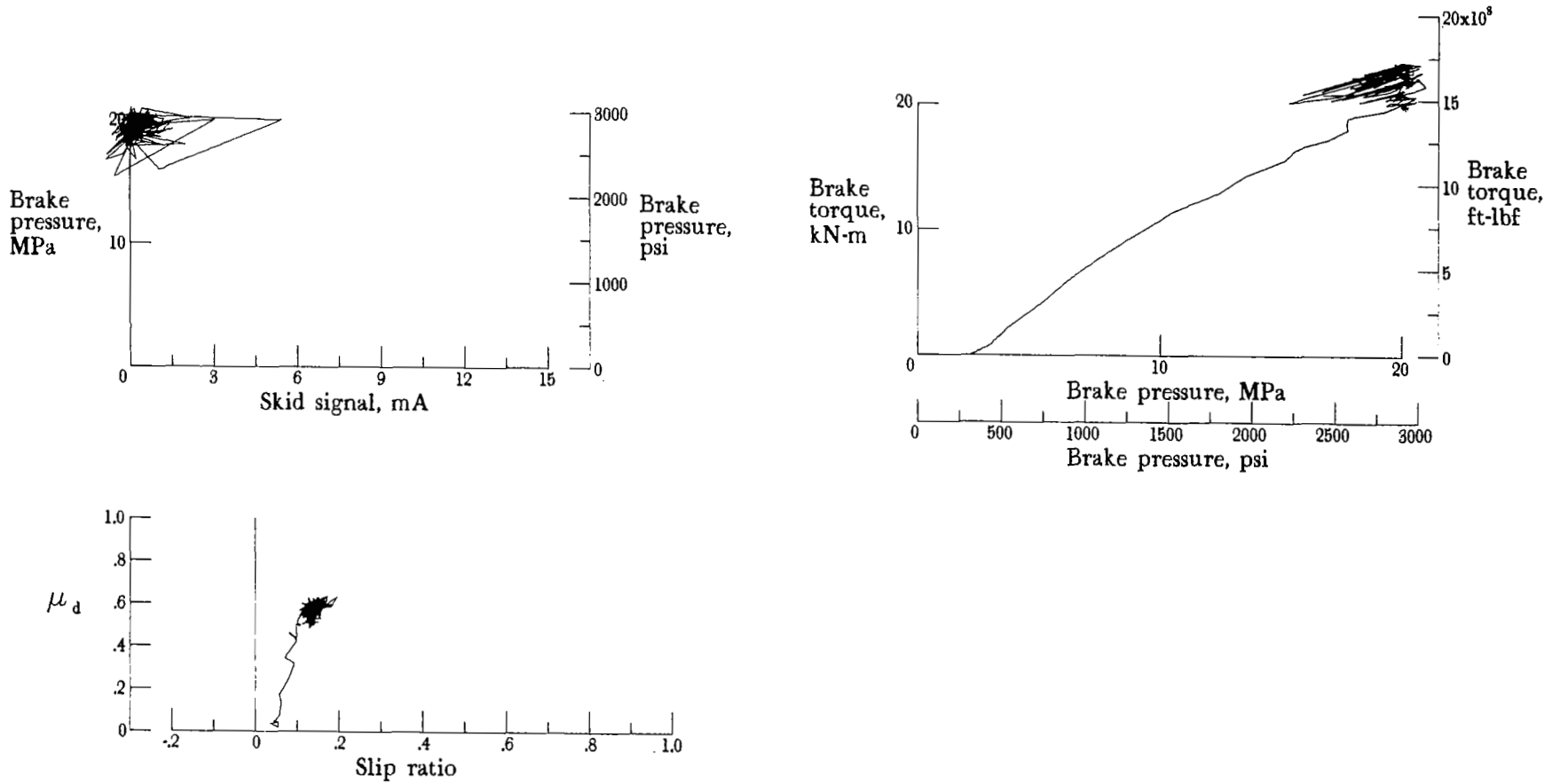


Figure A16.- Antiskid system dynamic response: system B; nominal carriage speed, 95 knots; vertical load, 81.8 kN (18 400 lbf); yaw angle, 0°; surface condition, dry; tire condition, new; brake pressure, 20 MPa (2890 psi).

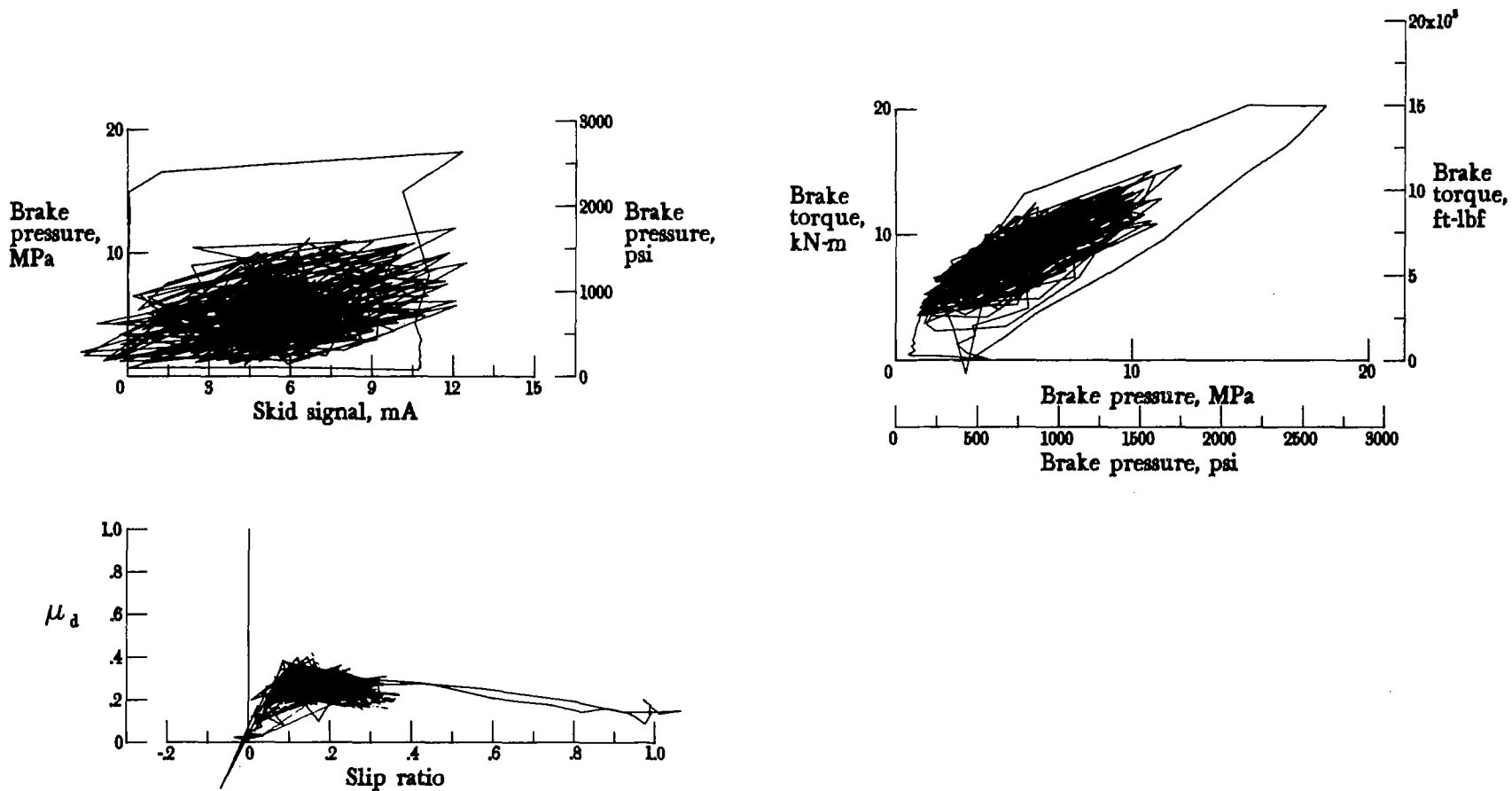


Figure A17.- Antiskid system dynamic response: system B; nominal carriage speed, 47 knots; vertical load, 62.3 kN (14 000 lbf); yaw angle, 0°; surface condition, damp; tire condition, new; brake pressure, 21 MPa (3000 psi).

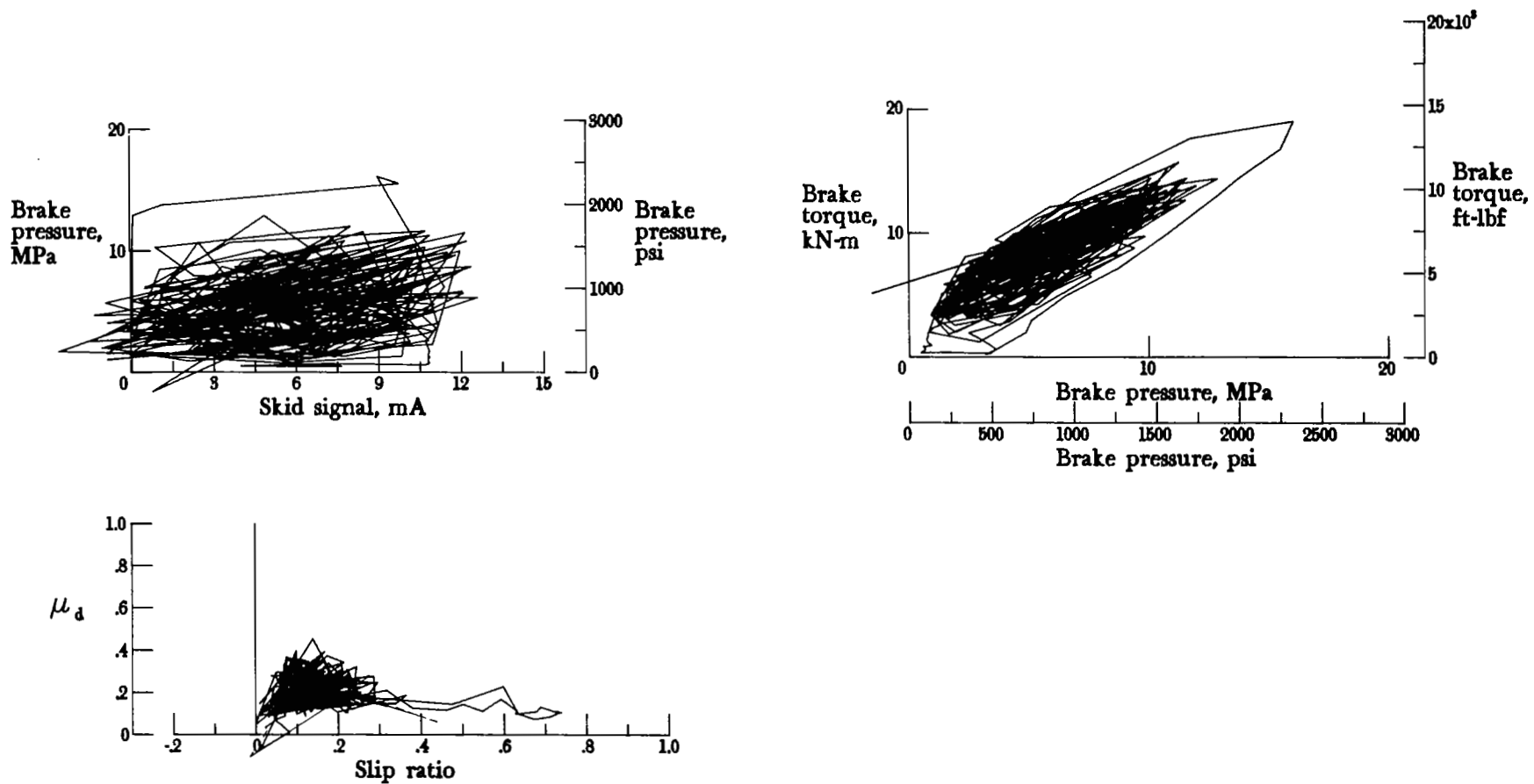


Figure A18.- Antiskid system dynamic response: system B; nominal carriage speed, 71 knots; vertical load, 63.2 kN (14 200 lbf); yaw angle, 0°; surface condition, damp; tire condition, new; brake pressure, 21 MPa (3000 psi).

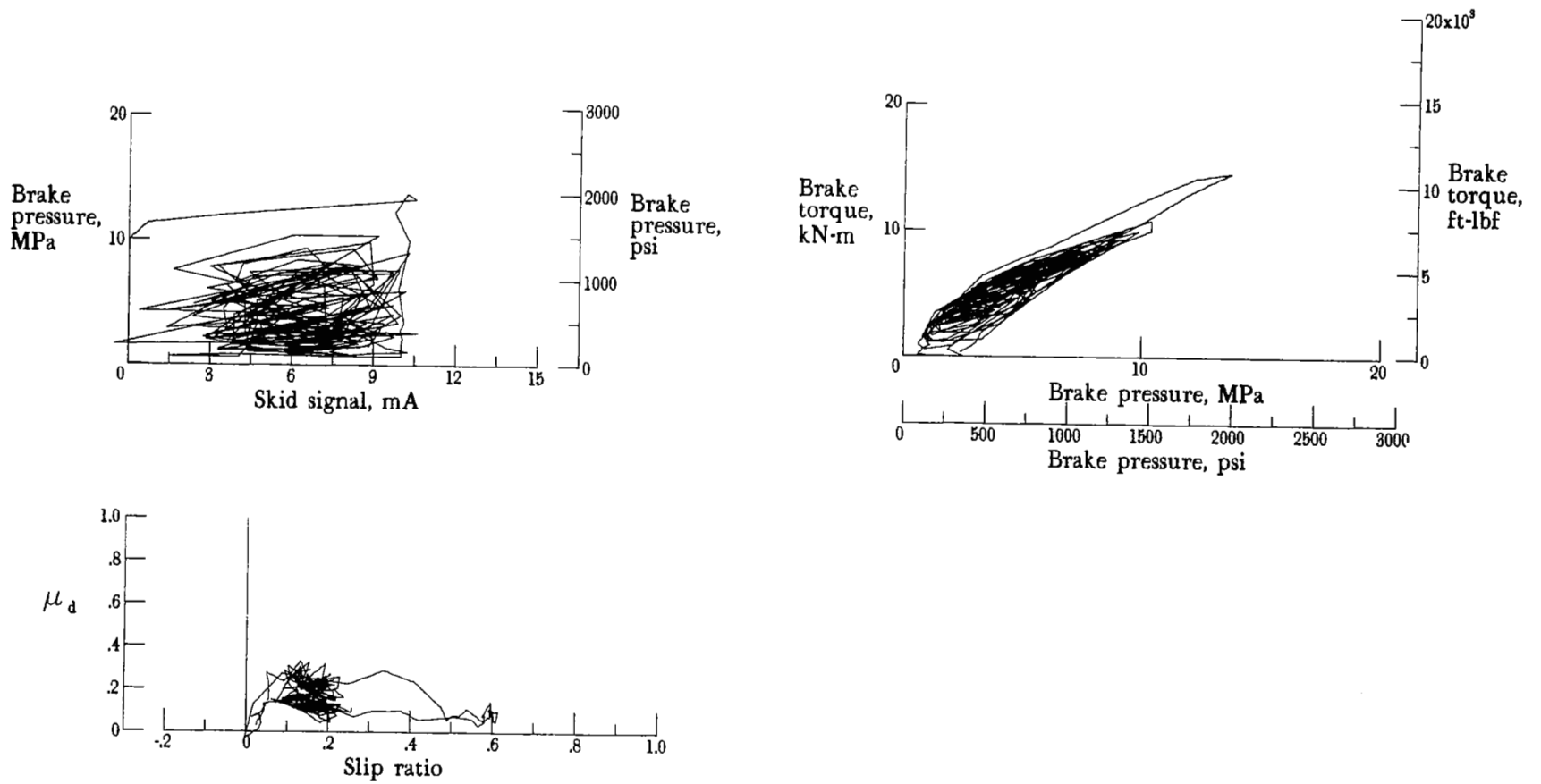


Figure A19.- Antiskid system dynamic response: system B; nominal carriage speed, 103 knots; vertical load, 61.8 kN (13 900 lbf); yaw angle, 0°; surface condition, damp; tire condition, new; brake pressure, 21 MPa (3000 psi).

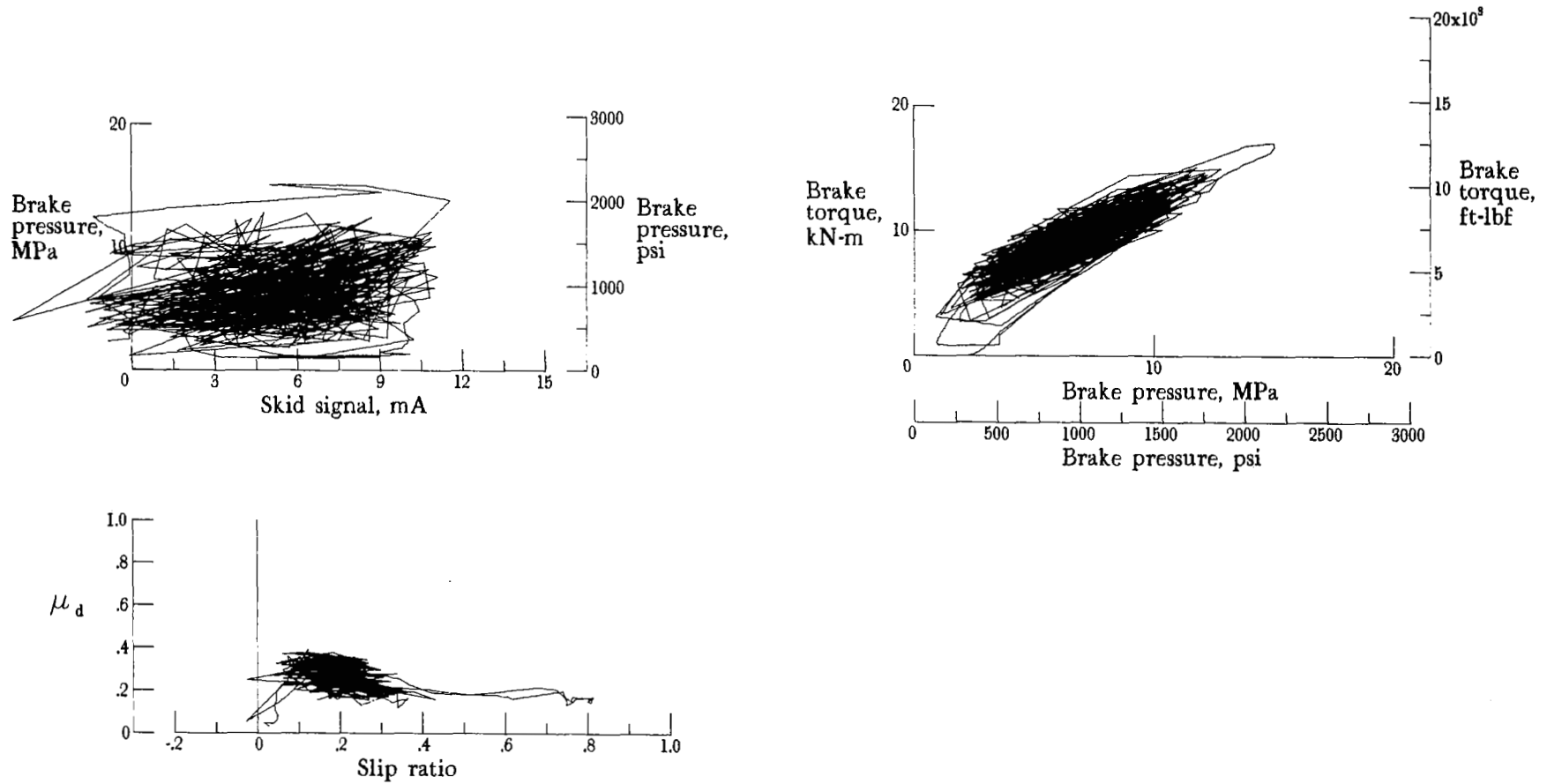
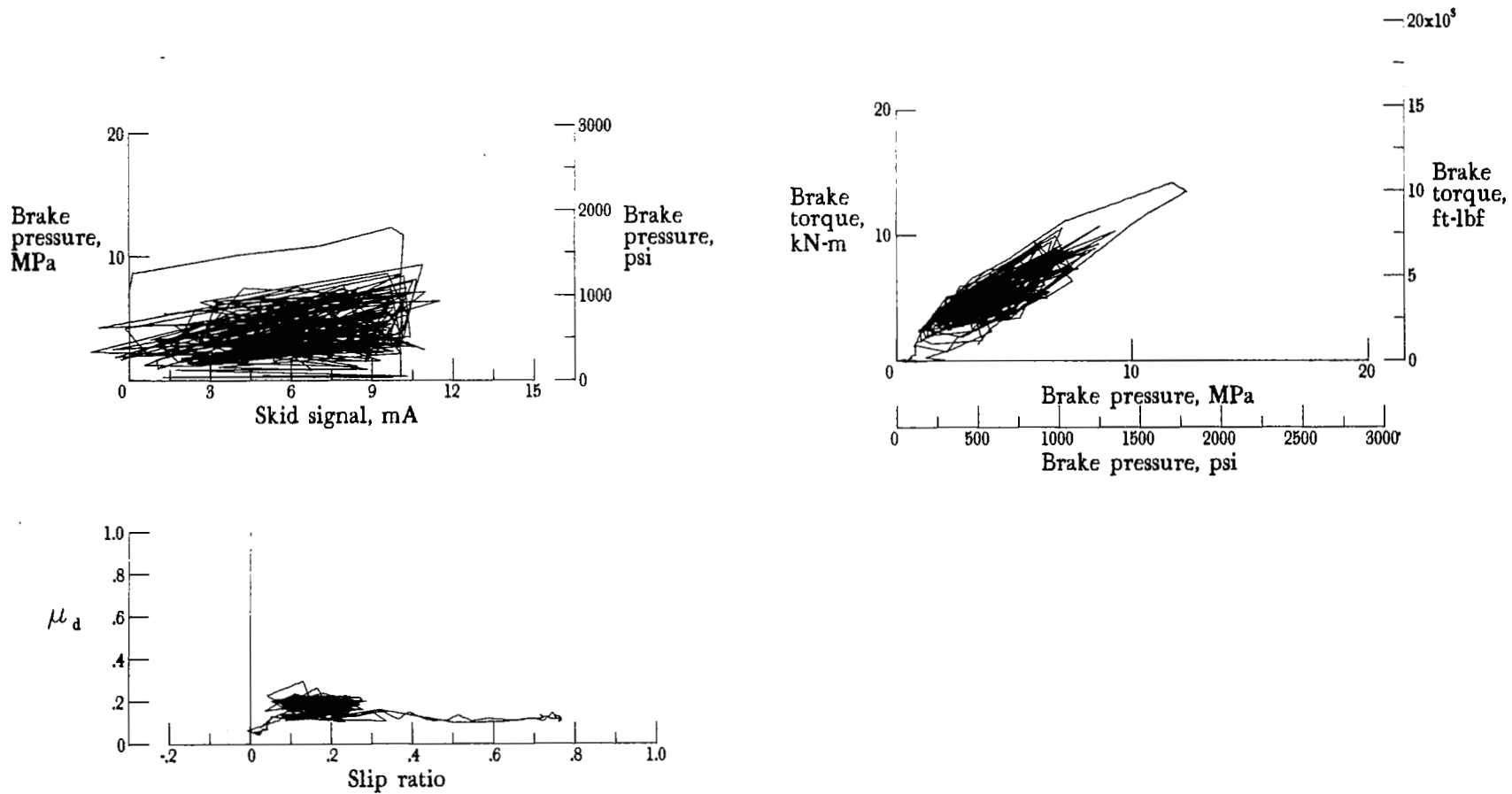


Figure A20.- Antiskid system dynamic response: system B; nominal carriage speed, 50 knots; vertical load, 81.4 kN (18 300 lbf); yaw angle, 0°; surface condition, flooded; tire condition, new; brake pressure, 21 MPa (3000 psi).



APPENDIX A

Figure A21.- Antiskid system dynamic response: system B; nominal carriage speed, 74 knots; vertical load, 81.0 kN (18 200 lbf); yaw angle, 0°; surface condition, flooded; tire condition, new; brake pressure, 21 MPa (3000 psi).

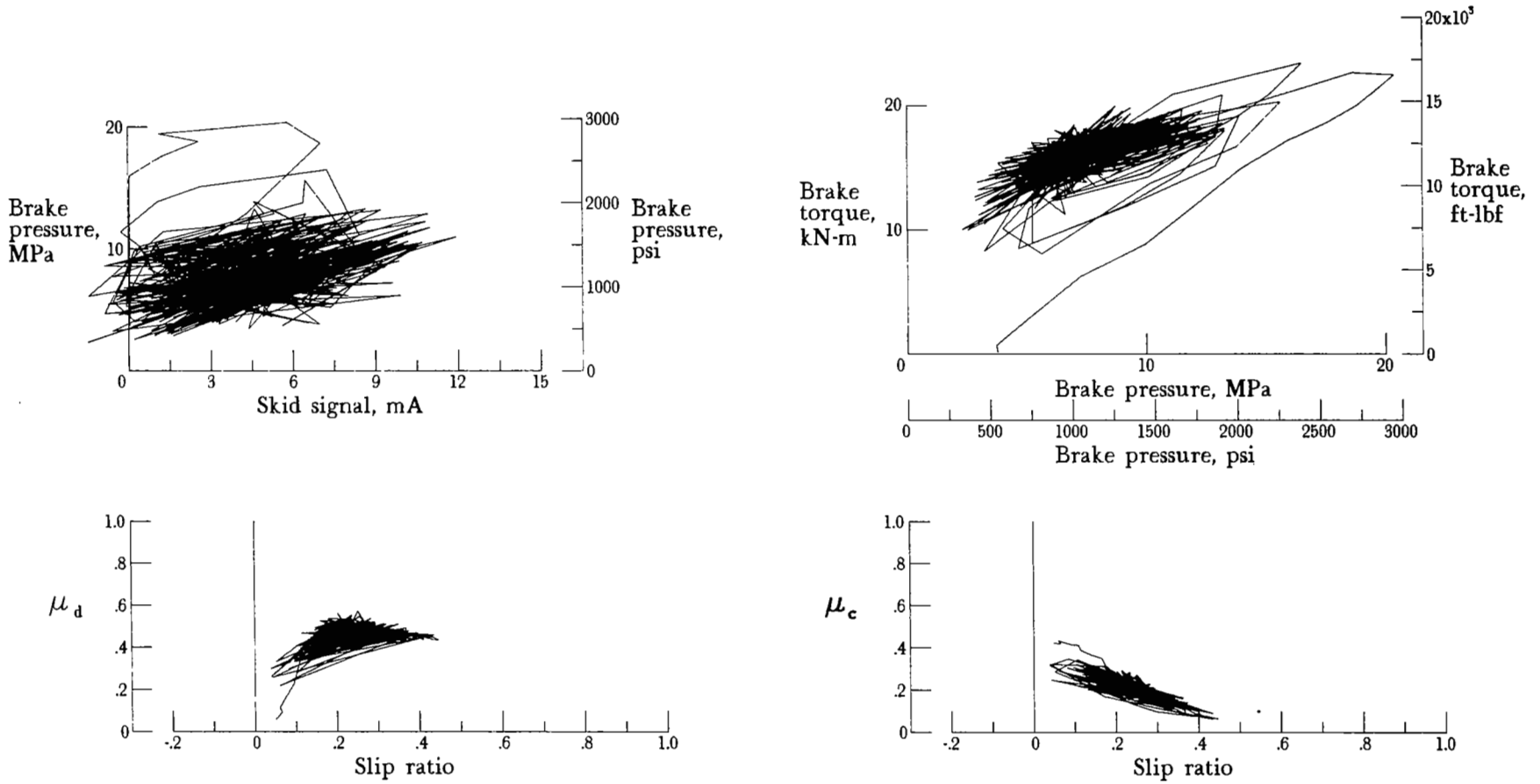


Figure A22.- Antiskid system dynamic response: system B; nominal carriage speed, 40 knots; vertical load, 81.4 kN (18 300 lbf); yaw angle, 6°; surface condition, dry; tire condition, new; brake pressure, 21 MPa (3000 psi).

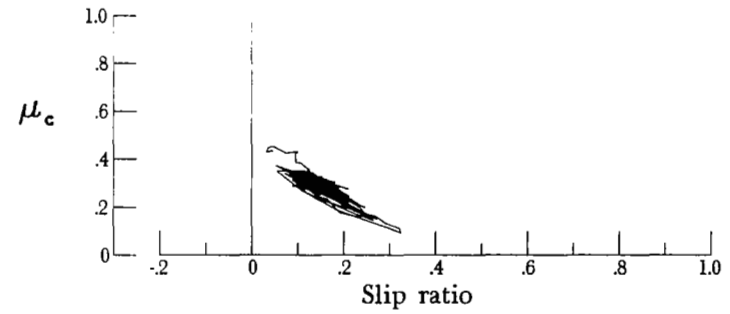
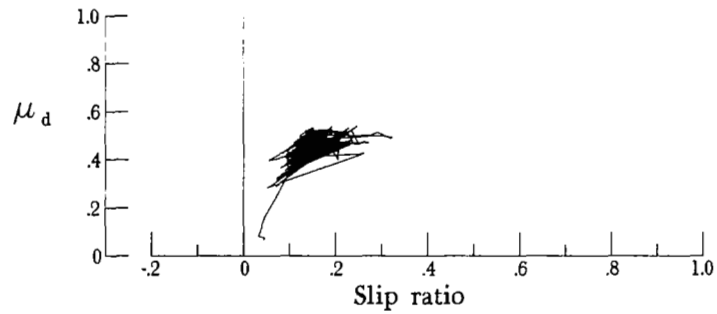
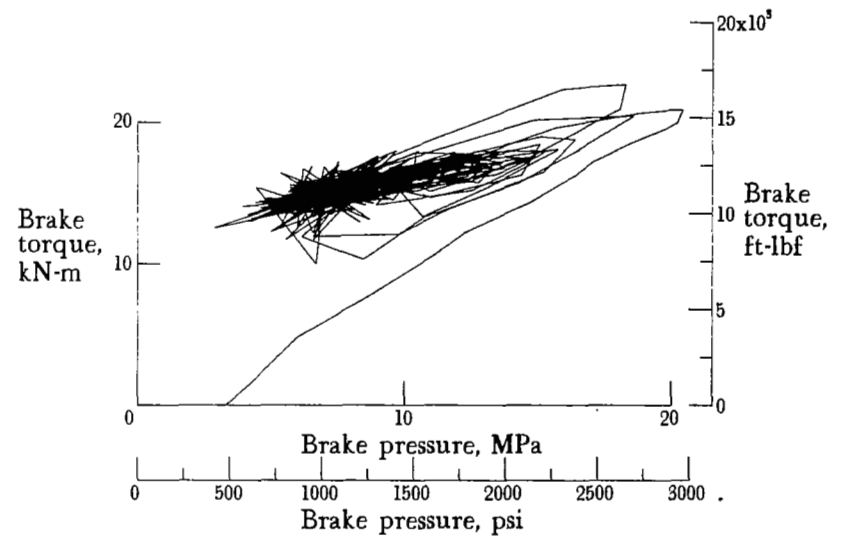
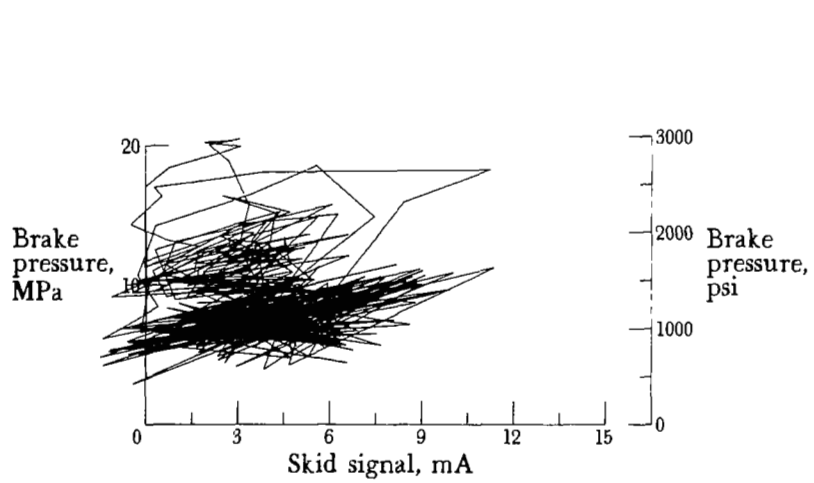


Figure A23.- Antiskid system dynamic response: system B; nominal carriage speed, 67 knots; vertical load, 81.4 kN (18 300 lbf); yaw angle, 6°; surface condition, dry; tire condition, new; brake pressure, 21 MPa (3000 psi).

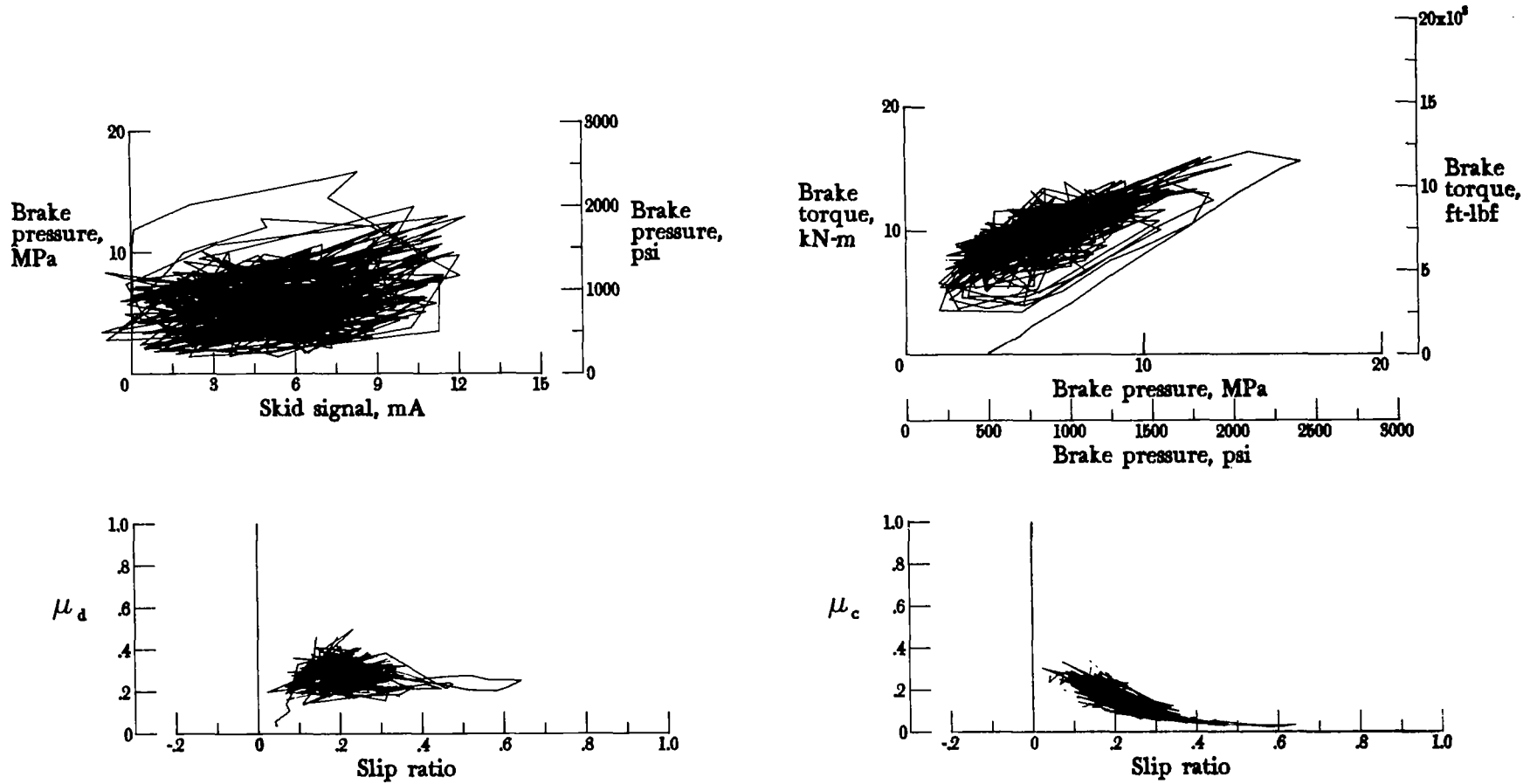


Figure A24.- Antiskid system dynamic response: system B; nominal carriage speed, 44 knots; vertical load, 81.0 kN (18 200 lbf); yaw angle, 6°; surface condition, damp; tire condition, new; brake pressure, 21 MPa (3000 psi).

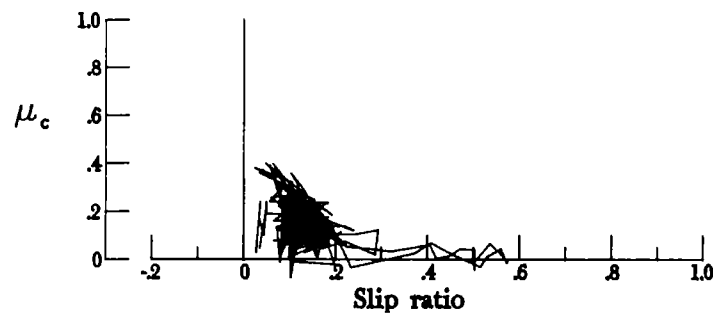
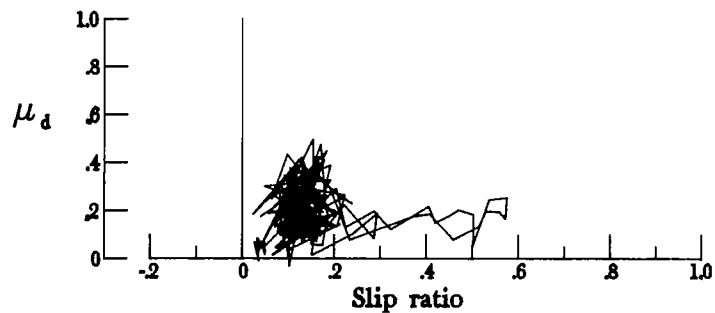
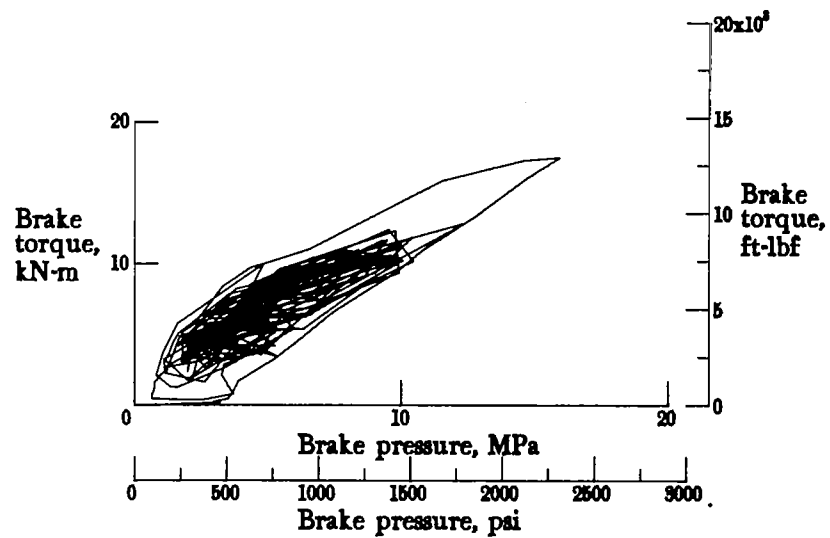
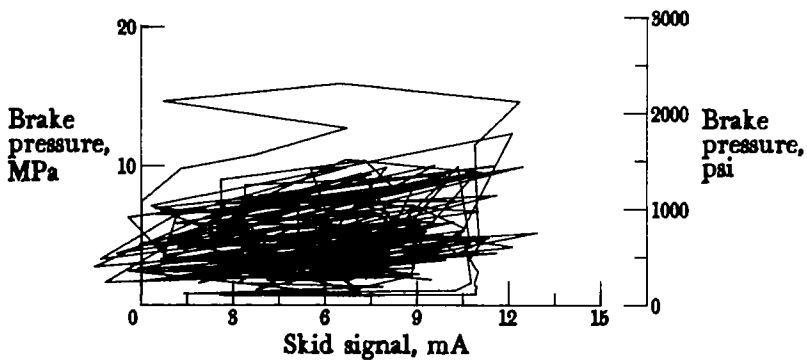


Figure A25.- Antiskid system dynamic response: system B; nominal carriage speed, 98 knots; vertical load, 81.0 kN (18 200 lbf); yaw angle, 6°; surface condition, damp; tire condition, new; brake pressure, 21 MPa (3000 psi).

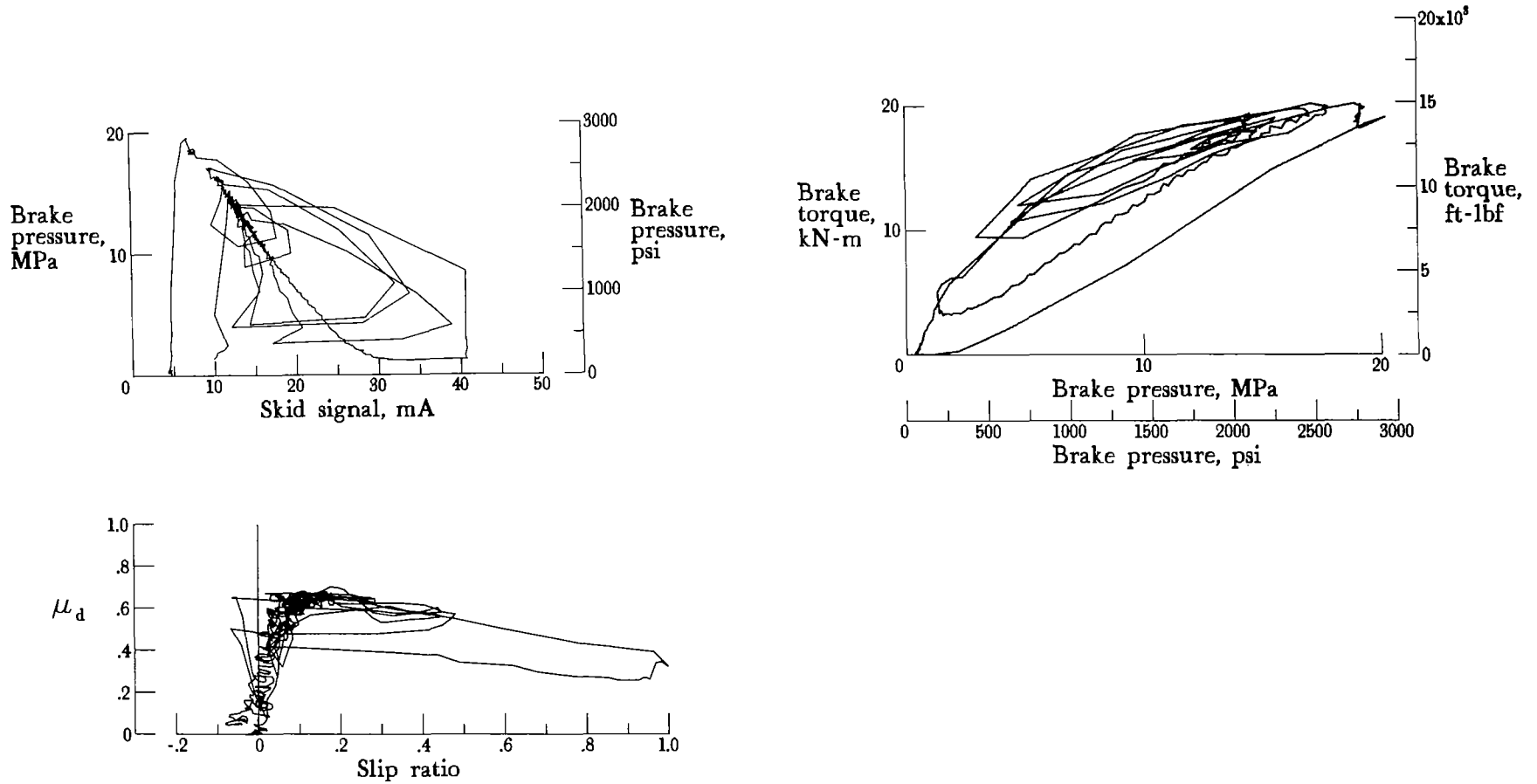


Figure A26.- Antiskid system dynamic response: system C; nominal carriage speed, 54 knots; vertical load, 59.6 kN (13 400 lbf); yaw angle, 0°; surface condition, one damp spot on an otherwise dry runway; tire condition, new; brake pressure, 21 MPa (3000 psi).

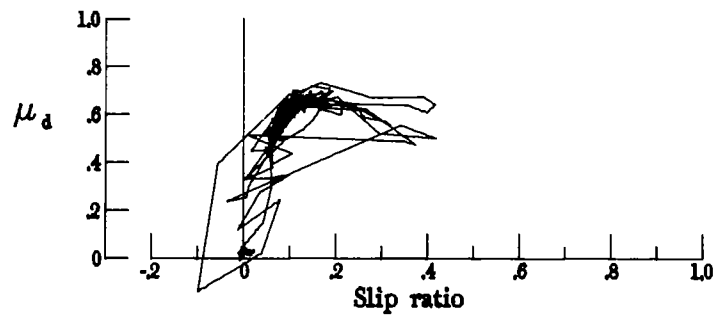
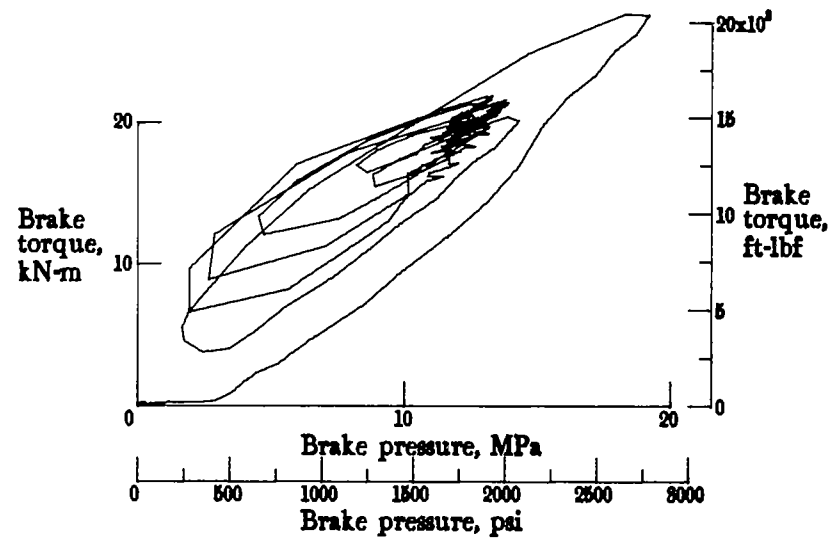
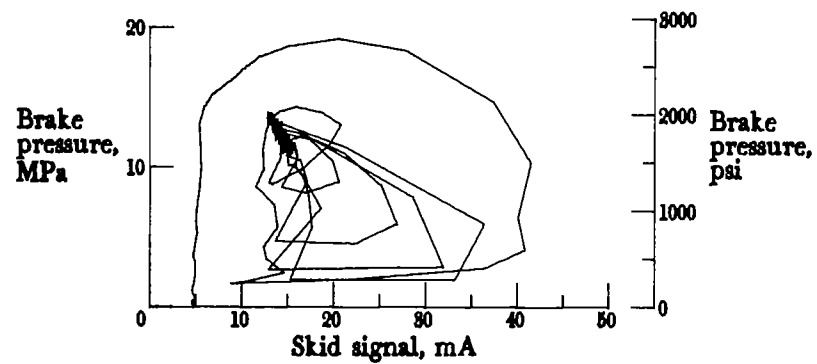


Figure A27.- Antiskid system dynamic response: system C; nominal carriage speed, 70 knots; vertical load, 64.9 kN (14 600 lbf); yaw angle, 0°; surface condition, dry; tire condition, new; brake pressure, 21 MPa (3000 psi).

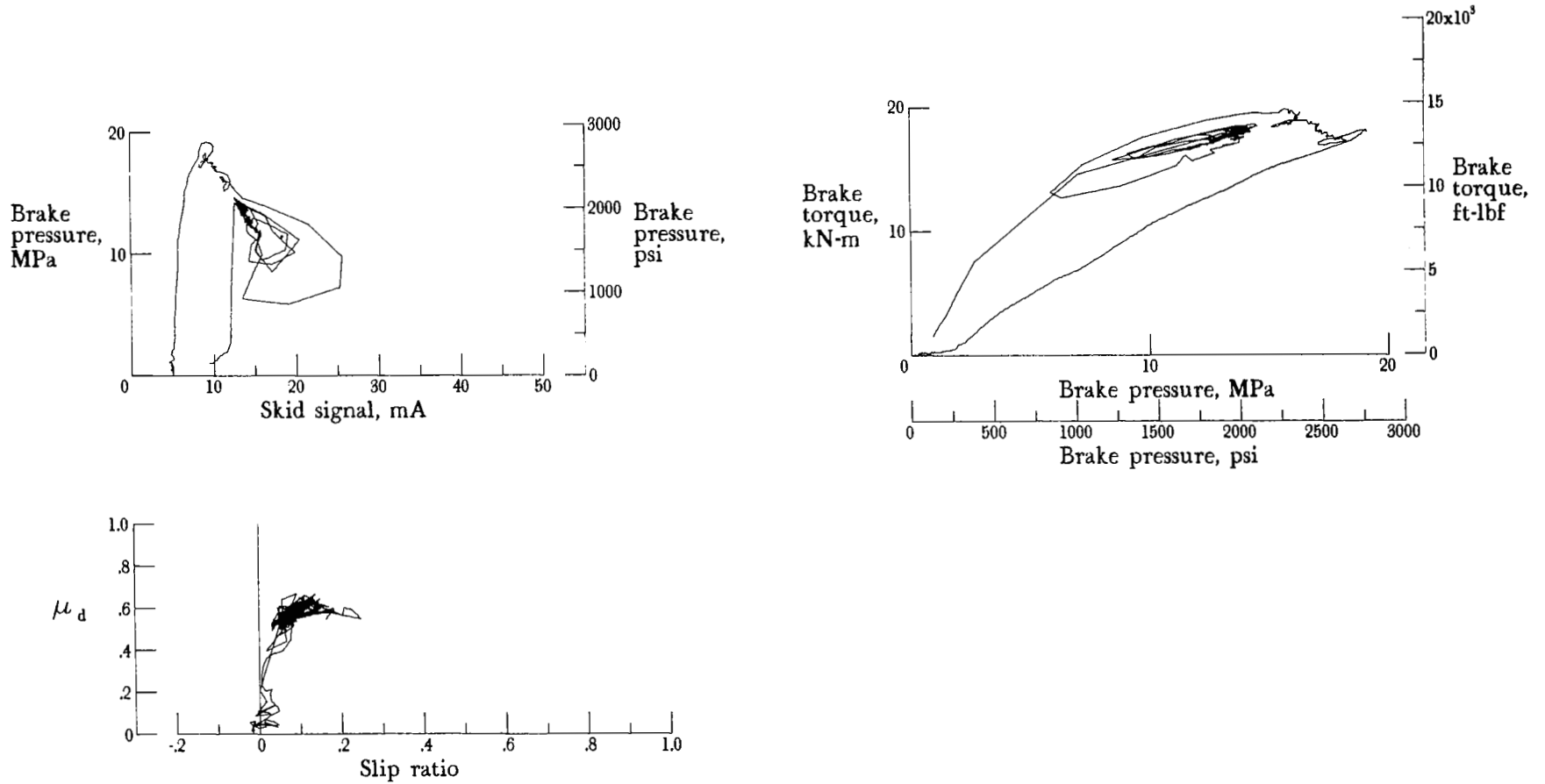


Figure A28.- Antiskid system dynamic response: system C; nominal carriage speed, 99 knots; vertical load, 61.8 kN (13 900 lbf); yaw angle, 0°; surface condition, dry; tire condition, new; brake pressure, 21 MPa (3000 psi).

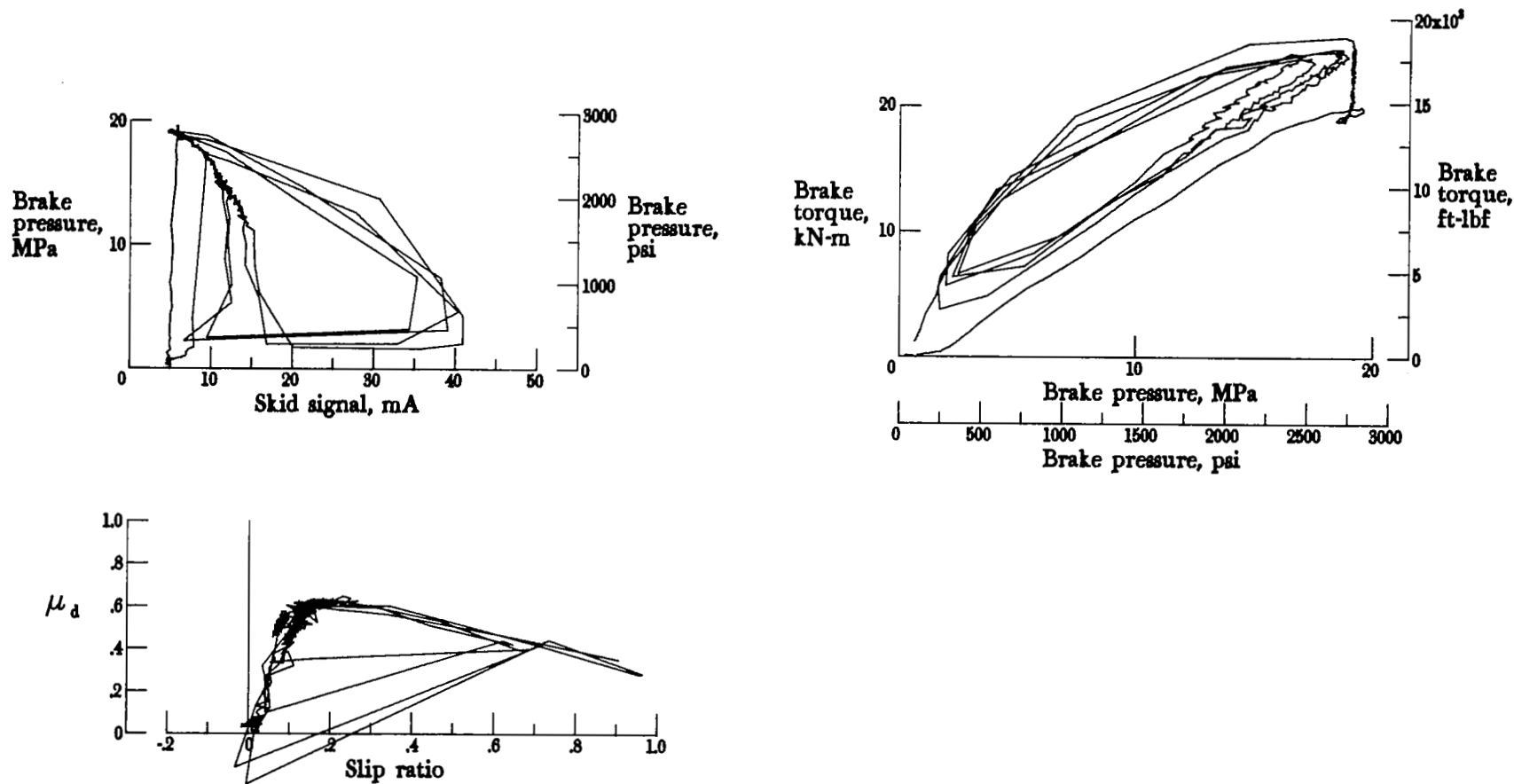


Figure A29.- Antiskid system dynamic response: system C; nominal carriage speed, 43 knots; vertical load, 83.6 kN (18 800 lbf); yaw angle, 0°; surface condition, dry; tire condition, new; brake pressure, 20 MPa (2900 psi).

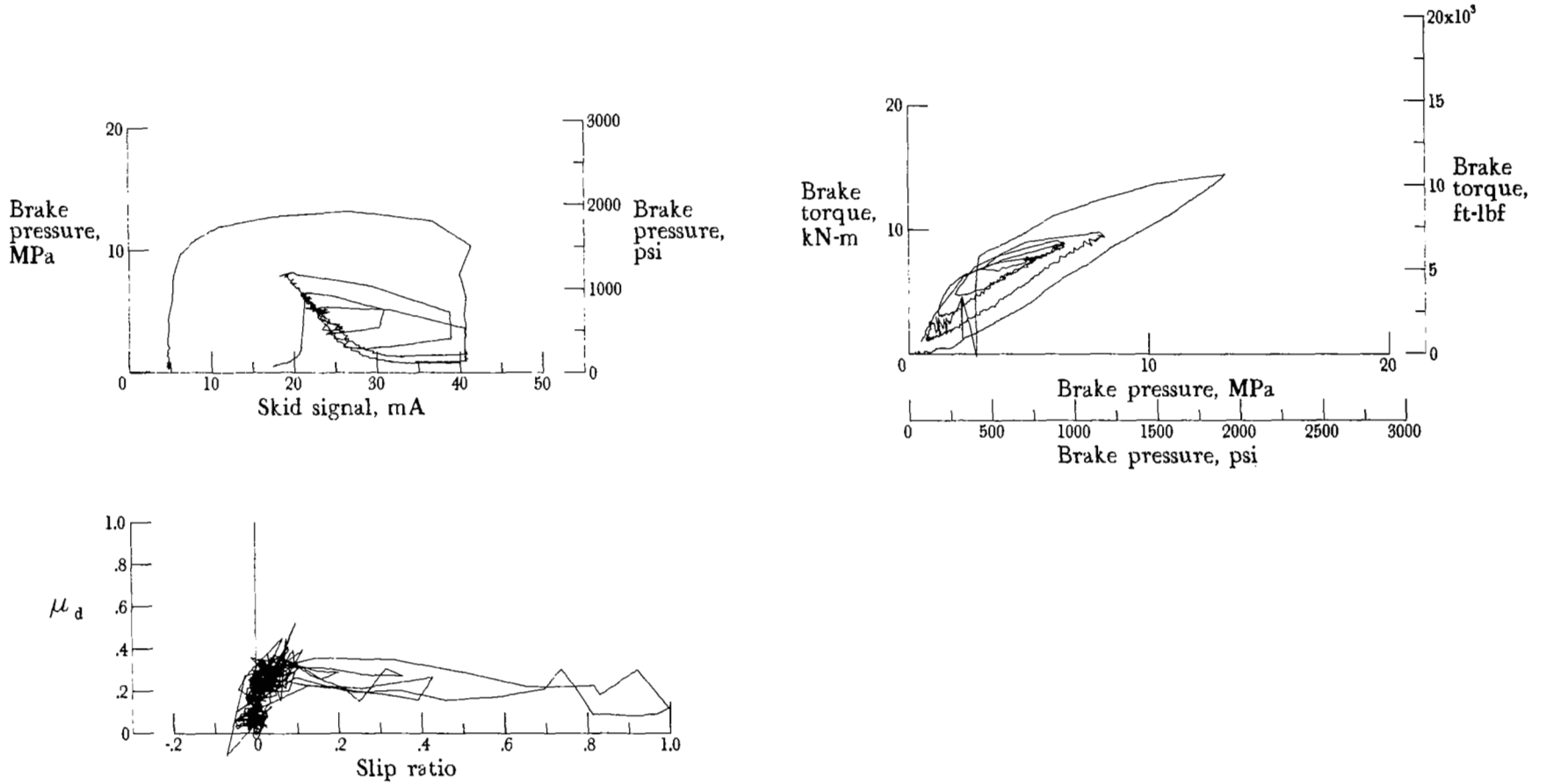


Figure A30.- Antiskid system dynamic response: system C; nominal carriage speed, 56 knots; vertical load, 59.6 kN (13 400 lbf); yaw angle, 0°; surface condition, damp; tire condition, new; brake pressure, 21 MPa (3000 psi).

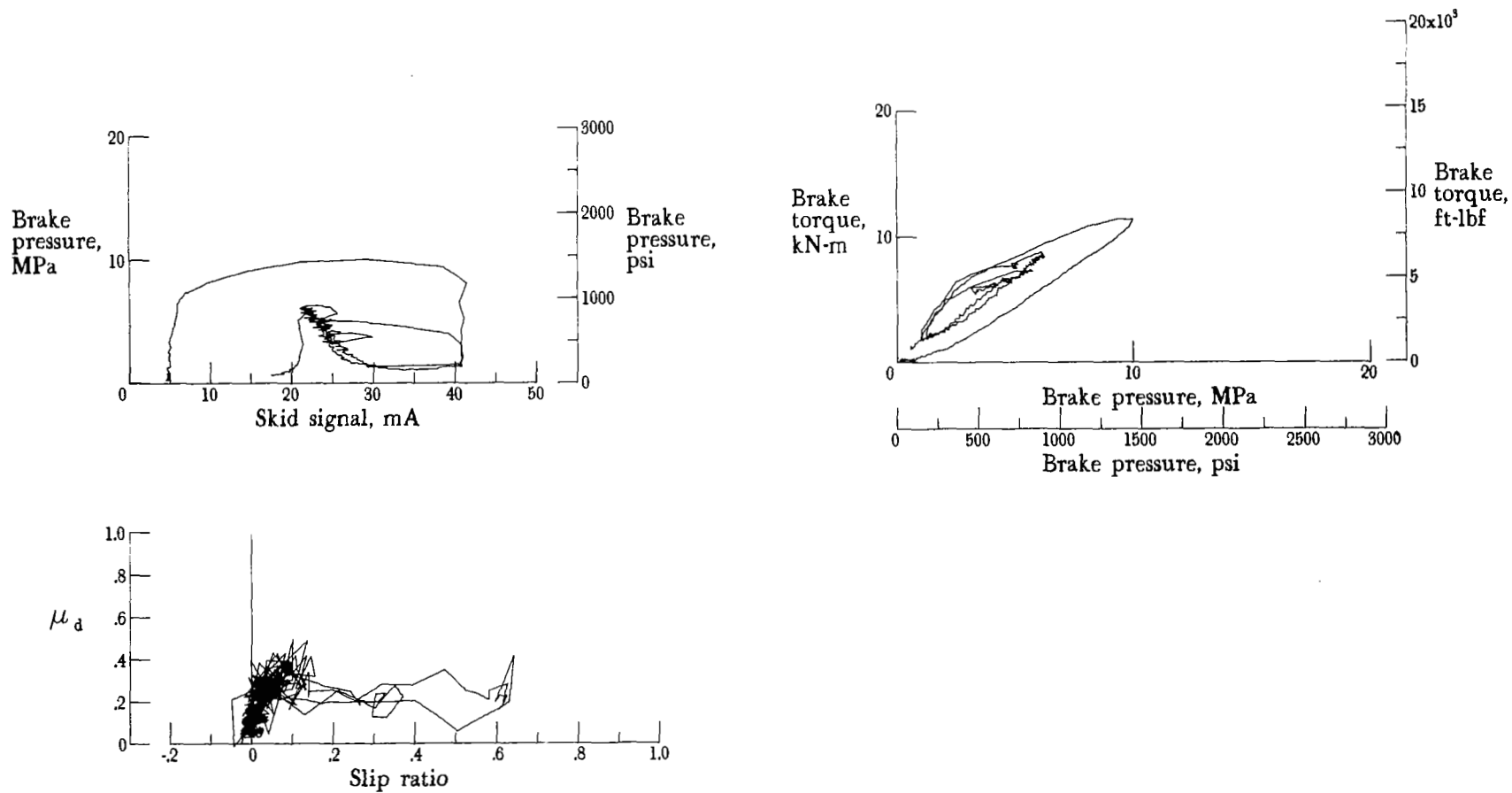


Figure A31.- Antiskid system dynamic response: system C; nominal carriage speed, 77 knots; vertical load, 59.6 kN (13 400 lbf); yaw angle, 0°; surface condition, damp; tire condition, new; brake pressure, 21 MPa (3000 psi).

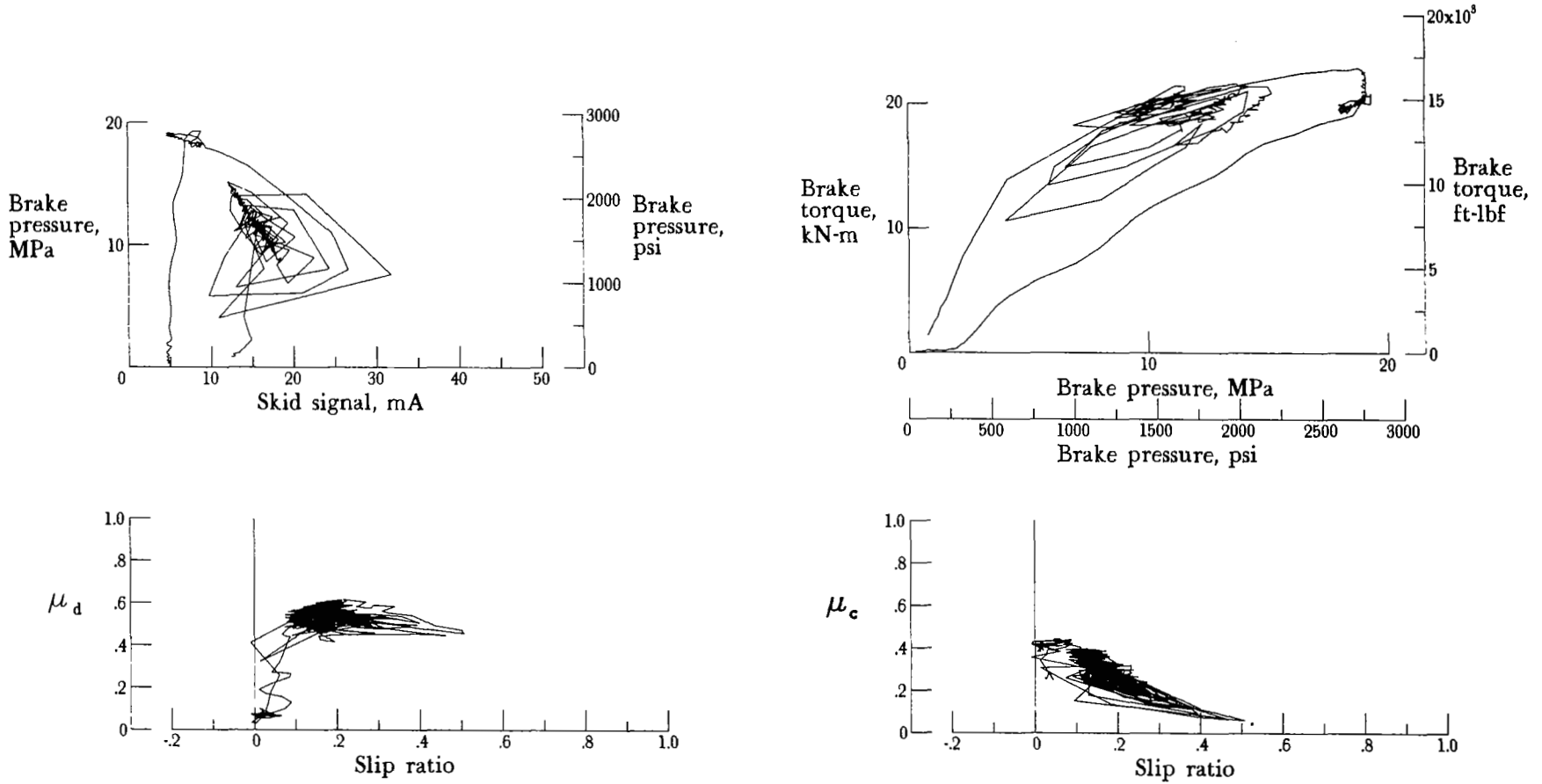


Figure A32.- Antiskid system dynamic response: system C; nominal carriage speed, 47 knots; vertical load, 85.0 kN (19 100 lbf); yaw angle, 6°; surface condition, dry; tire condition, new; brake pressure, 21 MPa (3000 psi).

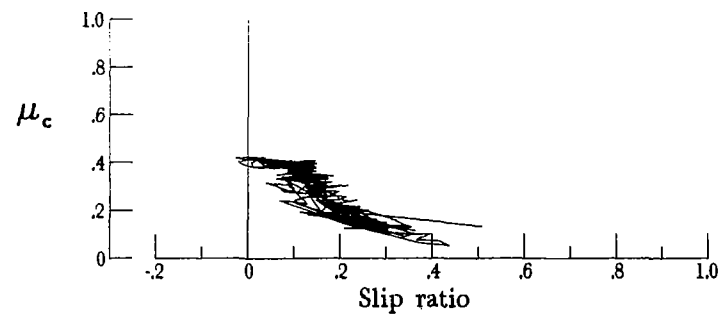
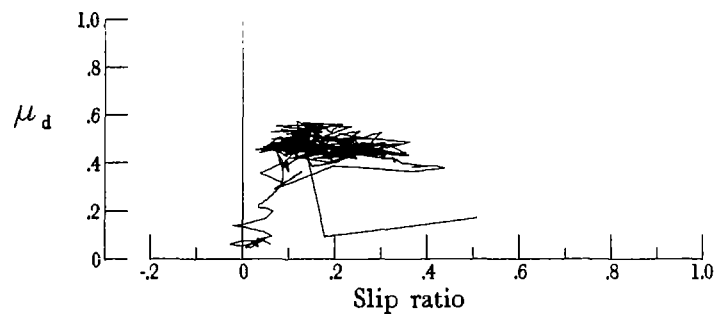
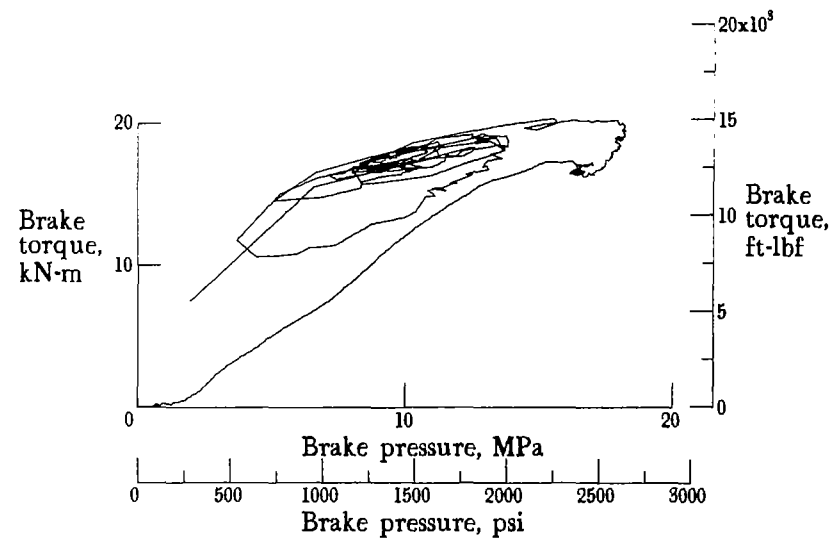
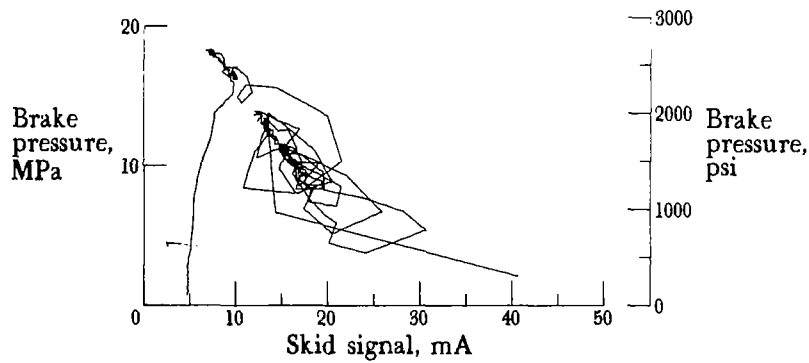


Figure A33.- Antiskid system dynamic response: system C; nominal carriage speed, 75 knots; vertical load, 85.0 kN (19 100 lbf); yaw angle, 6°; surface condition, dry; tire condition, new; brake pressure, 20 MPa (2900 psi).

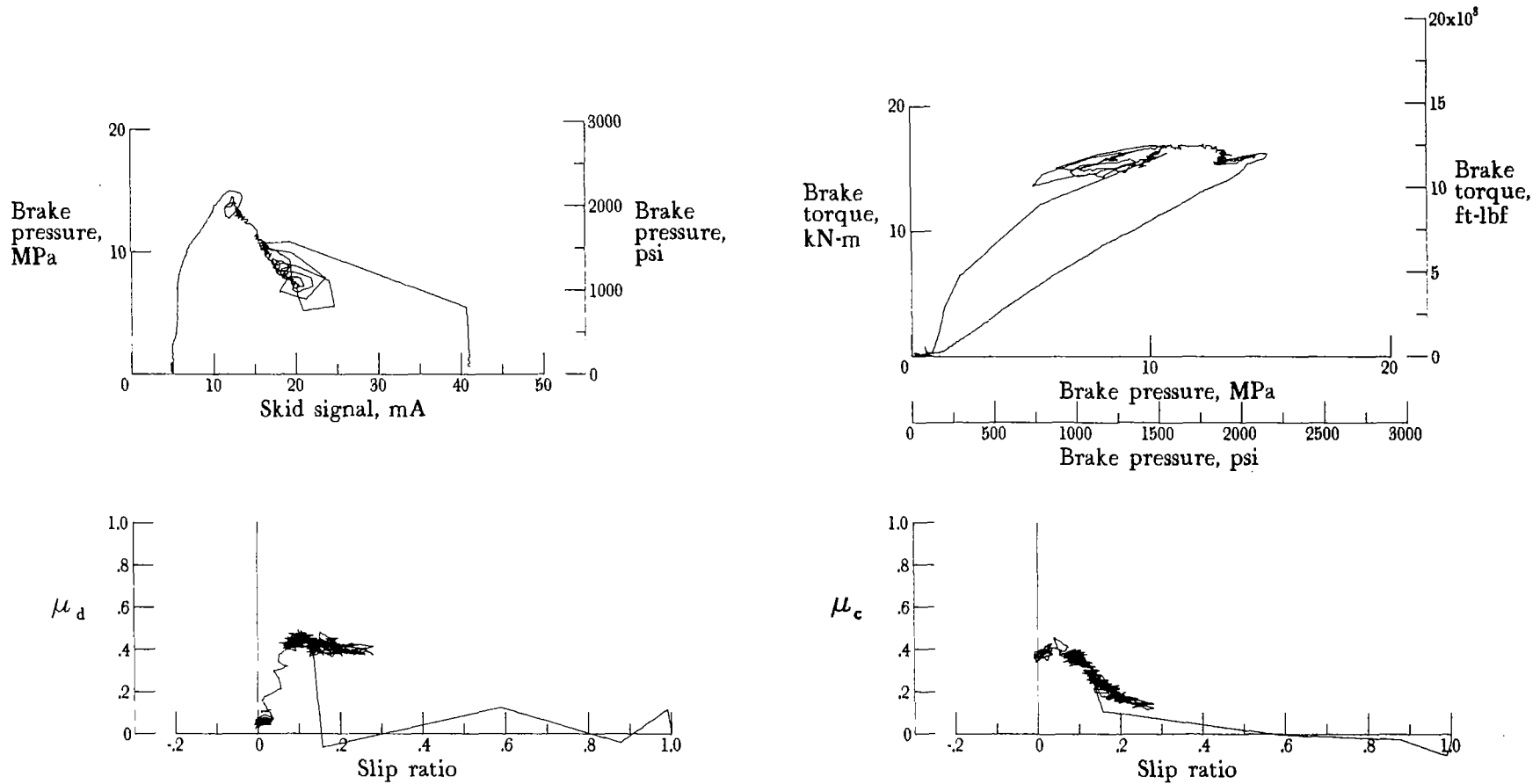


Figure A34.- Antiskid system dynamic response: system C; nominal carriage speed, 103 knots; vertical load, 85.0 kN (19 100 lbf); yaw angle, 6°; surface condition, dry; tire condition, new; brake pressure, 21 MPa (3000 psi).

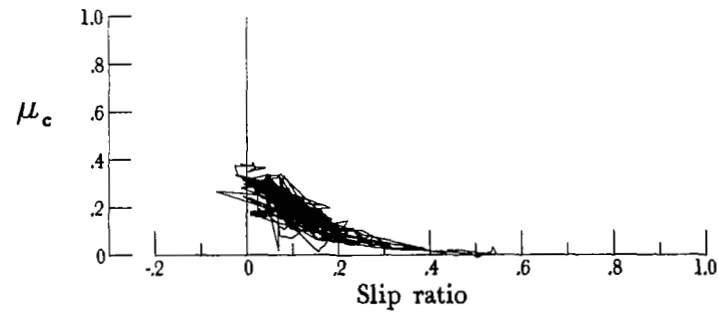
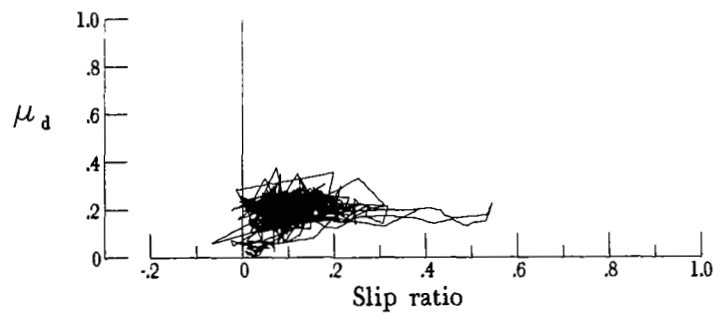
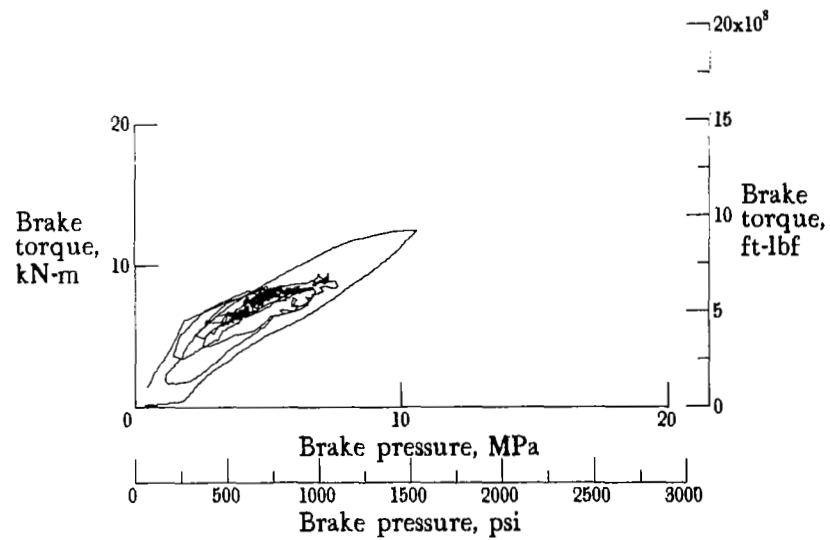
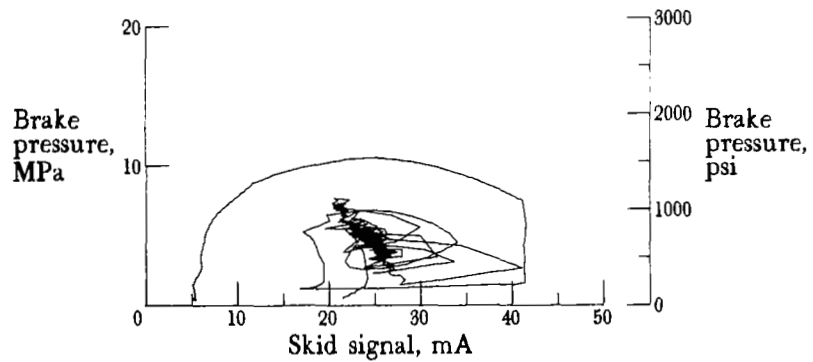


Figure A35.- Antiskid system dynamic response: system C; nominal carriage speed, 57 knots; vertical load, 85.9 kN (19 300 lbf); yaw angle, 6°; surface condition, damp; tire condition, new; brake pressure, 21 MPa (3000 psi).

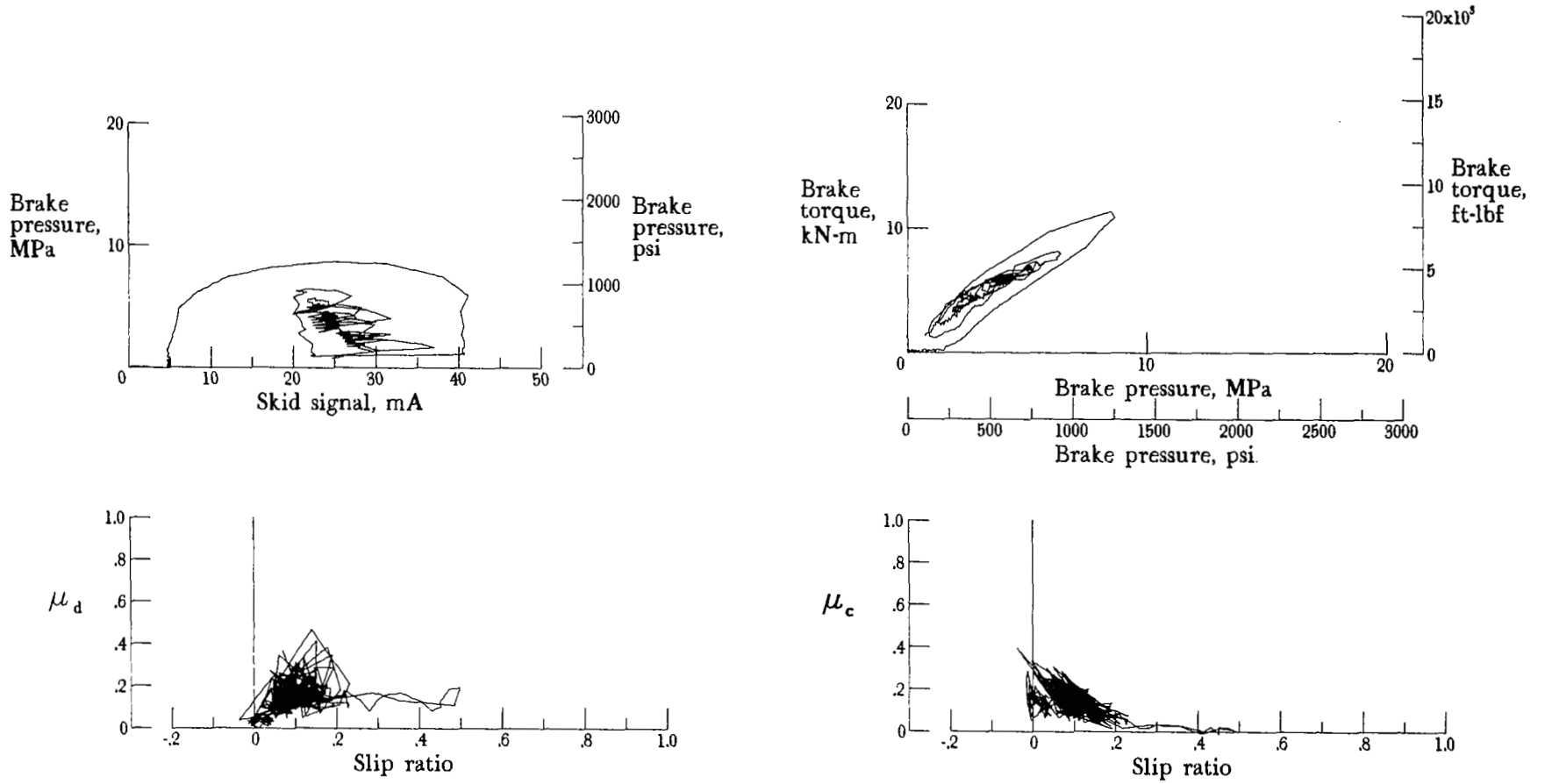


Figure A36.- Antiskid system dynamic response: system C; nominal carriage speed, 77 knots; vertical load, 84.1 kN (18 900 lbf); yaw angle, 6°; surface condition, damp; tire condition, new; brake pressure, 20 MPa (2900 psi).

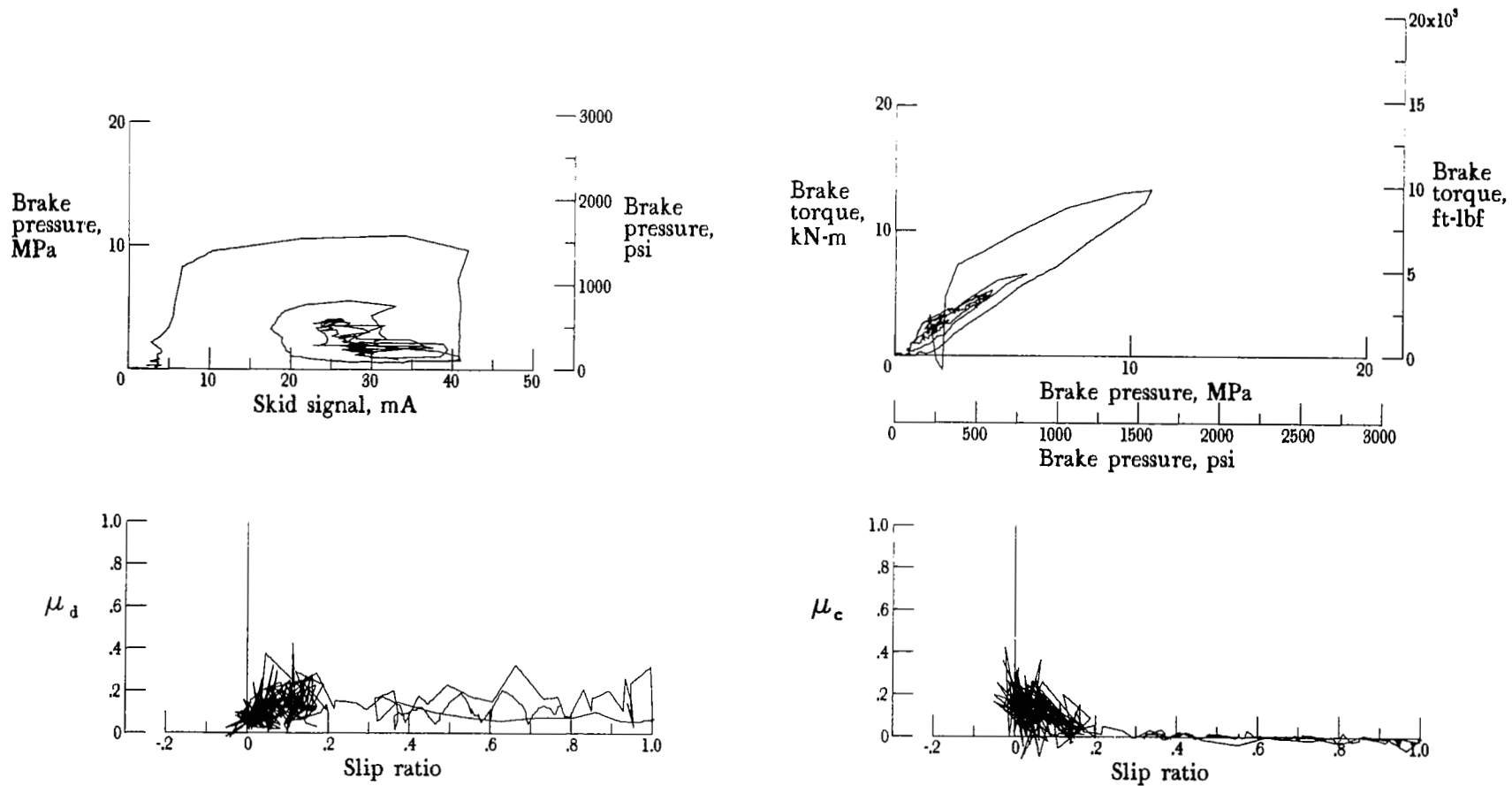


Figure A37.- Antiskid system dynamic response: system C; nominal carriage speed, 106 knots; vertical load, 77.8 kN (17 500 lbf); yaw angle, 6°; surface condition, damp; tire condition, new; brake pressure, 20 MPa (2900 psi).

APPENDIX B

COMPUTER CODES

This appendix presents the advanced continuous simulation language (ACSL, pronounced "axle") computer codes used to simulate the brake pressure-torque response (ref. 16).

Experimental Data Input

The following lines of computer codes are used to input brake pressure and torque time histories for the computer simulation and are common to all three computer models. The input data in this example is from run A18.

PROGRAM DYNAMIC PRESSURE-TORQUE

"- - - - - DEFINE TABLES FOR TORQUE AND PRESSURE TIME HISTORIES"

TABLE	ACTTOR, 1, 123 ...
	/0.00, 0.008, 0.016, 0.024, 0.032, 0.040, 0.048, 0.056, 0.064, ...
	0.072, 0.080, 0.088, 0.096, 0.104, 0.112, 0.120, 0.128, 0.136, ...
	0.144, 0.152, 0.160, 0.168, 0.176, 0.184, 0.192, 0.200, 0.208, ...
	0.216, 0.224, 0.232, 0.240, 0.248, 0.256, 0.264, 0.272, 0.280, ...
	0.288, 0.296, 0.304, 0.312, 0.320, 0.328, 0.336, 0.344, 0.352, ...
	0.360, 0.368, 0.376, 0.384, 0.392, 0.400, 0.408, 0.416, 0.424, ...
	0.432, 0.440, 0.448, 0.456, 0.464, 0.472, 0.480, 0.488, 0.496, ...
	0.504, 0.512, 0.520, 0.528, 0.536, 0.544, 0.552, 0.560, 0.568, ...
	0.576, 0.584, 0.592, 0.600, 0.608, 0.616, 0.624, 0.632, 0.640, ...
	0.648, 0.656, 0.664, 0.672, 0.680, 0.688, 0.696, 0.704, 0.712, ...
	0.720, 0.728, 0.736, 0.744, 0.752, 0.760, 0.768, 0.776, 0.784, ...
	0.792, 0.800, 0.808, 0.816, 0.824, 0.832, 0.840, 0.848, 0.856, ...
	0.864, 0.872, 0.880, 0.888, 0.896, 0.904, 0.912, 0.920, 0.928, ...
	0.936, 0.944, 0.952, 0.960, 0.968, 0.976, ...
	0., 0., 0., 0., 0., 0., 0., 0., 0., 0., 0., 26., 145., 507., ...
	1599., 3108., 4650., 6512., 8792., 10907., 12696., 14352., ...
	12421., 9737., 6866., 4989., 3842., 3040., 2553., 2177., 1861., ...
	1617., 1397., 1044., 870., 714., 594., 645., 498., 379., 381., ...
	255., 200., 273., 347., 246., 315., 824., 1283., 1911., 2462., ...
	3269., 4319., 4953., 5494., 5586., 4430., 3966., 3338., 2810., ...
	2888., 2833., 4173., 5787., 6682., 7659., 6237., 4861., 4035., ...
	3108., 2558., 2654., 3044., 4035., 4980., 5760., 7246., 8311., ...
	7228., 5599., 4411., 3552., 2622., 2150., 1925., 1934., 2333., ...
	3696., 5049., 6090., 5852., 6462., 6054., 5205., 4498., 3723., ...
	3163., 2902., 3356., 3732., 4489., 6021., 5283., 5774., 5751., ...
	4531., 3563., 2861., 2526., 3365., 4953., 6599., 8274., 6870., ...
	698., 6824., 7320., 8301., 8237., 8081., 7223., 8412., 7072./

APPENDIX B

TABLE PRESS, 1,123 ...  
/0.00, 0.008, 0.016, 0.024., 0.032., 0.040, 0.048, 0.056, 0.064, ...

.  
Data omitted for brevity.  
.

.  
0., 21., 16., 19., 19., 25., 45., 222., 433., 321., 512., 520., ...  
600., 642., 708., 901., 1196., 1509., 1781., 2048., 2290., ...  
1878., 1529., 980., 662., 465., 328., 258., 218., 190., 173., ...  
163., 155., 141., 131., 130., 130., 128., 116., 118., 113., ...  
112., 188., 511., 586., 668., 565., 230., 532., 758., 439., ...  
807., 898., 1035., 917., 747., 635., 396., 544., 415., 580., ...  
908., 976., 1162., 1309., 932., 829., 546., 361., 312., 565., ...  
851., 505., 808., 1150., 1220., 1151., 1044., 858., 602., ...  
387., 306., 279., 266., 518., 653., 683., 774., 1105., 739., ...  
1259., 720., 702., 603., 420., 442., 569., 357., 721., 806., ...  
810., 756., 1050., 718., 498., 453., 388., 396., 600., 847., ...  
1065., 1330., 960., 1049., 1053., 1211., 1304., 1237., 1237., ...  
1193., 1441., 859., 135./

Undamped Nonlinear Spring

The computer code for the undamped, nonlinear-spring pressure-torque model is listed in the following lines:

"- - - - - DEFINE PRESET VARIABLES"

CONSTANT TSTP = .972, SPEED = 120.

CINTERVAL CINT = 0.01

VARIABLE T = 0.00

DYNAMIC

DERIVATIVE

"- - - - - PRESSURE AND TORQUE"

PR = PRESS (T)

REALTR = ACTTOR (T)

F1 = 0.9944013639 ...

-.00322586335 \* SPEED ...

-.000012702928 \* SPEED \* SPEED ...

APPENDIX B

```

+3.0232572E-07 * SPEED * SPEED * SPEED ...
-1.08996216E-09 * SPEED * SPEED * SPEED * SPEED
T1 = F1 * (-1540.608088 + 16.0684884 * PR ...
-.00510589018 * PR * PR + 7.805 E-07 * PR * PR * PR)
TORQUE = AMAX1 (T1,0.)
ERROR = ABS (REALTR - TORQUE)
TOTERR = INTEG (ERROR, 0.)/TSTP
"
"
TERMT (T.GE.TSTP)
END $ "DERIVATIVE"
END $ "DYNAMIC"
END $ "PROGRAM"

```

Linear Spring With Viscous Damping

The computer code for the linear spring with viscous damping is listed in the following lines:

```

"- - - - - DEFINE PRESET VARIABLES"
LOGICAL          ON
CONSTANT         PI = 3.14159, MASS = 1., NFREQ = 24.0, ...
                 DAMP = 1.0, A1 = 73., POWER = 0.7, PO = 116., ...
                 ON = .TRUE., TAU = 0.3, TSTP = .972
CINTERVAL       CINT = 0.01
VARIABLE        T = 0.00
DYNAMIC
DERIVATIVE
"- - - - - INPUT"
PR = PRESS (T)
PRI = DIM (PRESS (T), PO)
"- - - - - STEADY STATE TORQUE"

```

APPENDIX B

```

Y = EXPF (0., TAU, ON)
PROCEDURAL (SSTOR = A1, PR1, POWER)
    IF (PR1.GT.0.)SSTOR = A1 * (PR1**POWER)
    IF (PR1.LE.0.)SSTOR = 0.
END $ "PROCEDURAL"
"- - - - - DYNAMIC TORQUE"
    WN = 2. *PI*NFREQ
    K = 19289.44/ (WN**2)/MASS
    P = 1./ (WN**2)
    Q = 2. *DAMP/WN
    DYN TOR = CMPXPL (P, Q, SSTOR, 0., 0.) *K
"- - - - - TORQUE OUTPUT"
    TORQUE = DYN TOR * Y
    REALTR = ACTTOR (T)
    ERROR = ABS (REALTR - TORQUE)
    TOTEER = INTEG (ERROR, 0.) /TSTP
TERMT (T.GE.TSTP)
END $ "DERIVATIVE"
END $ "DYNAMIC"
END $ "PROGRAM"

```

Variable Nonlinear Spring With Hysteresis Memory Function

The following lines of computer code define the variable nonlinear spring model with hysteresis memory function:

```

"- - - - - DEFINE PRESET VARIABLES"
LOGICAL          ON, PFLG
CONSTANT         A1 = 89., P1 = 580., C1 = 0.65., ...
                 A2 = 400., P2 = 100., C2 = 0.47., ...
                 Z = 346.7, TAU = 0.075., TSTP = 0.972., ...

```

APPENDIX B

```

        YIC = 36.0, YICT = 0.0, ...
        TRMX2 = 15200., A3 = 104.

CINTERVAL      CINT = 0.01

VARIABLE        T = 0.00

INITIAL

        TORLO = 0.

        TORHI = TRMX2

        SLOPE3 = A3
        ON = .TRUE.
        IC = 0.

        PFLG = .TRUE.

END $ "INITIAL"

DERIVATIVE

"- - - - - PRESSURE AND RATES"

        PR = PRESS (T)

        PRDER = DERIVT (YIC, PR)

        REALTR = ACTTOR (T)

PROCEDURAL (ON, PFLG = PRDER)

        IF ((PRDER.LT.500.) .AND. (PFLG)) PFLG = .FALSE.

        IF ((PRDER.LT.0.) .AND. (PR.LE.P1)) ON = .FALSE.

        IF ((PRDER.GT.0.) .AND. (.NOT. ON) .AND. (PR.GE.P1)) ON = .TRUE.

        IF ((PRDER.GT.50.) .AND. (.NOT. PFLG)) PFLG = .TRUE.

END $ "FIRST PROCEDURAL"

        PRESS1 = DIM (PRESS (T), P1)

        PRESS2 = DIM (PRESS (T), P2)

        Y = EXPF (YICT, TAU, ON)

        SP3 = A3 + (PR/3000.) + Z

        IF ((PFLG) .AND. (PRESS1.GT.0.)) SLOPE3 = AMIN1 (SP3, 400.)

```

APPENDIX B

PROCEDURAL (TQE1, TQE2 = C1, A1, C2, SLOPE3, PRESS1, PRESS2, Y)

IF (PRESS1.GT.0.) TQE1 = A1 \* (PRESS1\*\*C1) \*Y

IF (PRESS1.LE.0.) TQE1 = 0.

IF (PRESS2.GT.0.) TQE2 = SLOPE3 \* (PRESS2\*\*C2)

IF (PRESS2.LE.0.) TQE2 = 0.

END \$ "SECOND PROCEDURAL"

STATE = RSW (PFLG, TQE1, TQE2)

IF (PFLG) TORHI = STATE

IF (.NOT.PFLG) TORLO = STATE

Y2 = 1. + 0.18 \* EXPF (0., 3., ON)

PROCEDURAL (TORQUE = STATE, TORHI, TORLO, TRMX2, PFLG, Y2)

IF (PFLG) TORQUE = AMAX1 (TORLO, STATE)

IF (.NOT. PFLG) TORQUE = AMINI (TORHI, STATE)

TORQUE = AMIN1 (Y2 \* TORQUE, TRMX2)

END \$ "THIRD PROCEDURAL"

ERROR = ABS(REALTR - TORQUE)

TOTERR = INTEG (ERROR, 0.)/TSTP

TERMT (T.GE.TSTP)

END \$ "DERIVATIVE"

END \$ "DYNAMIC"

END \$ "PROGRAM"



A computer-generated motion-picture film supplement L-1284 is available on loan. Requests will be filled in the order received. You will be notified of the approximate date scheduled.

The film (16 mm, 10 min, black and white, silent) shows a time lapse build up of pressure-skid signal, torque-pressure, and friction-slip ratio plots for selected antiskid braking runs. For any plot, each successive movie frame adds two more data points, joined by straight line segments to the plot. When the movie is projected at 18 frames per second, the speed of the plot build up is reduced from real time by a factor of 6.94 and when projected at 24 frames per second the speed is reduced by a factor of 5.19.

Requests for film supplement L-1284 should be addressed to:

NASA Langley Research Center  
Attn: Photographic Branch, Mail Stop 425  
Hampton, VA 23665

-----  
Date \_\_\_\_\_

Please send, on loan, copy of film supplement L-1284 to NASA TP-1959.

\_\_\_\_\_  
Name of organization

\_\_\_\_\_  
Street number

\_\_\_\_\_  
City and State

\_\_\_\_\_  
Zip code

Attention: Name \_\_\_\_\_

Title \_\_\_\_\_

1. Report No. NASA TP-1959		2. Government Accession No.		3. Recipient's Catalog No.	
4. Title and Subtitle  DYNAMICS OF AIRCRAFT ANTISKID BRAKING SYSTEMS				5. Report Date February 1982	
				6. Performing Organization Code 505-44-33-01	
7. Author(s) John A. Tanner, Sandy M. Stubbs, Robert C. Dreher, and Eunice G. Smith				8. Performing Organization Report No. L-14788	
				10. Work Unit No.	
9. Performing Organization Name and Address  NASA Langley Research Center Hampton, VA 23665				11. Contract or Grant No.	
				13. Type of Report and Period Covered Technical Paper	
12. Sponsoring Agency Name and Address  National Aeronautics and Space Administration Washington, DC 20546				14. Sponsoring Agency Code	
15. Supplementary Notes  Technical Film Supplement L-1284 available on request.					
16. Abstract  An experimental investigation was conducted at the Langley Aircraft Landing Loads and Traction Facility to study the dynamic response of representative aircraft antiskid braking systems, and a computer study was performed to assess the accuracy of three brake pressure-torque mathematical models. The investigation utilized one main gear wheel, brake, and tire assembly of a McDonnell Douglas DC-9 series 10 airplane. The experimental investigation indicates that the performance of aircraft antiskid braking systems is strongly influenced by tire characteristics, dynamic response of the antiskid control valve, and pressure-torque response of the brake. The computer study employed an average torque error criterion to assess the accuracy of the three mathematical models. The results of the computer study indicate that a variable nonlinear spring with hysteresis memory function models the pressure-torque response of the brake more accurately than currently used models.					
17. Key Words (Suggested by Author(s))  Antiskid systems Brake pressure-torque response Braking Cornering			18. Distribution Statement  Unclassified - Unlimited  Subject Category 05		
19. Security Classif. (of this report)  Unclassified		20. Security Classif. (of this page)  Unclassified		21. No. of Pages  99	22. Price  A05